Functionalization of multiscale polymer fiber materials: from 1D yarns over 2D nonwovens to 3D sponges

DISSERTATION

zur Erlangung des akademischen Grades einer
Doktorin der Naturwissenschaften (Dr. rer. nat.)
an der Bayreuther Graduiertenschule für Mathematik und
Naturwissenschaften (BayNAT) der Universität Bayreuth

vorgelegt von

Sophie Edith Fritze

geboren in Bamberg

Bayreuth, 2025

Die vorliegende Arbeit wurde in der Zeit von April 2022 bis August 2025 in Bayreuth am Lehrstuhl Makromolekulare Chemie II unter Betreuung von Herrn Professor Dr. Andreas Greiner angefertigt.

Alle beschriebenen präparativen Arbeiten wurden in der Arbeitsgruppe von Prof. Dr. Andreas Greiner an der Universität Bayreuth durchgeführt. Die thermischen Analysen und Auswertungen haben in der Arbeitsgruppe von Prof. Dr. Markus Retsch stattgefunden.

Vollständiger Abdruck der von der Bayreuther Graduiertenschule für Mathematik und Naturwissenschaften (BayNAT) der Universität Bayreuth genehmigten Dissertation zur Erlangung des akademischen Grades einer Doktorin der Naturwissenschaften (Dr. rer. nat.).

Form der Dissertation: Monografie

Dissertation eingereicht am: 08.08.2025

Zulassung durch das Leitungsgremium: 19.08.2025

Wissenschaftliches Kolloquium: 19.03.2026

Amtierender Direktor: Prof. Dr. Jürgen Senker

Prüfungsausschuss:

Prof. Dr. Andreas Greiner (Gutachter)

Prof. Dr. Markus Retsch (Gutachter)

Prof. Dr. Johannes Brendel (Vorsitz)

Prof. Dr.-Ing. Christina Roth

Die vorliegende Arbeit ist als Monografie verfasst.

Teile der Arbeit sind bereits in folgender Publikation erschienen:

Thermal Transport in Polystyrene Nonwovens: Influence of Anisotropy, Structural Modification, and Functionalization

I. Klein*, **S. E. Fritze***, A. Berger, H. Schmalz, M. Retsch, A. Greiner, *ACS Appl. Polym. Mater.* **2026**, *8*, 1954.

https://doi.org/10.1021/acsapm.5c03952

(* contributed equally to this work)

Diese Publikation ist in der vorliegenden Arbeit mit der Literaturstelle [128] zitiert.

Für meine Eltern

„I have not failed. I've just found 10,000 ways that won't work."

Thomas Alva Edison

Index

Table of abbreviations

α	Thermal diffusivity [mm^2/s]
α_i	Orientation angles
δ	Chemical shift [ppm]
ε_b	Elongation at break [%]
κ	Thermal conductivity [W/m·K]
$\kappa_{10\% comp}$	Thermal conductivity at 10 % compression [W/m·K]
$\kappa_{50\% comp}$	Thermal conductivity at 50 % compression [W/m·K]
ρ	Density [g/cm^3]
ρ_{Ag}	Density of silver [g/cm^3]
ρ_{bulk}	Density of the bulk phase [g/cm^3]
σ	Electrical conductivity [S/cm]
$\sigma_{50\% comp}$	Compressive strength at 50 % compression [kPa]
Φ	Heat flow rate [J/s]
ω_i	Fiber segment weighing factor
$Đ$	Polydispersity
1D	One-dimensional
2D	Two-dimensional
3D	Three-dimensional
4PP	Four-Point Probe
A	Cross-sectional area of the sponge [cm^2]
AC	Acrylic acid
AgNWs	Silver nanowires
AgNPs	Silver nanoparticles
AIBN	Azobisisobutyronitrile
ATR	Attenuated Total Reflection

a.u.	Arbitrary unit
BOS	Bead-on-String
BPA	4-Aminobenzophenone
BPAA	*N*-(4-benzoylphenyl)acrylamide)
b-PEI	Branched poly(ethyleneimine)
BSE	Backscattered electron
CBS	Circular Backscattered Detector
CCD	Charge-Coupled Device
CNTs	Carbon nanotubes
CoNWs	Cobalt nanowires
C_p	Specific heat capacity [J/kg·K]
c_{SF}	Short fiber concentration [mg/mL]
DCM	Dichloromethane
d_i	Segment diameter
DMF	Dimethylformamide
DMSO	Dimethyl sulfoxide
dQ/dt	Heat flow rate [J/s]
DSC	Differential Scanning Calorimetry
dT/dx	Temperature gradient [K/m]
EDX	Energy-dispersive X-ray
E_{mod}	YOUNG's modulus [GPa]
Et_3N	Triethylamine
ETD	EVERHART-THORNLEY-Detector
F_{max}	Maximum force before failure [MPa]
FT-IR	FOURIER Transform Infrared
GPC	Gel Permeation Chromatography

HFIP	Hexafluoroisopropanol
HV	High voltage [kV]
ICP-OES	Inductively Coupled Plasma Optical Emission Spectroscopy
IR	Infrared
l	Height of the sponge [cm]
l_i	Segment length
LEXT	Laser Scanning Confocal Microscope
LIT	Lock-In Thermography
M	Molar mass [g/mol]
MA	Methyl acrylate
MABP	(4-Benzoylphenyl)methacrylate
m_{Ag}	Mass of silver fraction [mg]
MMA	Methyl methacrylate
$M_{n,app}$	Apparent Number Average Molecular Weight [g/mol]
m_{sponge}	Mass of the sponge fraction [mg]
MTPS	Modified Transient Plane Source
$M_{w,app}$	Apparent Weight Average Molecular Weight [g/mol]
NAS	*N*-Succinimidyl acrylate
NFES	Near-Field Electrospinning
NHS	*N*-Hydroxysuccinimide
NMR	Nuclear Magnetic Resonance
NWs	Nanowires
P	Porosity [%]
P4VP	Poly(4-vinylpyridine)
p.a.	Pures analytical
PAN	Poly(acrylonitrile)

PCL	Poly(ε-caprolactone)
PEEK	Poly(ether ether ketone)
PEI	Poly(ethyleneimine)
PEO	Poly(ethylene oxide)
PET	Poly(ethylene terephthalate)
PLA	Poly(lactic acid)
P(MA-*co*-MMA-*co*-MABP)	Poly(methyl acrylate-*co*-methyl methacrylate-*co*-(4-benzoylphenyl)methacrylate)
PMMA	Poly(methyl methacrylate)
P(NAS-*co*-BPAA)	Poly(*N*-succinimidyl acrylate-*co*-*N*-(4-benzoylphenyl)acrylamide)
PP	Polypropylene
P(PMAA-*co*-BPAA)	Poly(*N*-(pyridin-4-ylmethyl)acrylamide-*co*-*N*-(4-benzoylphenyl)acrylamide)
PTFE	Poly(tetrafluoroethylene)
PS	Polystyrene
PVP	Poly(vinylpyrrolidone)
RAFT	Reversible addition-fragmentation chain-transfer polymerization
R	Electrical resistivity [Ω]
rpm	Rounds per minute
RT	Room temperature
S_{2D}	Orientation parameter
S	Surface area [cm^2]
SDV	Styrene-divinylbenzene
SE	Secondary electron
SEM	Scanning Electron Microscopy

SJES	Stable Jet Electrospinning
TEAC	Triethylammonium chloride
T_g	Glass transition temperature [°C]
TGA	Thermogravimetric analysis
UV-Vis	Ultraviolet-visible
V_{Ag}	Volume fraction of silver [vol%]
V_{AgNW}	Volume of added AgNW suspension [mL]
V_{sponge}	Volume fraction of the sponge [vol%]
w	Weight fraction [wt%]
$W(log\ M)$	Mass fraction of molecules with a given molar mass (M)
x	Molar fraction [mol%]
XRD	X-ray diffraction

Summary

This work focused on the fabrication and investigation of electrospun fiber materials with different dimensionalities. Special emphasis was placed on the implementation of orientation within hierarchically structured fiber scaffolds. The central challenge, apart from structural design, lay in the integration of various metallic and non-metallic components into functional composites. For the functionalization of non-conductive polymers, mainly silver nanowires (AgNWs) were used as one-dimensional and anisotropic additives. These nanofiller structures constituted the main subject of investigation for thermal and electrical transport analysis, which was crucial for understanding the relationships between local structural properties and macroscopic transport performance. The analysis and evaluation were carried out by Ina Klein (Physical Chemistry I, Prof. Dr. Markus Retsch).

Based on a consistent manufacturing process, electrospinning permitted the construction of a wide variety of fiber architectures. In the first chapter, one-dimensional (1D) poly(acrylonitrile) (PAN) yarns with different stretch ratios were produced and subsequently functionalized *via* grafting reaction utilizing poly(ethyleneimine) (PEI). This led to the establishment of anchor groups for the final coating with silver nanowires. The analyses revealed that the combination of random nanowire distribution, geometric constraints of the yarn, and interfacial scattering decisively not only determined the conductivity for heat and electrons in the 1D system, but also introduced additional challenges for their measurement.

The second chapter expanded the investigation into two-dimensional (2D) structures by producing polystyrene (PS) nonwovens with controlled degrees of fiber orientation. The orientation was achieved by rapid rotation of the drum collector during electrospinning, enabling uniaxial alignment of the fibers. Two different functionalization strategies were applied: the incorporation of silver nanowires directly into the polymer solution prior to processing, which allowed alignment of the nanowires within the fiber matrix, as well as a fiber enclosing post-processing copper coating. The results of the thermal analysis revealed a direct correlation between fiber orientation and thermal transport anisotropy. A higher degree of uniaxial orientation of the PS fibers significantly increased the thermal conductivity along the fiber axis compared to the direction perpendicular to the orientation axis. However, this effect on the measured conductivity values was limited in AgNW functionalized nonwovens by non-percolating networks and interfacial scattering, whereas copper-coated systems established continuous metallic conduction pathways.

In the third chapter, three-dimensional (3D) sponges were realized by freeze-drying of short electrospun fibers. Fibers with the characteristic bead-on-string (BOS) morphology served as the starting material, whose unique structure was utilized for sponge formation. Within this most complex dimensional level, both structural control and functionalization proved particularly challenging. A method was developed that enabled homogeneous functionalization of the sponges with silver nanowires prior to freeze-drying. The fiber-forming polymers were synthesized and analyzed by Marius Schmidt (Macromolecular Chemistry II, Prof. Dr. Andreas Greiner) and processed in collaboration into the composite sponges. These structures exhibited increased mechanical stability in the presence of both BOS fibers and nanowires, while the analysis of electrical properties uncovered complex relationships between nanofiller distribution and percolation behavior in three-dimensional and thermally insulating networks.

The developed fiber composites with varying compositions, structures, functionalization, and dimensionalities provide a solid foundation and an important building block on the path towards the development of multifunctional textiles. The concept of coating, alignment, and distribution of anisotropic nanofillers in differently extended fiber architectures was investigated across all dimensionalities. The results showed that the structural architecture of the fiber matrix, the orientation and distribution of the nanofiller, as well as the quality of the interfacial interactions, are decisive parameters for macroscopic transport properties. These findings contribute to the fundamental understanding of structure-property relationships in functionalized fiber materials.

Zusammenfassung

Diese Arbeit beschäftigte sich mit der Herstellung und Untersuchung elektrogesponnener Fasermaterialien unterschiedlicher Dimensionalitäten. Ein besonderer Fokus lag dabei auf der Implementierung von Orientierung in hierarchisch aufgebauten Fasergerüsten. Die zentrale Herausforderung bestand neben der strukturellen Gestaltung unter anderem auch in der Integration verschiedener metallischer und nicht-metallischer Komponenten zu funktionalen Kompositen. Zur Funktionalisierung der nicht-leitenden Polymere wurden vorwiegend Silbernanodrähte (AgNWs) als eindimensionale und anisotrope Additive eingesetzt. Diese Nanofillerstrukturen bildeten den Hauptuntersuchungsgegenstand für die thermische und elektrische Transportanalyse, welche für das Verständnis der Zusammenhänge zwischen lokalen Struktureigenschaften und makroskopischer Transportperformance entscheidend war. Diese Analyse und Auswertung wurde von Ina Klein (Physikalische Chemie I, Prof. Dr. Markus Retsch) durchgeführt.

Auf Basis eines einheitlichen Herstellungsprozesses ermöglichte das Elektrospinnen die Konstruktion verschiedenster Faserarchitekturen. Im ersten Kapitel wurden eindimensionale (1D) Poly(acrylnitril) (PAN) Garne mit unterschiedlichen Verstreckungsgraden hergestellt und anschließend durch eine Graftingreaktion mit Poly(ethylenimin) (PEI) funktionalisiert. Dadurch konnten Ankergruppen für die finale Beschichtung mit Silbernanodrähten etabliert werden. Die Analysen zeigten, dass die Kombination aus ungerichteter Nanodraht-Verteilung, geometrischen Beschränkungen des Garns und Grenzflächenstreuung nicht nur die Leitfähigkeit für Wärme und Elektronen in dem 1D-System maßgeblich bestimmte, sondern auch zusätzliche Herausforderungen für eine präzise Messung dieser Eigenschaften mit sich brachte.

Das zweite Kapitel erweiterte die Untersuchung auf zweidimensionale (2D) Strukturen durch die Herstellung von Polystyrol (PS) Nonwoven mit kontrollierten Faserorientierungsgraden. Die Orientierung wurde durch schnelle Rotation des Rollenkollektors während des Elektrospinnens erreicht, wodurch eine uniaxiale Ausrichtung der Fasern ermöglicht wurde. Zwei verschiedene Funktionalisierungsstrategien kamen zur Anwendung: die Einarbeitung von Silbernanodrähten direkt in die Polymerlösung vor der Verarbeitung, welche eine Ausrichtung der Nanodrähte innerhalb der Fasermatrix ermöglichte, sowie eine faserumschließende Kupferbeschichtung nach der Faserverarbeitung.

Die Ergebnisse der thermischen Analyse offenbarten einen direkten Zusammenhang zwischen Faserorientierung und Wärmetransportanisotropie. Eine höhere uniaxiale Ausrichtung der PS-Fasern steigerte die Wärmeleitfähigkeit entlang der Faserachse signifikant gegenüber der quer zur Orientierung. Der Effekt auf diesen Wert wurde jedoch bei AgNW-funktionalisierten Nonwoven durch nicht-perkolierende Netzwerke und Grenzflächenstreuung begrenzt, während Cu-beschichtete Systeme durchgehende metallische Leitpfade etablierten.

Im dritten Kapitel wurden durch Gefriertrocknung von elektrogesponnenen Kurzschnittfasern dreidimensionale (3D) Schwämme realisiert. Als Ausgangsmaterial dienten Fasern mit der charakteristischen Bead-on-String (BOS) Morphologie, deren einzigartige Struktur für die Schwammbildung genutzt wurde. In dieser komplexesten Dimensionsebene erwies sich die Strukturvorgabe und -funktionalisierung als besonders herausfordernd. Es wurde eine Methode entwickelt, mit der die Schwämme bereits vor der Gefriertrocknung homogen mit Silbernanodrähten funktionalisiert werden konnten. Die faserbildenden Polymere wurden von Marius Schmidt (Makromolekulare Chemie II, Prof. Dr. Andreas Greiner) synthetisiert, analysiert und in Kooperation zu den Komposit-Schwämmen verarbeitet. Diese Strukturen zeigten in Anwesenheit der BOS Fasern sowie der Nanodrähte eine gesteigerte mechanische Stabilität, wobei die Analyse der elektrischen Eigenschaften komplexe Zusammenhänge zwischen Nanofiller-Verteilung und Perkolationsverhalten in dreidimensionalen und thermisch isolierenden Netzwerken aufdeckte.

Die entwickelten Faserkomposite mit unterschiedlichen Zusammensetzungen, Strukturierungen, Funktionalisierungen und Dimensionalitäten liefern eine fundierte Basis und wichtigen Baustein auf dem Weg zur Entwicklung multifunktionaler Textilien. Das Konzept der Beschichtung, Ausrichtung und Verteilung anisotroper Nanofiller in unterschiedlich ausgedehnten Faserarchitekturen wurde über alle Dimensionalitäten hinweg untersucht. Die Ergebnisse zeigten, dass die strukturelle Architektur der Fasermatrix, die Orientierung und Verteilung der Nanofiller sowie die Qualität der Grenzflächeninteraktionen entscheidende Parameter für die makroskopischen Transporteigenschaften darstellen. Diese Erkenntnisse tragen zum grundlegenden Verständnis der Struktur-Eigenschafts-Beziehungen in funktionalisierten Fasermaterialien bei.

1 Introduction

Modern societies are constantly facing greater challenges resulting from a growing world population, climate change, digitalization and rapid evolution of industry. In response to this, materials science developed as a distinct, multidisciplinary field in the 1950s, investigating the correlation between the structure, properties and processing of materials.[1] While initially focusing on metals, polymers, ceramics and their composites, the discipline has continuously evolved to encompass a wide range of materials, such as biological, nano- and hybrid materials.[1,2] In particular, biology serves as an important blueprint for various nature-inspired architectures as templates for improved or multifunctional materials. An important principle used by nature is hierarchical structurization. Hierarchical materials are organized on several levels, ranging from the nano- to the macroscale. Each level is essential for the overall properties of the material.[3] This approach offers several advantages. First, it enables improved mechanical properties by combining materials with different characteristics. Thus, materials can exhibit improved strength, stiffness or toughness. The approach of using hierarchical composites also enables lightweight construction, which can offer high strength at low weight, as well as multifunctionality achieved by the individual components. [2,3] Spider silk is a remarkable example of hierarchical structuring in nature, combining stiff and crystalline, as well as flexible and amorphous protein domains at different levels from the molecular to the macrofiber level. This multiscale arrangement gives spider silk both high strength and high elasticity after processing and makes it one of the toughest natural fibers.[2,4] While nature is limited by the elements available and the conditions under which the materials are formed materials science has the means to overcome these restrictions. Due to the broad availability of metals and their alloys, originally natural structural concepts (such as polymers and ceramics) can be complemented. At the same time, biological production processes such as self-assembly and growth can be replaced by more efficient processes.[3] These approaches are designed as multiscale fabrication methods following bottom-up, top-down or hybrid concepts.[5] One of the most extensively studied and most versatile techniques for the production of nano- and microfibers is the method of electrospinning, which will be described in the following.[6]

1.1 Electrospinning of nanofibers

Electrospinning is a continuous process that allows the production of fibers with a high surface-to-volume ratio and diameters in the sub micrometer range.[7] Both of these characteristics are difficult to achieve using conventional mechanical fiber processing methods. The basic electrospinning set-up consists of three main components: a high-voltage source, a spinneret and a grounded collector plate (see Figure 1a). In this configuration, a high-voltage electrostatic field is applied between the cannula of a syringe and a counter electrode or a grounded collector.[8]

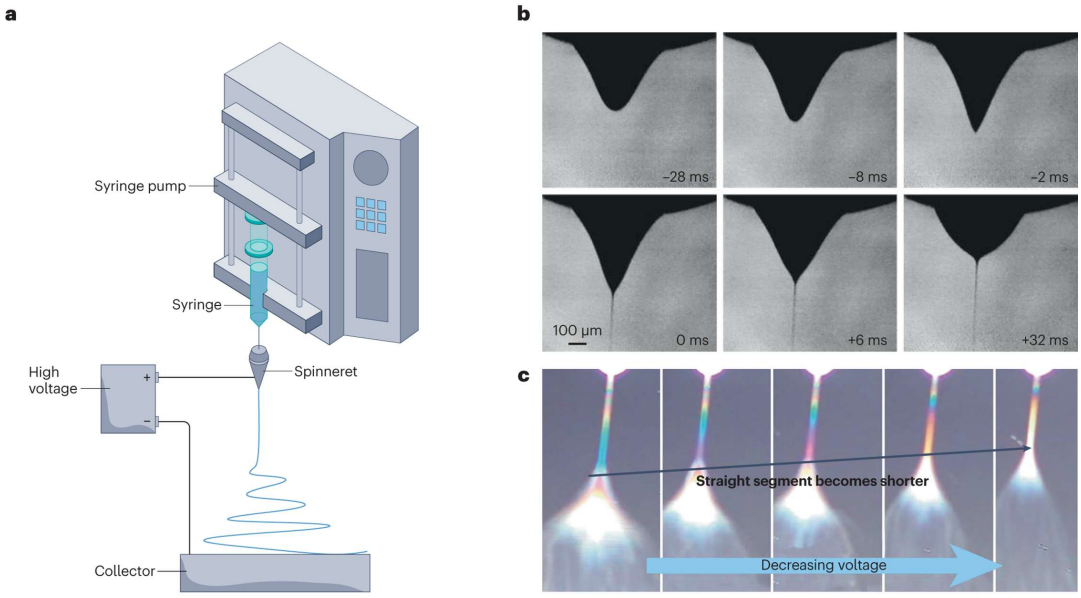

Figure 1: Illustration of a simple electrospinning set-up (**a**). Images showing the transformation of a poly(ethylene oxide) (PEO) droplet, which changes from a conical to a spherical shape under the application of high voltage, before the ejection of a fiber jet (**b**) as well as images of a PEO jet's diameter and linear segment length as a function of applied voltage (**c**). Reproduced from Ji et al.[9] with permission from Springer Nature.

The electrospinning process can be divided in a sequence of four steps.[10] During this, the solution, suspension or melt that is pumped through the cannula is exposed to a high-voltage electric field. Under the influence of the voltage, the droplet at the tip of the cannula deforms in the first step into a so-called *Taylor cone* (see Figure 1b).[11] As the voltage increases further, the electric field approaches a critical voltage. At this point, the repulsive electric forces overcome the surface tension forces and a jet emerges from the drop.[12–14] This jet is accelerated towards the counter electrode, with the jet thinning due to the evaporation of solvent (resp. the solidification of the melt) and only the fine fibers are deposited as a nonwoven. However, the path of the electrically charged liquid jet in the second step only travels in a straight line towards the counter electrode for a certain distance (see Figure 1c).[8,11] The third step is initiated by repulsive forces between the charged sections of the jet, which destabilize the jet and cause it to bend.[15]

Within this unstable region, the whipping movements cause the jet to be stretched, which helps to create thinner fibers. At the same time, the solvent evaporates, causing the fibers to stiffen and deposit on the substrate in the fourth and last step. The combination of these dynamic processes is crucial for the formation of fibers with diameters in the nanometer range.[15]

In addition, there are further parameters that have a significant influence on the fiber deposition and properties. As illustrated in Table 1, these variables can be divided into three categories. Among these are processing conditions, such as voltage or set-up geometry. But also the environment influences the behavior of the fiber jet through the prevailing temperature and humidity. To ensure the reproducible fabrication of nanofibers with the desired properties, it is therefore crucial to control and optimize the process and ambient conditions.[8,11]

Table 1: Overview of the factors influencing the electrospinning process.[8,11,16]

Processing conditions	**Material properties**	**Environmental conditions**
Electrostatic potential	Concentration/Viscosity	Temperature
Electric field strength	Solvent (and its polarity)	Humidity
Feed rate	Conductivity	Local air flow
Distance between syringe and collector	Surface tension	Atmospheric composition
Syringe and collector geometry	Additives	Pressure

One key factor, which is usually already predetermined by the intended use of the fibers, is the selected material and its corresponding material properties as a solution, suspension or melt. Properties like viscosity or surface tension, for example, affect the suitability for processing by electrospinning. In general, potential base materials can be divided into four classes. These include organic, inorganic, composites as well as living matter. Among the organic materials used are mainly synthetic and natural polymers.[9] The latter comprise representatives such as polysaccharides, collagen and gelatine. Polymers like poly(vinylpyrrolidone) (PVP), poly(ε-caprolactone) (PCL) or poly(lactic acid) (PLA) are frequently applied synthetic materials.[10] Furthermore, the use of small molecules such as cyclodextrins is also possible. Processing of these cyclic oligosaccharides is primarily feasible, because the processability not only depends on the material itself, but also on the solvent and its characteristics.[17]

Apart from the solubility, conductivity and volatility show significant influence on the process, as these parameters can enable or impede continuous fiber formation. These dependencies further complicate the application of inorganic materials such as metal nanomaterials or ceramics. In these cases, composites are often used to overcome this drawback. Polymers are usually applied as carriers for the inorganic component. Additionally, this multi-component approach can also be adapted to process living matter such cells and microorganisms.[9]

The previously described complex dependencies between the individual parameters also have an impact on which electrospinning technique is (or can be) chosen. This has led to the development of a variety of methods and set-ups. One example is the approach of Near-Field electrospinning (see Figure 2), which enables a defined fiber deposition. This is achieved by a process-related suppression of the previously described whipping jet regime in combination with the use of a moving table.[18,19]

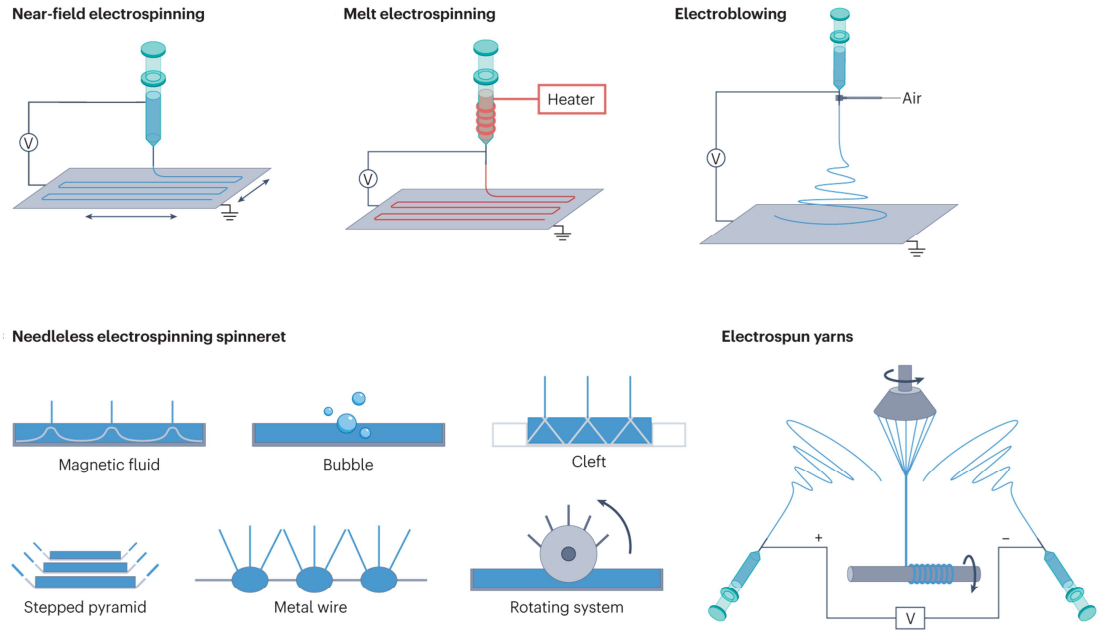

Figure 2: Illustration of different electrospinning set-ups, including Near-Field electrospinning, Melt Electrospinning, Electro-blowing, various Needleless Electrospinning spinnerets and Yarn Electrospinning. Reproduced from Ji et al.[9] with permission from Springer Nature.

Besides solution electrospinning, thermoplastic polymers may also be electrospun from the melt. In addition to the avoidance of an additional solvent, this method also captivates through possible defined fiber deposition comparable to 3D printing. In contrast to solution-based methods, however, the fiber diameters achieved are higher, along with the throughput.[20] In the context of greater output, which is needed for the transition from laboratory to industrial scale, methods such as electroblowing and needleless electrospinning are also becoming relevant.[9]

Both techniques enable a more continuous solution supply utilizing different principles, which in turn create new platforms for process development.[9] The Yarn Electrospinning method illustrates this very well. Using a multi-needle set-up in combination with different tools for twisting the fiber bundles into yarns shows the variety of combinations. There are both approaches with a funnel device (see Figure 2) as well as rotating disk collectors (see Figure 3).[21]

The choice of collector geometry used in the electrospinning process is decisive for the properties and structure of the resulting nanofiber mats. The motivation for the development of different collector designs derives from the desire to specifically influence the formation, orientation and morphology of the nanofibers and thus obtain materials with tailored properties for specific applications. Figure 3 provides a graphic overview of the collector geometries which have been used previously, and which can be divided into stationary and rotating collectors. In general, the former mainly generates mats with randomly distributed fibers. Orientation can be achieved with the aid of an additional electric field. In addition, different arrangements of the electrodes are possible so as to generate different orientation axes.[22]

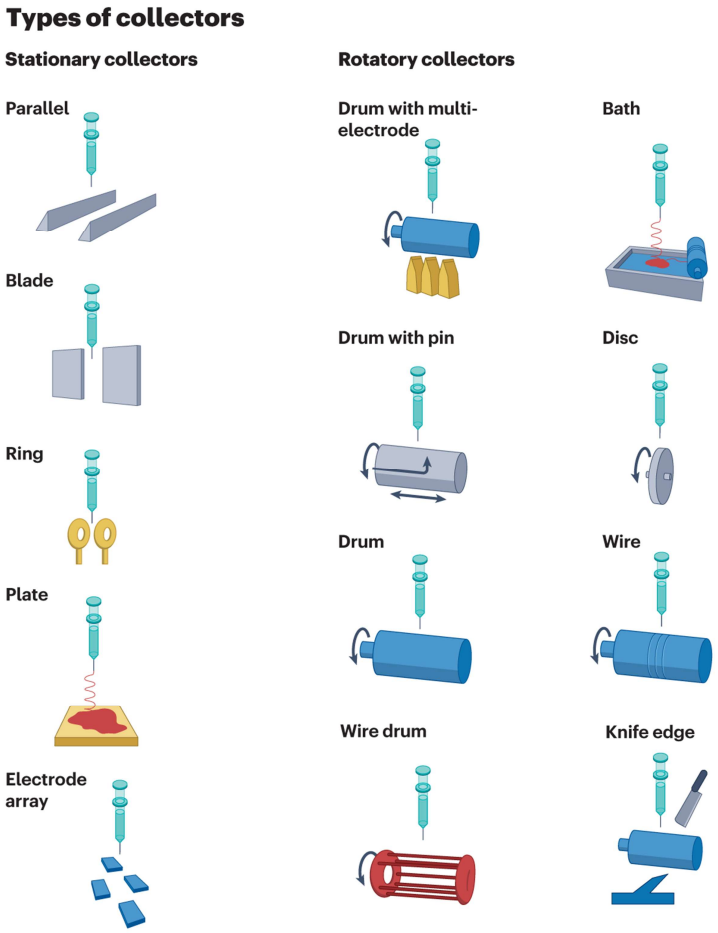

Figure 3: Illustration of different types of electrospinning collectors (both stationary and rotatory). Reproduced from Ji et al.[9] with permission from Springer Nature.

An even larger variety exists among the rotating collectors. This type of fiber collector focuses primarily on the homogenous distribution and orientation of the fibers. Therefore, the size, pattern, mobility and function of the drum can vary.[9,22]

As a counterpart to the collector, the solution-emitting cannula is also of interest for a steady improvement. The devices illustrated in Figure 4 predominantly target the maximization of solution throughput.[9] However, it is also possible to influence the fiber composition through the design of the nozzles. Modifications to the spinnerets include the use of coaxial, bicomponent as well as gas jacket spinnerets. Coaxial nozzles are characterized by two concentric capillaries. Through the separation between the inner and outer capillary, it is possible to spin two polymers simultaneously, as these are only combined into one fiber jet when exiting the cannula. Associated with this are bicomponent nozzles, where two capillaries arranged next to each other are utilized, resulting in a side-by-side configuration of the fibers. In contrast, gas jacket nozzles benefit from a gas stream that surrounds the as-spun fibers. This gas stream can thus influence the volatilization of the solvent and improve the surface morphology of the fibers.[23]

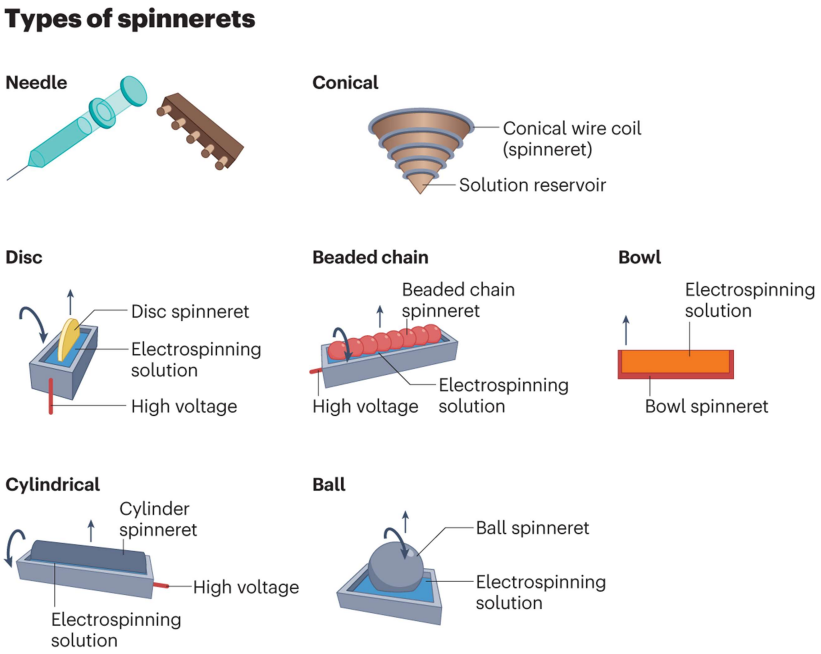

Figure 4: Illustration of different types of electrospinning spinnerets. Reproduced from Ji et al.[9] with permission from Springer Nature.

The numerous modifications to spinnerets and electrodes are primarily motivated by the properties associated with different fiber morphologies. Electrospun fibers do not necessarily have to be cylindrical but can take on a variety of shapes and structures, which in turn offer new features and application potential.[9]

The control of the process parameters and the choice of suitable materials not only makes it possible to adjust the diameter but also to produce fibers with ribbon, branched, beaded or even spiral shape aside to core-shell, janus, hollow and porous structures (see Figure 5).[9]

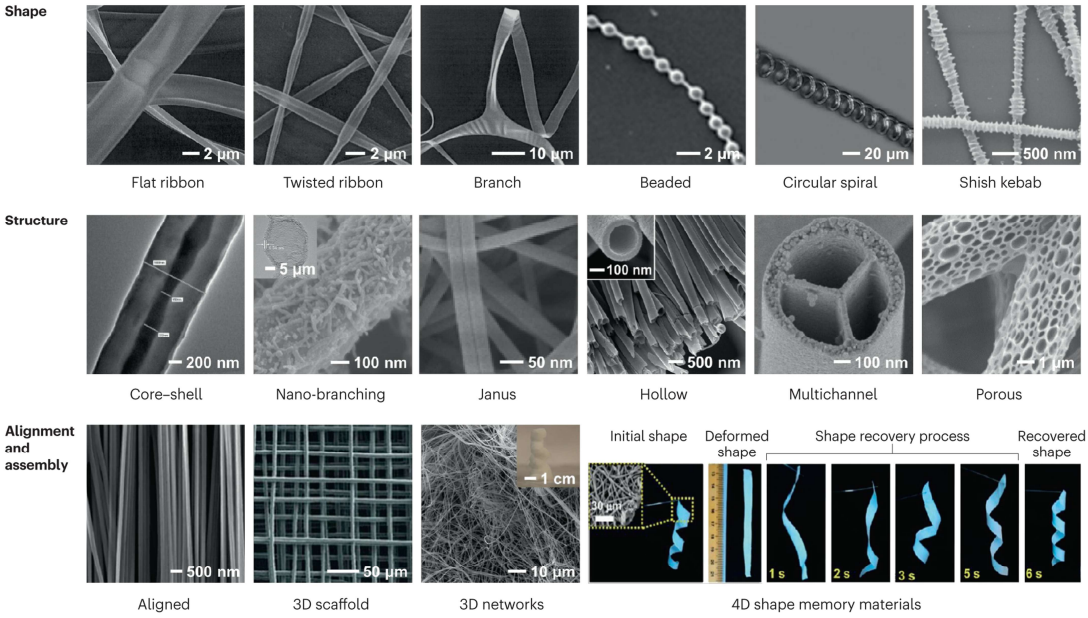

Figure 5: Selection of SEM and optical images highlighting different shapes, structures, alignments and assemblies of electrospun fibers. Reproduced from Ji et al.[9] with permission from Springer Nature.

Figure 5 also outlines that the fiber architecture, assembly and therefore dimensionality can be influenced with the selected electrospinning technique. As the most basic 1D structure, individual nanofibers (with their specific morphology) serve as building blocks for more complex assemblies. With the bundling of several such nanofibers, 1D yarns with increased strength and stability can be created.[21] The transition to 2D structures is then made with the deposition of nanofibers on a collector. All options for the orientation and patterning of the nonwoven remain unrestricted in this case. This stands in contrast to 2D wet-laid nonwovens consisting of randomly oriented short electrospun fibers. But these membranes, made from suspensions of short fibers, captivate with balanced fiber densities and higher quality than nonwovens made from continuous fibers.[24] A similar principle is used for the production of 3D sponge structures. This also involves suspensions of short electrospun fibers which can be transformed into highly porous 3D structures through freeze drying. In addition to various nonwoven layering approaches, the literature also proposes methods that use a combination of electrospinning and 3D printing technologies. These promise the production of complex 3D structures with a more controllable shape and porosity.[25]

The interest of electrospun fiber materials for various applications is primarily derived from their unique properties. Among these is the high surface-to-volume ratio.[8] Besides, the high specific surface area, they also appeal with high flexibility and mechanical stability.[26,27] At the same time, the lightness of the material can be ensured with the controllable porosity.[12,15] Along with functionalization, electrospun fibers can also be coated or loaded with various materials to achieve further specific functions.[11] These properties open a broad spectrum of possible applications. In the field of biomedicine, and more specifically in the field of tissue engineering, electrospun fiber scaffolds can serve as 3D support structures for cell growth and tissue formation.[8,15] It is remarkable how well electrospun fibers can mimic the fibrillar structure of the extracellular matrix.[28,29] In drug delivery systems, they can further serve as a carrier architecture for the controlled release of encapsulated drug molecules.[30] In addition to medical applications, electrospun fibers are also considered as air and water filters. The high porosity and specific surface area of the materials not only enable efficient filtering of particles but can also be beneficial for the creation of membranes for oil/water separation processes.[15] The continuous evolution of fiber-based nanomaterials finally paves their way for use as substrates or conductive elements in flexible sensors, displays and energy storage devices.[26] In the context of smart textiles, they can also take on a textile application character. These multifunctional fabrics do not only have to be waterproof, breathable or insulating, they also have to adapt actively to ambient changes.[31]

Despite the numerous advantages and the wide range of possible applications offered by electrospinning, there are also some limitations in terms of scalability and control over the resulting fiber structures. An important limiting factor in this regard is the low production rate, which makes upscaling to an industrial standard difficult.[6] Added to this is the impact caused using (organic) solvents. These do not only come along with a negative environmental effect, but above all a cost-generating effect.[9] In addition, the limited control of fiber morphologies and reproducibility pose an obstacle on the way to broad establishment.[24] Current efforts focus on overcoming these challenges through the development of new electrospinning techniques, optimization of electrospinning parameters and continuous expansion of starting materials. In this context, the introduction of machine learning can have a transformative effect on future research, as it enables the prediction of fiber characteristics, such as fiber diameter, by identifying complex, non-linear relationships between process parameters and fiber properties. Through the use of extensive experimental datasets, machine learning algorithms facilitate the systematic optimization of process conditions, thereby accelerating the development of electrospun nanofibers with tailored properties for diverse applications.[32]

1.2 Functionalization of nanofibers

Similar to the processing of nanofibers, there is a broad spectrum of options to improve their initial properties and functionalities. This functionalization contributes just as much towards greater application as the processing itself. The following Figure 6 gives an overview of possible structural components and functionalities for the modification of electrospun fibers. Blending different polymers is a simple yet popular method to achieve the best possible combination of properties from individual components, thereby uniting their respective advantages to realize optimal material performance.[33,34] For example, the incorporation of enzymes and biomolecules as blend components can significantly enhance the biological compatibility of fibrous scaffolds with surrounding tissue.[35] Surfactants, which in turn contribute to tune wettability, also support this process.[36] In addition, supramolecular structures such as cyclodextrins, but also dendrimers, can be exploited to form inclusion complexes with organic contaminants or heavy metal ions due to their large number of functional groups, which makes them valuable for water purification purposes.[37,38] Targeted introduction of molecular functionalities is crucial for tuning fiber properties, as attributes like hydrophilicity/hydrophobicity (-OH, -COOH), biocompatibility and cell adhesion (-COOH, -OH, NH_2), or surface charge (-SO_3H) can thus be specifically adjusted.[39–41]

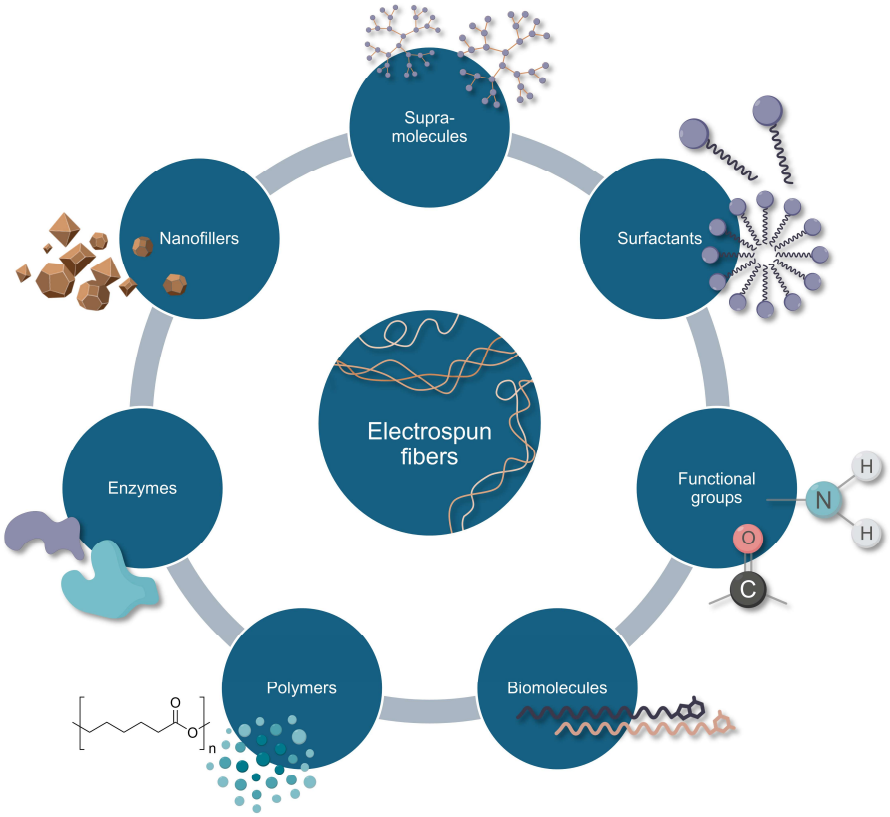

Figure 6: Overview of structural components and functionalities for the modification of electrospun fibers (adapted from SAGITHA et al.).[38]

Another class of materials that can have a crucial impact on physical, chemical and biological properties are nanofillers. In the overview in Figure 7, these fillers are classified according to their origin.

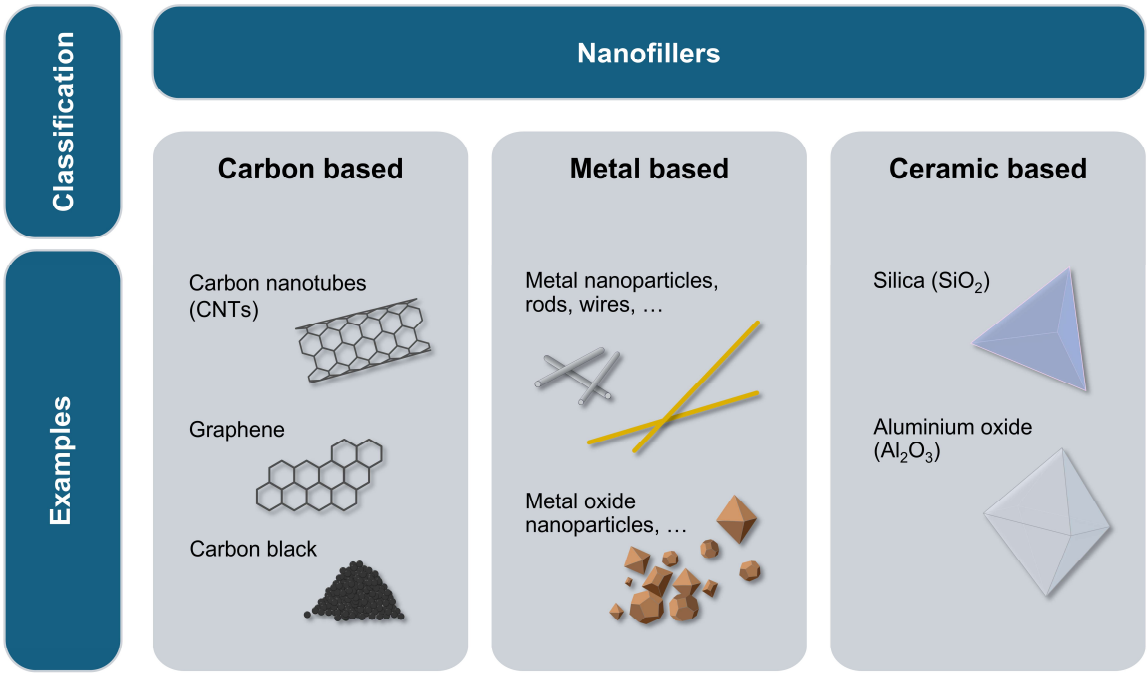

Figure 7: Classification and examples of nanofillers, sorted according to their origin.[42–44]

Carbon-based nanofillers, such as carbon nanotubes (CNTs) or graphene, enhance the mechanical, electrical and thermal properties of electrospun fibers due to their unique composition and structure.[42] Metallic nanofillers as particles (and other geometric shapes) of gold, silver or platinum can impart catalytic, antibacterial and optical properties to electrospun fibers. Whereas metal oxide nanoparticles such as titanium dioxide, zinc oxide and iron oxide improve the mechanical, optical and photocatalytic properties of electrospun fibers.[43] Overlapping with members of metal oxides, there is also the class of ceramics. Their representatives, such as silica and aluminum oxide, have a high intrinsic strength. Embedded in a polymer fiber matrix, they act as mechanical reinforcing elements and can simultaneously increase thermal and chemical resistance.[44]

The functionalization with the previously described nanofillers or other structural compositions from Figure 6 is carried out *via* pre-processing methods (*in situ*) or post-processing methods (*ex situ*). In the case of *in situ* methods, the nanofillers or other components are embedded within the surrounding (polymer) matrix before or during processing. This can be done through simple solution blending or through special techniques such as coaxial electrospinning (see Chapter 1.1).[43,45] In contrast, with *ex situ* methods, the functional components are incorporated onto the fibers after electrospinning.[43]

This type of method can be further divided into three categories by means of physical, physicochemical and chemical methods.[46] Table 2 provides a concise overview and lists some examples for each modification type.

Table 2: Overview of possible modification methods for electrospun micro- and nanofibers (adapted from KOWALCZYK).[46]

<table>
<tr><th colspan="4">Electrospun micro- and nanofiber modification methods</th></tr>
<tr><th colspan="4">Classification by time</th></tr>
<tr><th>Pre-processing (in situ)</th><th colspan="3">Post-processing (ex situ)</th></tr>
<tr><td rowspan="2">• Polymer blending[47]
• Blending with other additives and nanofillers[26,48,49]</td><td colspan="3">Classification by type of modification</td></tr>
<tr><td>Physical</td><td>Physicochemical</td><td>Chemical</td></tr>
<tr><td>• Annealing[38,46]
• Stretching[46,47]
• Leaching[46]
• Plasma treatment[50,51]
• Ultrasound treatment[46]
• Surface absorption[46]
• UV-photo-lithography[46]
• Laser-ablation[46]</td><td>• Plasma treatment and surface grafting[46]
• Plasma treatment with surface anchoring[46,50]
• Carbonization with reducing atmosphere[46,52]
• Sintering with oxidizing atmosphere[46,53]</td><td>• Crosslinking[47,50]
• Wet modification[52]
○ (Surface) hydrolysis[46]
○ Oxidation[47,54]
○ Grafting polymerization[38,55]
○ Metallization[56–58]
• Chelation[38,59]</td></tr>
</table>

Physical surface treatments primarily aim to change the physical properties such as the surface characteristics, morphology or crystallinity of the fibers without significantly affecting their chemical composition.[46] Among these, mechanical stretching is one of the simplest methods. It improves the mechanical properties of electrospun fibers by aligning the polymer chains along the fiber axis, leading to a reduction in fiber diameter along with an increase in crystallinity. These processes can also be supplemented by annealing.[10] Less invasive, though also less specific, are plasma treatments.[60] These introduce (depending on the plasma type) polar functionalities such as carbonyl, carboxyl or even hydroxyl groups onto the polymer fiber surface. In addition to the surface composition, biological, optical and electrical properties can also be altered without a significant impact on the polymer's bulk properties.[50] Beyond that, approaches using plasma can also be combined with chemical grafting reactions, since physical methods are often not efficient enough for an homogenous in-depth membrane functionalization.[38,46]

In addition, carbonization within a reducing atmosphere is another widely used physico-chemical method.[46] In over 90 % of cases, PAN fibers serve as polymeric precursors for the pyrolysis. The resulting electrospun carbon nanofibers feature a high specific surface area and good electrical conductivity, making them attractive materials for energy conversion/storage applications, sensory technology, catalysis as well as biomedical applications.[61] Besides physical and physicochemical approaches to functionalization, the class of chemical modification certainly offers the greatest variety. This involves chemical reactions that change the molecular structure of the fibers by creating new functional groups or splitting existing bonds. As shown in Table 2, this involves a number of methods, including crosslinking, wet chemical modifications and chelation.[51,52] Crosslinking is a versatile method for modifying electrospun fibers, which leads to a significant improvement in chemical resistance, thermal and mechanical performance.[62,63] But synergies can also arise between wet chemical methods. Oxidation using agents like potassium permanganate initially creates polar functional groups on the surfaces to prepare them for further conversion.[64] As an example, grafting polymerization can be named. During this process, polymer chains or other constituents grow to or from the surface of the fiber substrate.[60] This can be achieved either in a radical manner such as reversible addition-fragmentation chain-transfer polymerization (RAFT) or in a non-radical manner such as click reactions. Both open up multiple options for introducing different polymer nano- and microstructures.[38]

With regard to the development of flexible electronics, chemical modification through metallization is gaining a new significance. As a collective term, it once again encompasses numerous processes. In many cases, metal nanoparticles are first seeded on the fibers *via* dip-coating or sputtering. This is followed by electroplating a layer of metal.[57] In contrast to these fiber surface-orientated methods, another relevant approach involves the incorporation of metal nanoparticles (or other nanostructures) into the polymer matrix.[65] This proves to be of advantage considering that metal nanoparticles have unique electronic and optical properties compared to their bulk equivalents. These features depend on the size and shape of the nanoparticles and can thus be tailored.[66] One of the most remarkable shapes is that of nanowires (NWs). They stand out due to their extremely high aspect ratio of ≥ 1000:1 coupled with a diameter of just above one nanometer. This unique 1D crystalline geometry combines high conductivity, flexibility and mechanical robustness, which is of crucial importance for the development of flexible electronics.[67] For more than two decades, research has been fascinated by their features.[68] Numerous metals have been processed into nanowires in the past, for instance silver,[69] gold,[70] copper,[71] platinum[72] and nickel.[73]

In parallel, various synthesis routes for nanowires have been introduced, including template-supported growth (hard-template) and solution-based (soft-template) methods.[68] Figure 8 illustrates the differences between these two top-down respectively bottom-up synthesis routes.

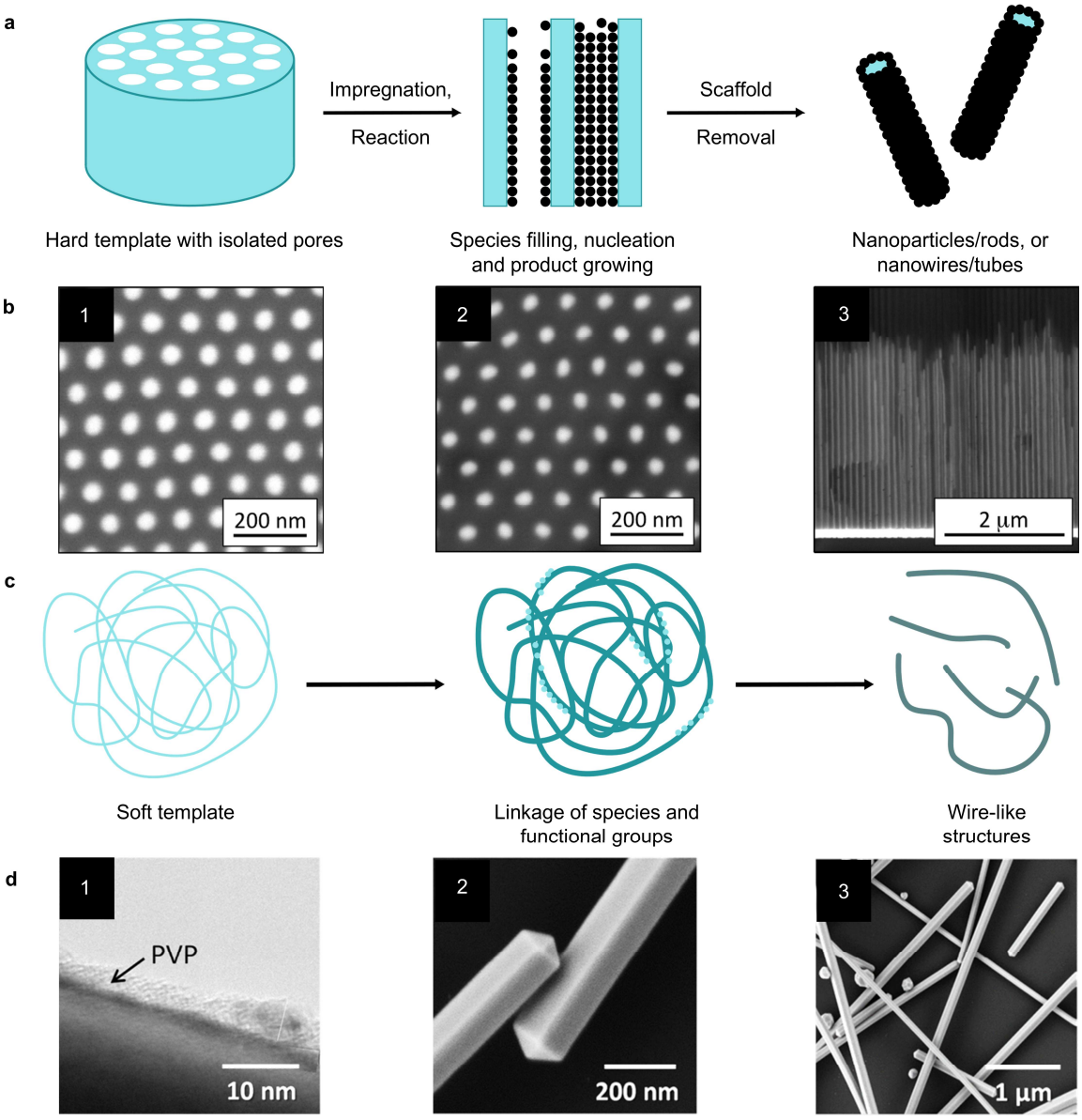

Figure 8: Illustration of the hard-template synthesis route for the creation of nanowires (**a**) with SEM images of the bottom (1,2) and the cross section (3) of CoNWs embedded in nanoporous alumina template (**b**) as well as an illustration of the soft-template synthesis for the creation of nanowires (**c**) with TEM (1) and SEM (2,3) images of AgNWs (**d**). (**a**,**c**) adapted from CHENG et al.,[74] (**b**) reprinted from PROENCA et al.[75] with the permission of AIP Publishing, (**d**) reproduced from BARDET et al.[76] (published under the terms and conditions of the CC BY license 4.0).

Template-assisted methods use porous membranes made of anodic aluminum oxide, mesoporous oxides or CNTs,[77] controlling the growth, shapes and sizes of the nanowires.[78] Their pores serve as a confining space in which the metal ions are (electro)chemically reduced. Even though the resulting nanowires are highly ordered and regular in shape, template removal is usually challenging and can damage the nanowire structure. In this context, soft-template approaches appear to be beneficial since they are known to be reproducible and easy to scale.[68]

A prominent example of this is the polyol method, which is widely used for synthesizing AgNWs. During the preparation, the metal salt (e.g. $AgNO_3$) is dissolved in a polyol (e.g. ethylene glycol) together with a polymeric ligand (e.g. PVP). The latter then serves as a soft template for the controlled growth of the forming seeds during heating. Due to the preferential adsorption of PVP on certain crystal facets (see Figure 9), the reduction of silver can only take place from one side resulting in defined nanowires.[79,80]

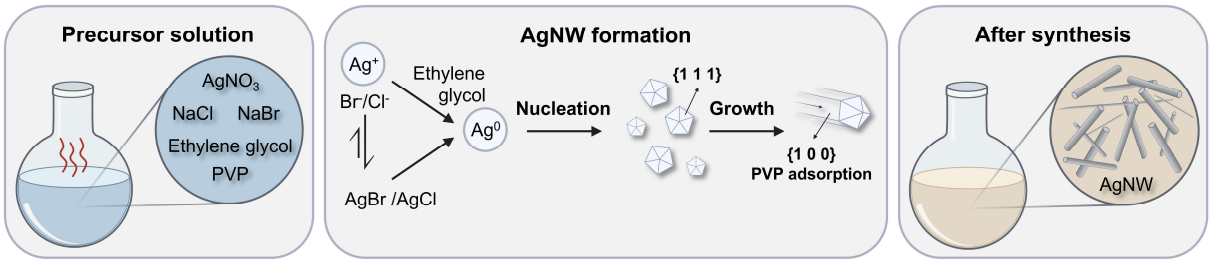

Figure 9: Formation of AgNWs according to the polyol synthesis route (adapted from SILVA et al.).[80]

These AgNWs have a unique combination of qualities that make them attractive for application. Among these is their outstanding conductivity, as bulk silver has the highest electrical and thermal conductivity of all metals.[68,81] It also exhibits relatively high oxidation stability.[82] With the synthesis route just described, AgNW can ultimately be customized in various forms and lengths for an application at low cost.[68] The 1D wire geometry opens up new possibilities for efficiently constructing percolation paths when embedded in (polymer) matrices.[67] This can either be realized by dip-[81,83] or spray-coating of the respective substrate with AgNW resulting in a network of AgNWs attached on the surface,[84] or by mixing the AgNWs together with their matrix before processing.[85] The latter can involve processing by means of film casting, extrusion as well as electrospinning into films,[82,86] yarns,[65,87] nonwovens[88] or other architectures.[89] The resulting structures are promising for application as self-sustaining devices in energy storage systems, solar cells, wearable electronics or even flexible displays.[90] Beyond enabling the development of new device types, they also compete with established products. Transparent AgNW-based conductive films are the most promising substitutes for indium tin oxide in displays, as they circumvent the problem of indium scarcity.[69] The establishment of such new materials, though, causes further challenges in addition to the initial problems of scalability and production costs. In addition to the chemical, mechanical and thermal stability of AgNWs, these include above all the compatibility and behavior of the nanowires with their matrix.[91] A closer look reveals that the contact resistances between the nanowires have a significant influence on the overall conductivity of the network. For an optimization of these junctions, a deepened understanding of the complex interactions between the nanowires is necessary.[92]

1.3 Thermal transport in fiber materials

In the past, fiber materials were mainly used for their heat-insulating properties (e.g. in the form of protective clothing).[93] With the approach of developing wearable devices for personal thermal management, further features of textiles become relevant.[94,95] This includes the efficient dissipation of heat from a heat source or its homogeneous distribution over a surface.[96] An overview of the underlying heat pathways and heating or cooling mechanisms of these cloths is given in Figure 10.[95]

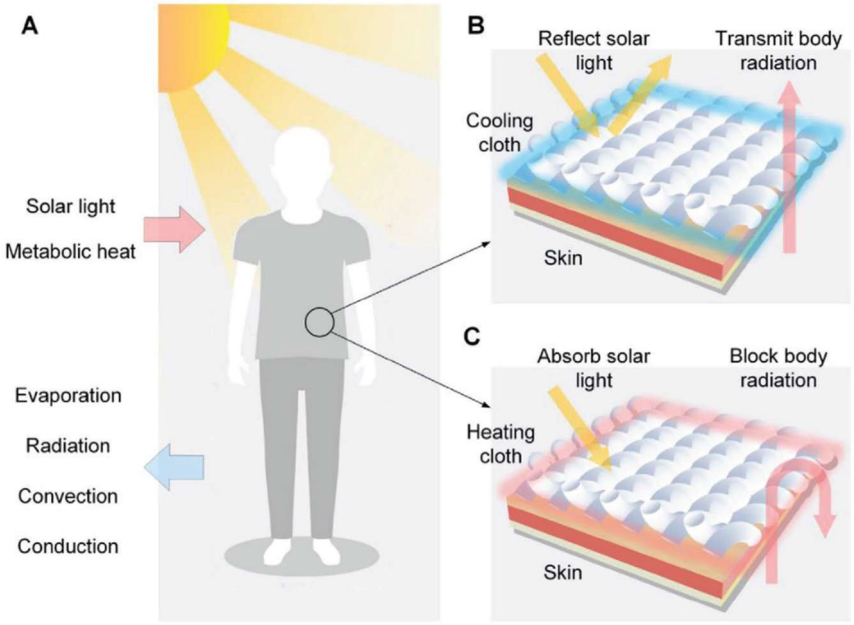

Figure 10: Illustrations of heat input (colored in red) and output pathways (colored in blue) for the human body (**a**), as well as of a cooling textile that reflects solar light and transmits body radiation (**b**) and of a heating textile that absorbs solar light and blocks body radiation (**c**). Reprinted from HU et al.[95] with permission from John Wiley & Sons.

The ability to characterize and control the thermal pathways within fiber materials is crucial for optimizing the performance in their applications.[97] There are several ways of expressing thermal transport in physical terms. Thermal conductivity is a key characteristic and describes the transfer of thermal energy between neighboring particles. While temperature indicates the extent of particle vibration, heat (which is closely tied to thermal conductivity) quantifies the amount of energy transferred, the rate of transfer, and its direction. FOURIER's law defines the heat flow (Φ) through a material as a function of the temperature gradient (dT/dx) and the thermal conductivity (κ) and thus establishes a proportionality between these variables.[98]

$$\Phi = -\kappa S \frac{dT}{dx} \tag{1}$$

Φ: heat flow rate, κ: thermal conductivity, S: surface area, dT/dx: temperature gradient.

For further description of thermal transport, the thermal diffusivity α can be utilized. This parameter considers not only the thermal conductivity (κ), but also the specific heat capacity (C_p) and the density (ρ) of the material. It is therefore a measure for the speed of heat propagation in a structure.[98]

$$\alpha = \frac{\kappa}{C_p \cdot \rho} \tag{2}$$

α: thermal diffusivity, κ: thermal conductivity, C_p: specific heat capacity, ρ: density of the material.

Thermal conductivity and heat transport are strongly influenced by material properties.[99] Crystallinity is one of the relevant factors. Crystalline materials generally have a higher thermal conductivity than amorphous materials.[98] This difference arises from the distinct heat transfer mechanisms in each type. In crystalline materials, heat is primarily conducted by phonons (lattice vibrations). In contrast, in (partially) amorphous materials such as polymers, additional mechanisms, including segmental rotations and intermolecular bonds, also contribute to heat transfer.[98,99] Besides, thermal conductivity also increases with increasing density. Porous materials therefore possess a lower thermal conductivity than compact materials, as the air in their pores is a poor conductor of heat.[97] There are various ways to influence thermal transport. For instance, a preferential orientation in the structure can have a significant impact,[96] while the use of fillers and additives offers additional opportunities to tailor thermal conductivity.[99]

As shown in Figure 11, there are different methods for analyzing thermal behavior, depending on the type of material. These may vary in their principles, areas of application and accuracy. The available techniques can be divided into two main categories, namely steady-state and non-steady-state methods. [100]

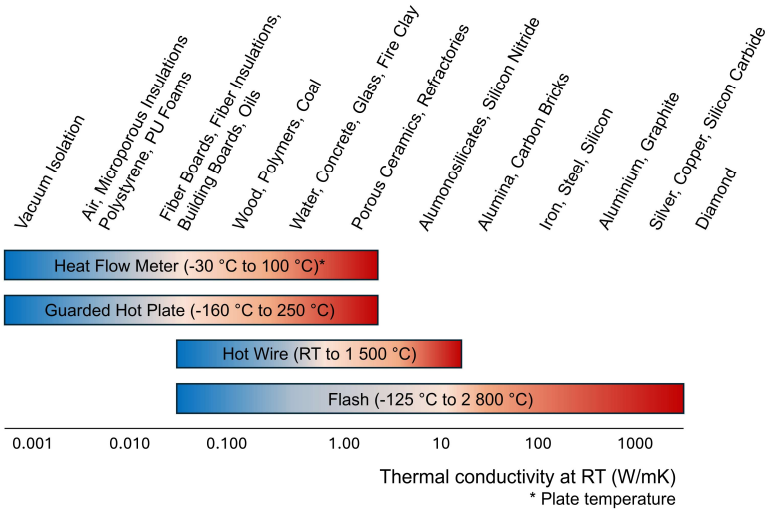

Figure 11: Comparative overview of the measuring range of thermal analysis methods together with different material classes (adapted from [101]).

The former methods refer to FOURIER's law of heat conduction and measure thermal conductivity by generating a steady-state temperature difference across a sample of a known thickness.[100] The output signal within a measurement is then evaluated in relation to the applied heating power, complemented by absolute measurements of reference materials. Examples include the guarded hot plate as well as the heat flux meter method.[99] These techniques are generally suitable for non-metallic materials such as insulating materials, polymers, glasses or ceramics. Although these methods are mathematically simpler and generate more accurate results, they are more time-consuming, as a stationary state must first be established within the sample. This is one of the reasons why non-steady-state methods have proven to be more advantageous. After all, these techniques track the sample behavior during the heating process and use this to determine thermal conductivity characteristics. The measurements can thus be conducted rather quickly and can also cover a wide range of sample types (from non-conductive to conductive). Examples of these techniques are the hot wire or laser flash method.[100] Both methods are transient methods in a narrow sense, as the sample is exposed to a single heating event. By analyzing the time-dependent temperature fluctuation, conclusions can be drawn about the thermal transport properties. However, the category of non-steady-state analysis methods also includes quasi-steady-state methods. Here, the sample is subjected to periodic heat excitation so that its temperature response can be analyzed within the frequency domain. One representative of this group is Lock-In Thermography (LIT).[102] The following Figure 12 illustrates the set-up of this technique.[103]

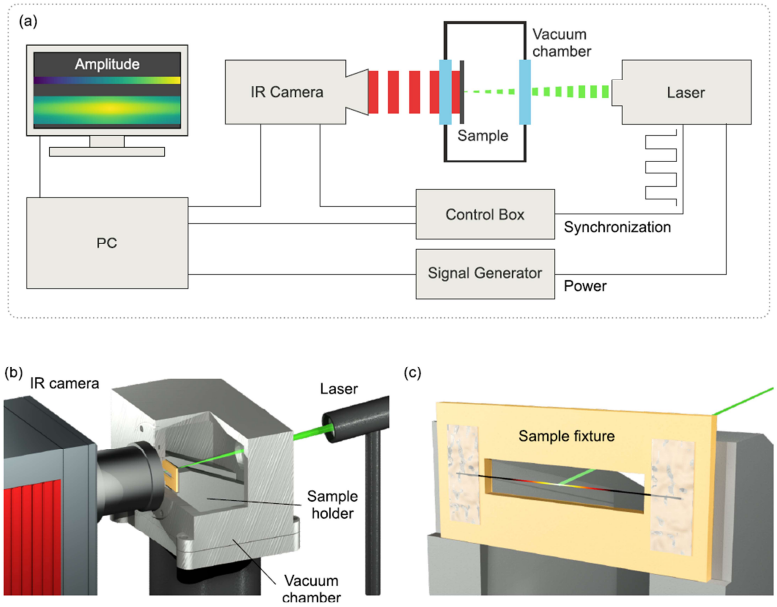

Figure 12: Illustration of a Lock-In Thermography set-up consisting of a modulated laser, that periodically heats the sample, an IR camera that detects the temperature distribution and a computer that converts the signals into phase and amplitude images (**a**), close-up of the vacuum chamber that holds the sample in between the laser and the camera (**b**) as well as a single fiber being attached on a sample holder that is hit by the laser beam (**c**). Reprinted with permission from TRAN et al.[103] Copyright © 2022, American Chemical Society.

Lock-In Thermography is a versatile and powerful method for non-destructive in-plane analysis of thermal properties of materials like thin films and fibers. During the measurement, a modulated laser serves as a periodic heat source for the probe in the sample chamber. An IR camera mounted behind the probe specimen detects the temperature response of the sample to the heat excitation (see Figure 12b). The resulting time-dependent temperature distribution is then converted into the amplitude and phase of the temperature oscillations by a FOURIER transformation. From this data, the thermal diffusivity can then be determined.[103] In combination with the specific heat capacity and the density, and with the aid of Equation 2, the thermal conductivity of a material can also be calculated.[104] Thus, this technique not only allows the visualization of the temperature distribution on the surface of the sample but also a quantitative determination of various thermal parameters.[102] A special feature is the sample geometry, as the measurement takes place in-plane of thin layers, even if these are semi-transparent. This makes it suitable for fibers and, depending on the resolution of the camera, also for microfibers. Since conventional approaches often struggle to assess the thermal properties of individual fibers with very small diameters, Lock-In Thermography has proven to be an attractive solution.[103]

2 Motivation and aim of the thesis

Thermal transport and management have become central challenges for diverse sectors of modern civilization. The importance of this topic is emphasized by the increasing demand for efficient thermal regulation in response to rapid technological advancement, urbanization, and the ongoing effects of global warming.[105] Innovative solutions need to address these challenges across multiple length scales. At the microscale, the ongoing miniaturization of microelectronic devices intensifies heat dissipation issues, necessitating advanced cooling strategies to maintain device performance and longevity.[106,107] On the macroscale, effective thermal management is crucial in urban environments, where rising temperatures and dense infrastructure drive the need for integrated systems - ranging from textiles to advanced building materials - to enhance comfort and sustainability. Fiber-based materials offer versatile and scalable solutions that can be tailored to meet thermal management requirements at both micro- and macroscopic levels.[108]

This thesis aims to construct percolative networks within the hierarchical confinement of fiber architectures, advancing the understanding of how local structure influences global energy transport - an essential foundation for developing multifunctional devices with tunable transport properties. The work systematically explores all three spatial dimensions of fiber architectures, utilizing the versatile processing technique of electrospinning for nanofiber creation. AgNWs were selected as the percolation mediator due to their outstanding combination of conductivity, flexibility, and suitability for scalable processing.[109] The study further addresses the critical roles of filler geometry, distribution and interfacial properties in achieving efficient thermal transport within composite systems.

The work is structured into three main chapters, each exploring distinct dimensionalities and strategies for incorporating AgNWs into fiber architectures, as illustrated in Figure 13. Hereby, percolation serves as the recurring and guiding theme through all chapters.

In the first chapter, 1D PAN yarns were fabricated with varying stretch ratios. The subsequential coating with AgNWs highlights the initial challenges of integrating anisotropic nanofillers into layered 1D composites and the effects on percolation behavior.

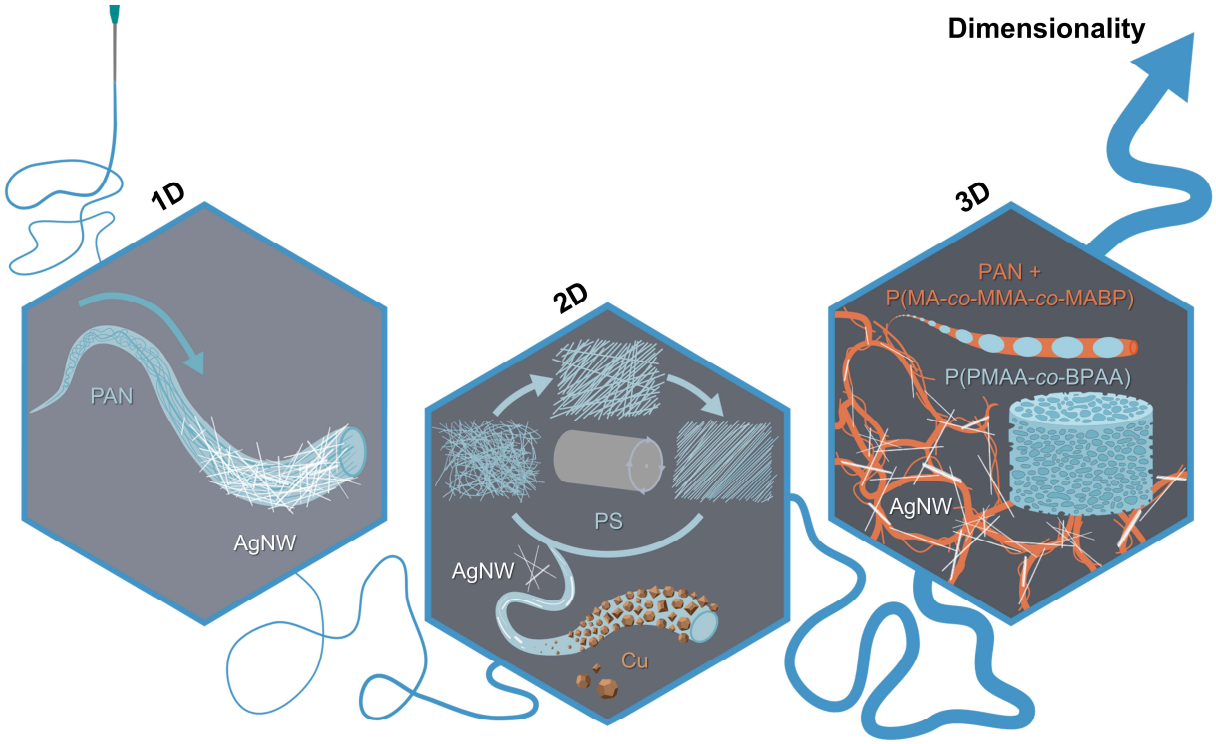

Figure 13: Overview of the content of the thesis, starting with the realization of 1D PAN yarns exhibiting various stretch ratios and functionalization with AgNWs. This is followed by the fabrication of 2D PS nonwovens with controlled fiber orientation and either internal (AgNW) or external (Cu) metallization. Finally, 3D BOS sponges composed of short fibers, homogenously decorated with AgNWs, were produced. This structural diversity created by electrospinning forms the foundation for a comprehensive investigation of the structure-property relationship with special focus on their thermal transport behavior.

The second chapter expands the dimensionality to 2D PS nonwovens, where fiber orientation could be precisely controlled during processing. Here, both the alignment of fibers and the targeted incorporation and alignment of AgNWs within the fiber matrix were achieved, enabling internal fiber metallization. This was further complemented by external copper functionalization, resulting in nonwovens with varying degrees of orientation and surface properties, providing valuable insights into the contributions of matrix and filler on global thermal transport.

The third and final chapter introduces 3D sponges assembled from short electrospun BOS fibers. This morphology enhances mechanical stability and facilitates AgNW attachment. A novel composite sponge preparation method led to a distinct arrangement of AgNWs along pore walls and reveals the evolving challenges of achieving efficient percolation as the system transitions from 2D to 3D architectures.

The thesis systematically explores the principles of coating, aligning, and spacing AgNWs within hierarchical fiber systems, with a focus on how matrix dimensionality and nanofiller integration strategies influence percolation and thermal transport.

3 Results and discussion

Throughout this work, Ina Klein (Physical Chemistry I, Prof. Dr. Markus Retsch) carried out the thermal analyses and evaluations, as well as the determination of orientation parameters within the fiber structures.

3.1 1D yarns

The thesis begins with 1D yarns, where the term '1D' in the fiber context refers to a macroscopic yarn composed of many twisted nanofibers. Although this represents the simplest geometry, the production of continuous nanofiber yarns is technically demanding. After the fiber jet is formed, it is crucial to be reliably collected and twisted into a stable yarn bundle, a process that has prompted the development of various specialized techniques over time.[21] Here, an established set-up for yarn fabrication was adapted, and PAN was selected as the base material due to its excellent processability, versatility, and the broad range of functionalization options it offers. This includes post-processing treatment possible by pyrolysis leading to carbon fibers, which are highly valued for advanced applications in the fields of catalysis, sensors and nanoelectronics.[110] PAN's suitability is further emphasized by its ability to be functionalized through straightforward methods such as dip-coating or chemical grafting, enabling the integration of additional functionalities and performance enhancements.[111,112]

In this context, a combinatorial approach was established to produce 1D PAN yarns with controlled stretch ratios, which were subsequently functionalized with AgNWs (see Figure 14).

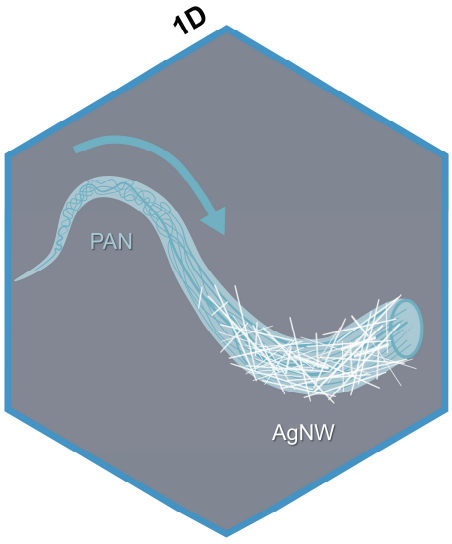

Figure 14: Overview illustrating the first chapter's content, starting with the realization of 1D PAN yarns exhibiting various drawing degrees and their functionalization with AgNWs.

The functionalization strategy unites two established approaches - chemical grafting and dip-coating - to integrate AgNWs into PAN yarns, as illustrated in Figure 15.

Leveraging PAN's inherent reactivity, branched poly(ethyleneimine) (*b*-PEI) is first grafted onto the fiber surfaces adapting a literature-known method involving thermal treatment in ethylene glycol.[112,113] This step introduces amine-rich anchoring sites that enable strong interfacial interactions with AgNWs during subsequent dip-coating. The PEI grafting shall therefore not only enhance the hydrophilicity of the PAN yarn but also provide anchoring groups to stabilize the AgNWs, with the intention to minimize detachment during mechanical stress. While recent studies from SHAO et al. have employed dip-coating alone to deposit both PEI and AgNWs through physical adsorption,[111,114] this work advances the approach by chemically anchoring PEI *via* covalent bonding before introducing AgNWs through dip-coating.

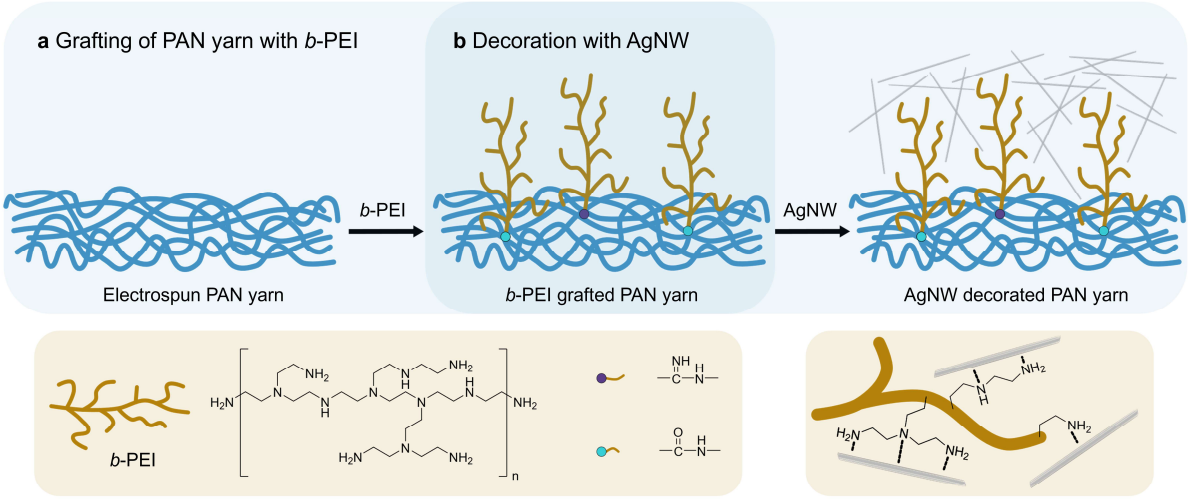

Figure 15: Illustration of the two-step 1D PAN yarn modification and functionalization: starting with the grafting of the electrospun yarn with *b*-PEI (**a**). This is followed by the decoration with AgNWs in a second step (**b**).

This synergy aims to improve interfacial stability but in fact reveals inherent limitations of dip-coating of anisotropic fillers in confined geometries.

3.1.1 Yarn preparation

Multifibrillar yarns were prepared using a custom-made electrospinning device equipped with two oppositely positioned syringes, a fiber-collecting funnel, and a winder collector, as depicted in Figure 16a. During electrospinning, commercial PAN (copolymer containing ~ 6 wt% methyl acrylate) dissolved in DMF was processed. Further analytical data on the spinning material can be found in Chapter 5.1 (see Table 6) and Chapter 7 (see Figure 60a). The yarns collected directly from this set-up are designated as ‘as spun’. To enhance the alignment of the individual nanofibers within the yarn bundle, a subsequent heat stretching procedure was applied. The ‘as spun’ yarns were drawn through a tube oven at 150 - 160 °C without further mechanical stretching at first, yielding what was referred to as ‘annealed’ yarn.

This step was included to later elucidate the influence of annealing on the thermal properties of the various yarns. Due to the semicrystalline nature of PAN, it means that thermal treatment can significantly affect molecular orientation, crystallinity, and thus the heat transport behavior. For additional alignment, the yarns were extended to twice and three times their original length, resulting in samples labeled ‘x2’ and ‘x3’, respectively. This nomenclature is used throughout the following discussion to distinguish between the different processing states. Further stretching with this physical modification approach beyond three times the original length was not feasible due to frequent rupture of the yarns.

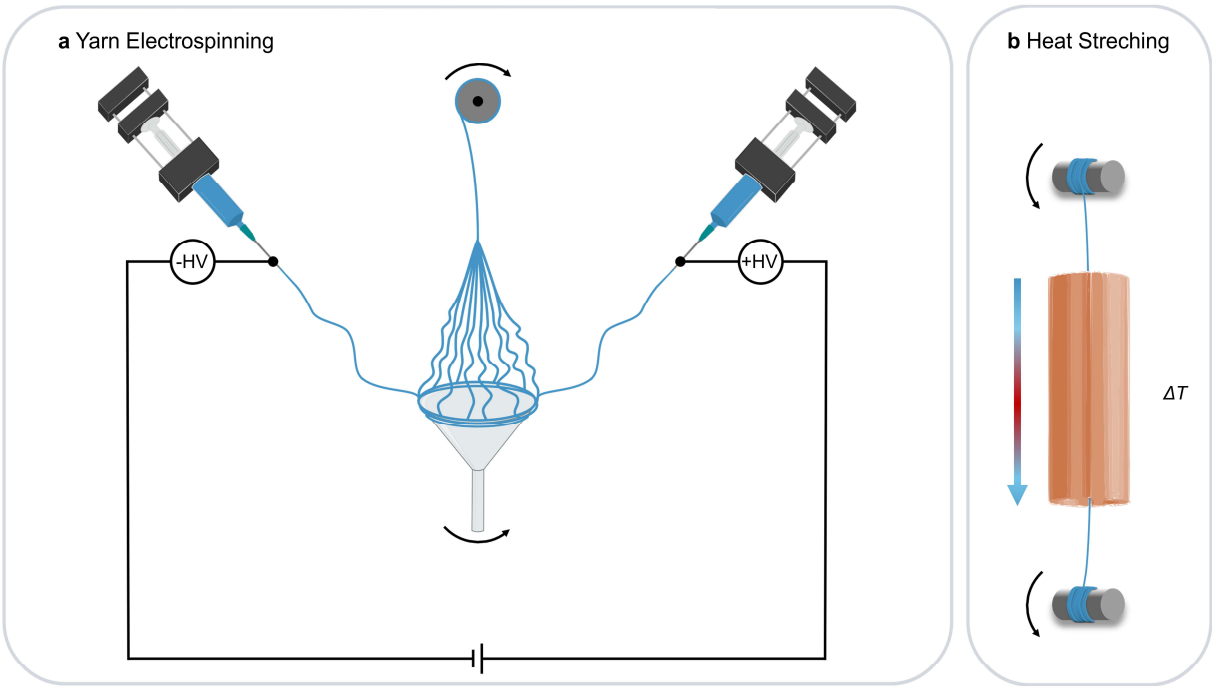

Figure 16: Illustration of the Yarn Electrospinning set-up consisting of two syringes fixed opposite to each other in the set-up, with the fiber-collecting funnel device and the winder collector in between (**a**) as well as the Heat Stretching device equipped with two winding motors feeding the yarn through the tube oven at different winding motor speeds to create different stretch ratios (**b**).

Figure 17 presents SEM images of the various yarn types, illustrating the decrease in both yarn diameter and the diameter of individual nanofibers as the stretch ratio increases. Each yarn visible in the images is composed of numerous individual nanofibers, which collectively form the structure of the macroscopic yarn. This multifibrillar architecture dominates the properties of the yarn, as interactions and the spatial arrangement of the single fibers determine the overall mechanical behavior and functional characteristics. Upon stretching, the fibers become increasingly aligned along the yarn axis, appearing straighter and less twisted compared to the initial, as spun state - a result of the rotational forces applied during twisting. Consequently, the yarns are getting more compact and less fluffy, reflecting the enhanced alignment and densification achieved through stretching.

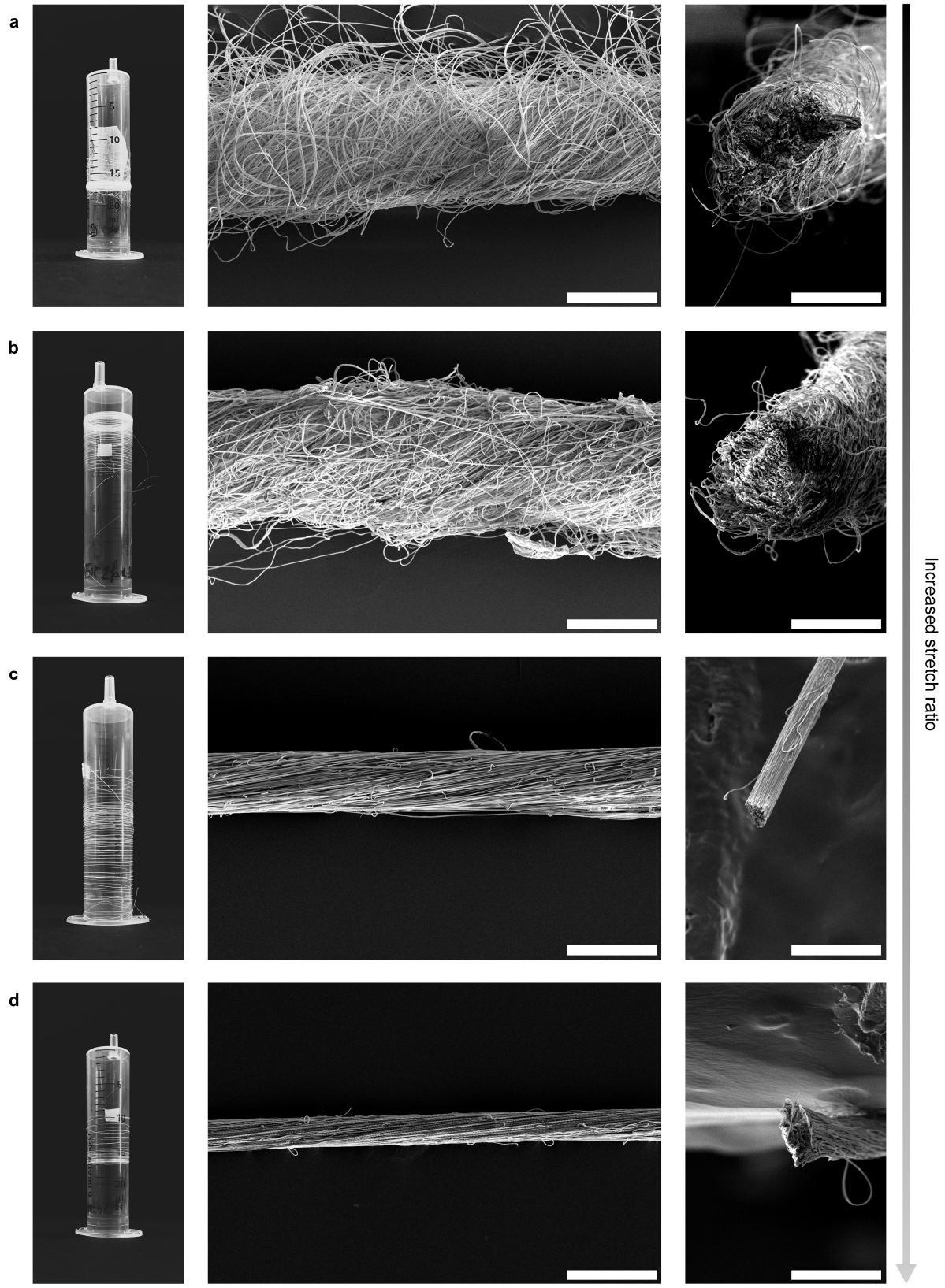

Figure 17: Optical images of the yarn-loaded syringes and corresponding SEM images (top view and cross section) of neat 1D PAN yarns in the as spun (**a**), annealed (**b**) as well as x2 (**c**) and x3 stretching state (50 µm scale bar) (**d**).

Yarn diameters and individual fiber diameters were determined from the SEM images, with all values compiled in a summarizing table in Chapter 7 (see Table 19).

Both parameters remain relatively consistent for the as spun and annealed yarns but decrease significantly at higher stretch ratios. The yarn diameter exhibits a more pronounced reduction compared to the fiber diameter, which only decrease noticeably at the highest stretch ratio (x3), as shown in Figure 18a.

Additionally, the orientation parameter S_{2D} was calculated from the SEM images (for procedure see Chapter 5.1 - SEM and Chapter 7, Figure 61) by Ina Klein (Physical Chemistry I, Prof. Dr. Markus Retsch). This parameter quantifies the fiber alignment within the yarns, where 0 indicates complete randomness and 1 represents perfect alignment. Due to limited image availability only one image per yarn type was evaluated (see Chapter 7, Table 19). Therefore, no standard deviations could be calculated, but the S_{2D} values in Figure 18b still reveal a striking trend: the initially aligned nanofibers in the as spun yarn achieve near-perfect alignment at higher stretch ratios, underscoring the effectiveness of the stretching process in enhancing structural order.

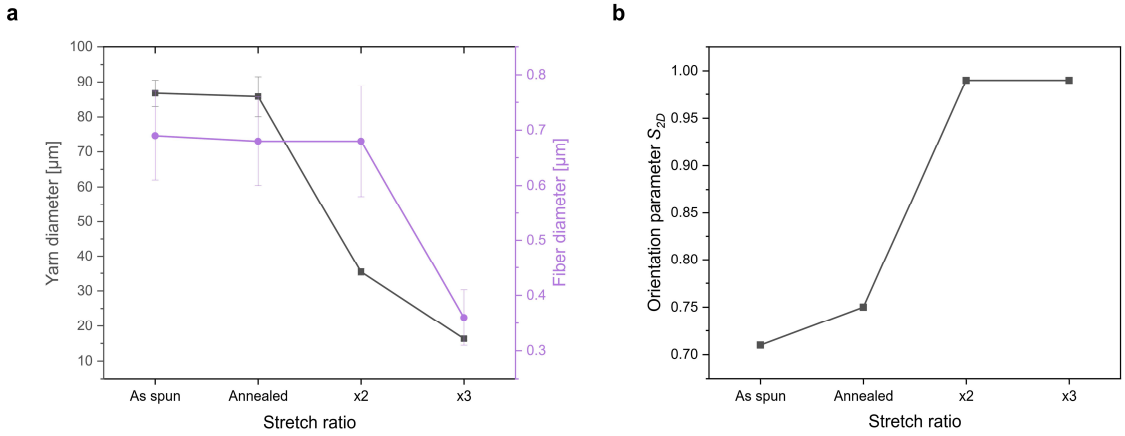

Figure 18: Yarn and fiber diameter of neat 1D PAN yarns (**a**) as well as the orientation parameter S_{2D} as a function of stretch ratio (**b**).

The impact of variations in diameter and orientations are further analyzed in terms of mechanical performance (summarized in Chapter 7, Table 20). According to PEIRCE's theory, the reduction in yarn diameter with stretching decreases the probability of defects, thereby enhancing strength - a phenomenon that was also previously demonstrated for electrospun PAN yarns by SHAO et al and BRENNAN et al.[114–116] However, as shown in Figure 19b, this set of yarns exhibits partially nonlinear behavior: the maximum force before failure F_{max} initially rises with stretching but plateaus beyond the x2 stretch ratio, while elongation at break ε_b demonstrates a continuous decline as expected. Concurrently, the YOUNG's modulus E_{mod} peaks at the x2 stretch ratio, reaching values over ten times higher than those of the as spun yarn (see Figure 19c).

This trend for F_{max} and E_{mod} suggests an optimal stretch ratio - here identified as x2 - where near-perfect alignment is already reached and maximizes the mechanical performance. Beyond this threshold, excessive thinning compromises mechanical stability despite minimal gains in fiber alignment. Still, the modulus (13.2 GPa) and maximum force before failure of 342 MPa achieved at the x2 stretch ratio fall within the range reported for conventional electrospun PAN yarns in studies using similar thermal stretching protocols.[114,116] However, direct quantitative comparisons remain challenging due to variations in yarn diameter, fiber alignment methodologies, and processing conditions across studies.

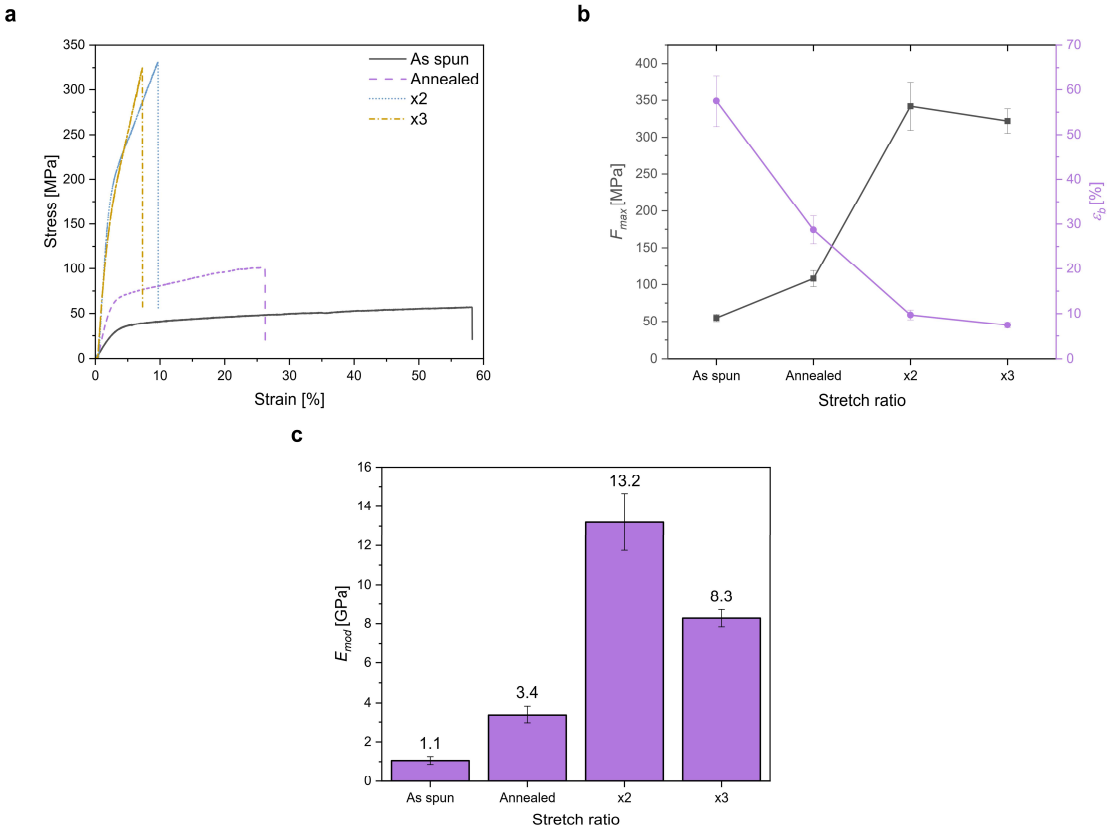

Figure 19: Mechanical analysis of neat 1D PAN yarns: stress-strain plots (**a**), maximum force before failure F_{max} as well as elongation at break ε_b values (**b**) and YOUNG's modulus E_{mod} as a function of stretch ratio (**c**).

The mechanical performance of the yarns is closely connected to their degree of crystallinity, which was analyzed using XRD. This was done by Patrick Länger (Inorganic Chemistry III, Prof. Dr. Jürgen Senker). For these measurements, the yarns were wound around a capillary, though this sample preparation introduced certain challenges. The resulting diffractograms, shown in Figure 20, exhibit a high signal-to-noise ratio, which limits the analysis to a qualitative discussion of the diffraction peaks. Characteristic reflections for PAN in a hexagonal cell - specifically at $2\theta \approx 17$ ° for the (100) plane and 29.5 ° for the (110) plane - serve as indicators for crystalline content (highlighted in blue in Figure 20).[117]

The as spun yarn display the lowest crystallinity, which can be attributed to the rapid solution processing that limited molecular ordering. Annealing leads to a significant increase in crystallinity, with the annealed yarn showing the most pronounced crystalline features, including a faint (101) peak - consistent with its longest residence time in the tube oven.[117] In contrast, yarns subjected to stretching (x2 and x3) spent less time in the oven, resulting in lower crystallinity for x3 compared to x2. This trend explains why the x2 yarn exhibited the best mechanical properties: it combines high nanofiber alignment with a comparatively high degree of crystallinity, both of which are known to contribute to superior strength and modulus in semicrystalline systems like PAN.[116]

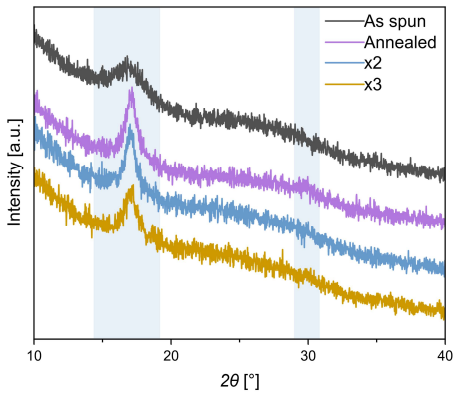

Figure 20: Normalized XRD diffractograms of the different neat 1D PAN yarns. The blue areas highlight the characteristic reflections for PAN in a hexagonal cell at $2\theta \approx 17$ ° (100) and 29.5 ° (110).[117]

Due to their anisotropic 1D geometry, thermal analysis of the yarns was experimentally limited. As introduced in Chapter 1.3, LIT is employed to quantify the thermal diffusivity α by analyzing phase and amplitude profiles of in-plane thermal propagation (see Chapter 1.3, Figure 12 for set-up and Chapter 7, Figure 62 for measurement details). While the methodology is robust for homogenous materials, the twisted, multi-filament structure of the PAN yarns introduced measurement complexities, particularly after AgNW functionalization (see Chapter 3.1.3). As such, the results should be regarded as indicative of general trends only.

Initial measurements, performed by Ina Klein (Physical Chemistry I, Prof. Dr. Markus Retsch), on neat yarns considered both phase and amplitude-phase product evaluations, yielding closely matching α values (summarized in Chapter 7, Table 20). The measured thermal diffusivities in Figure 21a and b exhibit a clear trend: diffusivity increases with stretch ratio, before plateauing between x2 and x3, consistent with the mechanical performance behavior. This correlation underscores the interplay between nanofiber alignment, crystallinity, and thermal transport.

Higher stretching enhanced alignment and crystallinity up to x2, while excessive stretching (x3) reduced crystallinity and disrupted interfacial bonding, diminishing both thermal and mechanical properties. These findings reinforce the hypothesis that the x2 stretch ratio represents the critical balance between structural order and process-induced defects in the presented PAN yarn system.

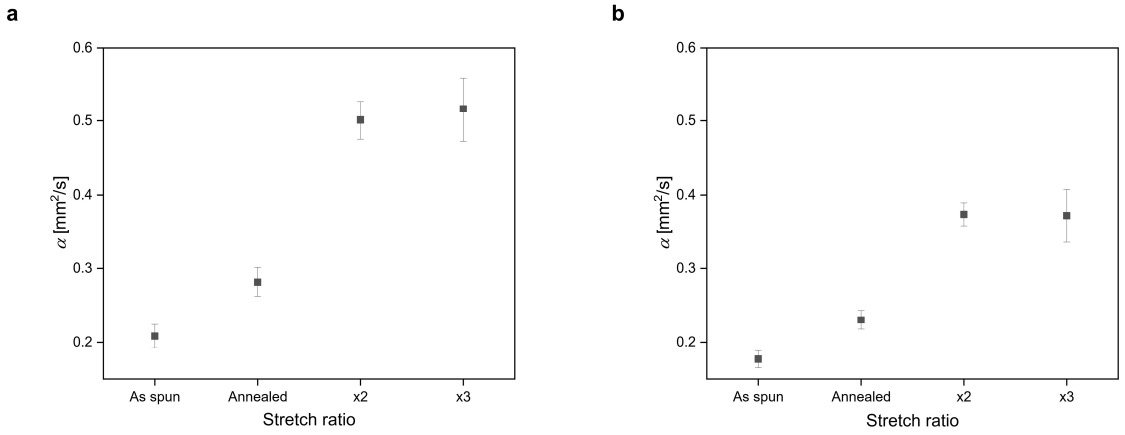

Figure 21: Thermal diffusivity α determined from phase (**a**) and amplitude-phase product evaluations resulting from LIT as a function of stretch ratio (**b**).

These 1D PAN yarns provide a well-characterized selection for the subsequent modification with PEI, enabling their transformation into AgNW composite yarns in the following chapters.

3.1.2 Yarn modification

The chemical modification of 1D PAN yarns was performed using a literature-established grafting method, adapted from previous work on 2D PAN nonwovens. [112,113] The chemical modification of acrylic textiles *via* grafting has gained significant interest due to its versatility in introducing new functionalities and enhancing material performance. It enables the introduction of specific functional groups onto the PAN backbone, which can dramatically improve properties such as hydrophilicity, dyeability and adsorption capacity.[113,118] Here, *b*-PEI was grafted onto the PAN yarn surface, as depicted in Figure 22. This polymer contains primary, secondary, and tertiary amine groups in hyperbranched architecture. The structural diversity enhances its capacity to stabilize metals *via* coordination, making it particularly effective for surface functionalization requiring robust chemical anchoring.[119]

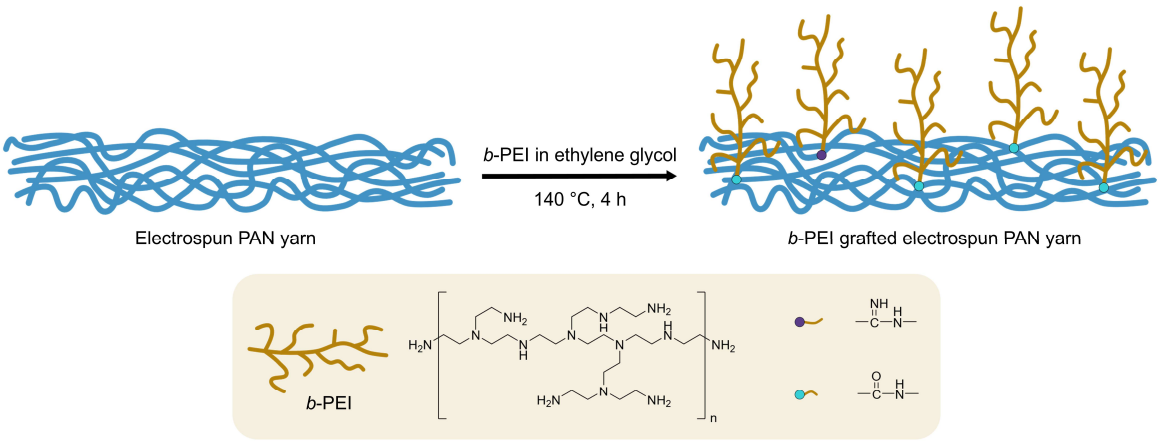

Figure 22: Illustration of the proposed 1D PAN yarn modification process: the grafting of neat electrospun yarn with *b*-PEI dissolved in ethylene glycol at elevated temperatures (adapted from ZHAO et al.).[113]

The modification was performed simultaneously for all four different yarn types from the previous Chapter 3.1.1 and resulted in a distinct color transition from white to yellowish (see Chapter 7, Figure 63). This shift aligns with literature reports of PEI-grafted PAN systems.[112,113] Due to the yarns geometry and limited quantity, 2D PAN nonwovens were prepared as reference (applying similar processing and modification conditions). FT-IR analysis of the reference nonwovens reveal spectral changes (see Figure 23a). Notably, the prominent band at 1660 cm^{-1} - associated with C=O stretching vibrations from amides, vanishes entirely. This band most likely arises from remaining DMF, that was still trapped within the nonwoven after processing.[120] Besides, the nitrile band at 2242 cm^{-1} and the ester carbonyl band at 1732 cm^{-1} (from the methyl acrylate comonomer) show reduced intensity but persist. Whitin the reaction, the PEI's primary amines could both react with the nitrile groups in PAN as well as with the ester functionalities from the methyl acrylate (favored) and form covalent amidine (-NH-C=N-) and amide groups (-NH-C=O) (see Figure 22), as previously demonstrated in analogous grafting studies.[112,113] The residual bands therefore imply incomplete conversion. Despite this finding, the modification significantly altered surface properties. Contact angle measurements show a dramatic hydrophilicity increase (see Figure 23b). The pristine nonwoven exhibited a contact angle of 111.4 °, while modified samples showed immediate water droplet penetration. This aligns with literature-known observations of PEI-grafted PAN systems, where introduced amine groups enhance polarity and hydrogen bonding capacity.[113] Such wettability is crucial for the subsequent AgNW functionalization, as it ensures uniform dispersion and adhesion. While the nonwoven's incomplete conversion highlights reaction limitations in 2D systems, the 1D yarns' smaller diameter and higher surface-to-volume ratio likely ensure sufficient grafting.

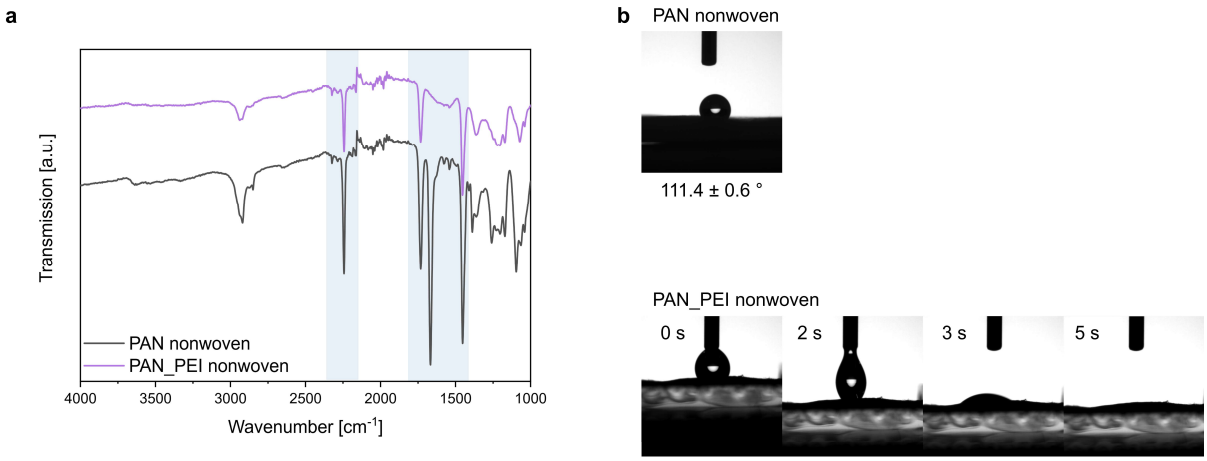

Figure 23: FT-IR spectra of 2D PAN nonwovens before and after PEI modification. The blue areas highlight the regions of structural change induced by the grafting reaction (**a**). On the right, optical images of contact angle measurements reveal the change in hydrophilicity created by the modification (**b**).

Additional elemental analysis of the modified 2D PAN nonwoven, conducted in triplicates, shows only a slight decrease in the carbon-to-nitrogen (C/N) ratio after grafting (see Table 3). This minor change can be explained by the relatively low molecular weight of the *b*-PEI used here (M_w 25 000) (for further analytical data see Chapter 5.1, Table 6 and Chapter 7, Figure 60b), which contrasts with literature reports where higher molecular weight *b*-PEI (M_w 250 000) resulted in a more pronounced increase in nitrogen content upon grafting.[113] This difference may also partially explain the subtle differences seen in the FT-IR spectra.

Table 3: Results of the elemental analysis of the different 2D PAN nonwovens.

Sample	C [%]	N [%]	H [%]	C/N	Sum
PAN nonwoven	64.25 ± 0.43	23.26 ± 0.37	5.74 ± 0.09	2.76	93.26 ± 0.73
PAN_PEI nonwoven	65.10 ± 0.48	23.89 ± 0.19	5.75 ± 0.11	2.72	94.74 ± 0.57

The SEM images presented in Figure 24 illustrate that the overall morphology of the PAN yarns remains largely unchanged after modification with branched PEI. However, a closer look at the images reveals that the modified yarns appear more loosely packed, with a less compact arrangement of individual fibers compared to the initial yarns (see Figure 17). This effect is particularly noticeable in the as spun and annealed samples, where the yarn structure seems to have become more open and less cohesive following the modification process. Such loosening is most likely a consequence of the solution-based grafting procedure, which can disrupt the integrity of the fluffier yarn assemblies and lead to a partial loss of the initial dense packing.

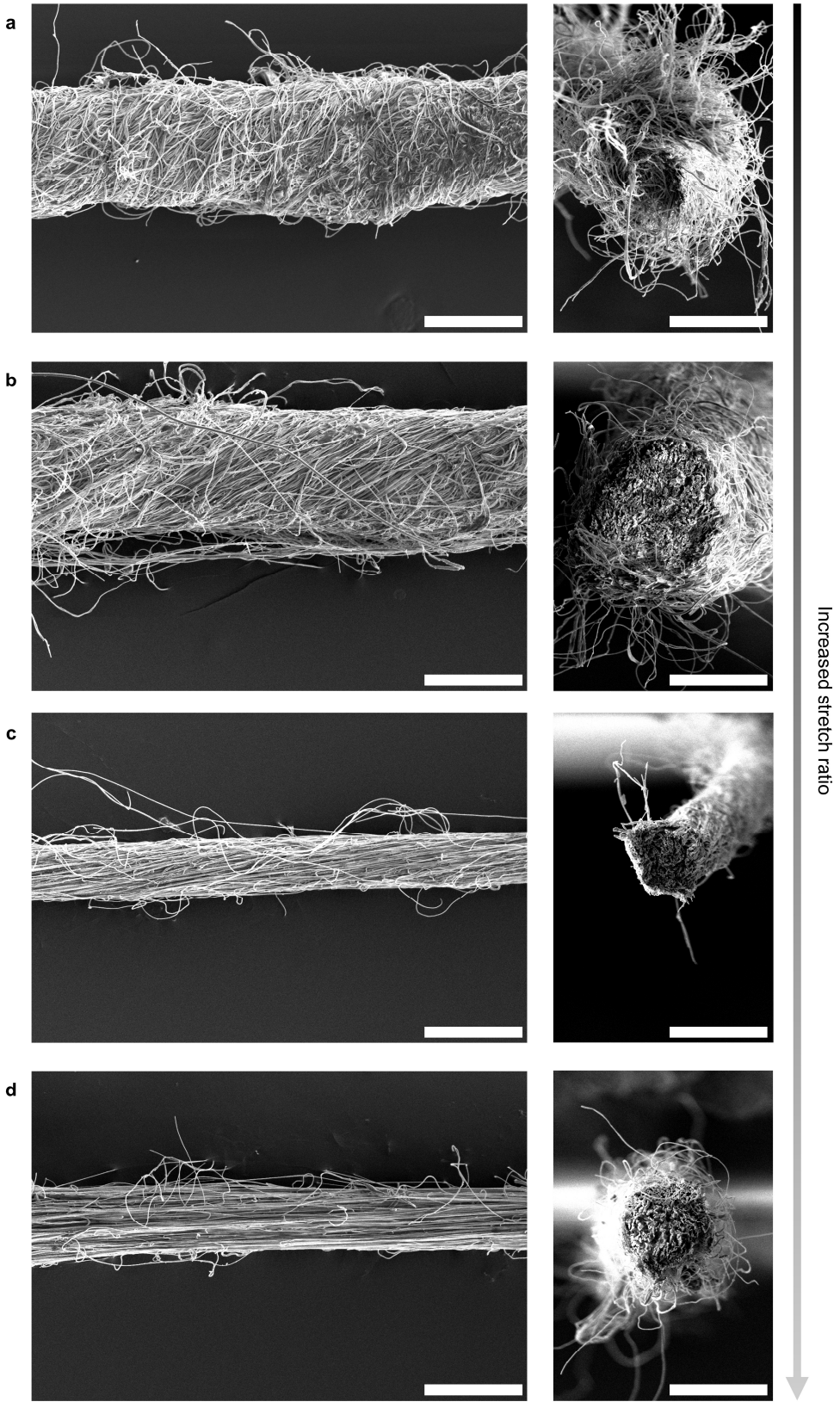

Figure 24: SEM images (top view and cross section) of PEI modified 1D PAN yarns in the as spun (**a**), annealed (**b**) as well as x2 (**c**) and x3 stretching state (50 µm scale bar) (**d**).

The orientation parameter, calculated by Ina Klein (Physical Chemistry I, Prof. Dr. Markus Retsch) for the PEI modified PAN yarns using the same methodology as for the unmodified 1D PAN yarns described in Chapter 3.1.1, highlights notable structural changes after modification. Figure 25b provides a direct comparison: the as spun yarns exhibit a drastic decrease in their orientation parameter following PEI grafting, indicating a significant loss in molecular alignment along the fiber axis. For the other yarn types, the reduction in orientation is less pronounced but still evident. This follows and quantifies the observation from the SEM images that the solution-based modification process disrupts the initial fiber arrangement, particularly in the as spun samples, likely due to swelling and partial relaxation of the nanofibers within the yarn bundle. The observed decrease in orientation is consistent with literature on post-processing and chemical modification of PAN fibers, where such treatments can lead to reduced fiber integrity and, consequently, changes in mechanical and functional properties.[114,118]

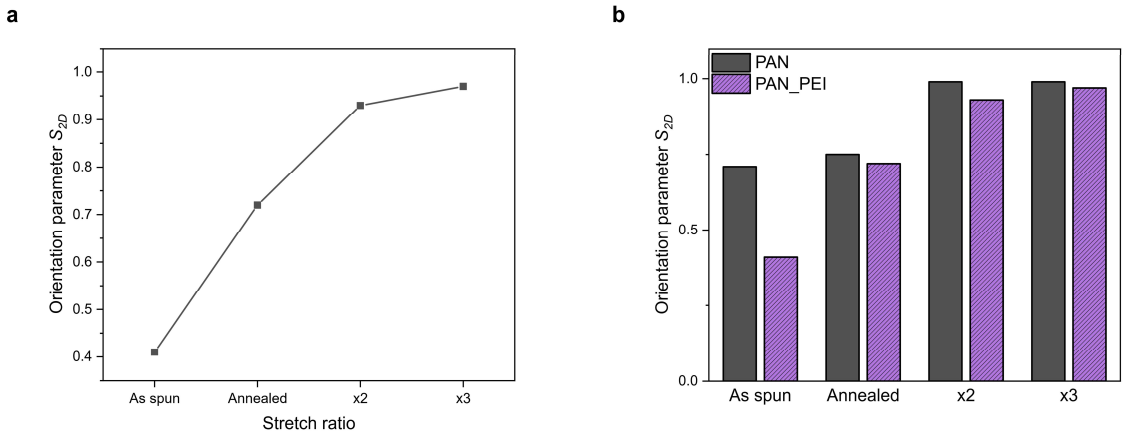

Figure 25: Orientation parameter S_{2D} of PEI modified 1D PAN yarns (**a**) as well as a comparison of the S_{2D} values before and after the modification as a function of stretch ratio (**b**).

Mechanical testing confirms that PEI modification leads to a decrease in the overall mechanical performance of the 1D PAN yarns. As detailed in Figure 26a, b and c (and summarized in Chapter 7, Table 20), all measured parameters - including maximum force before failure, elongation at break, and YOUNG's modulus - are consistently lower for PEI-grafted samples compared to their unmodified counterparts. For instance, the maximum force before failure drops by 29 % through modification (from 342 MPa to 242 MPa for the x2 yarn), while the YOUNG's modulus declines by 54 % (from 13.2 GPa to 6.1 GPa). This loss in mechanical performance is observed across all yarn types and is particularly pronounced in highly oriented samples.

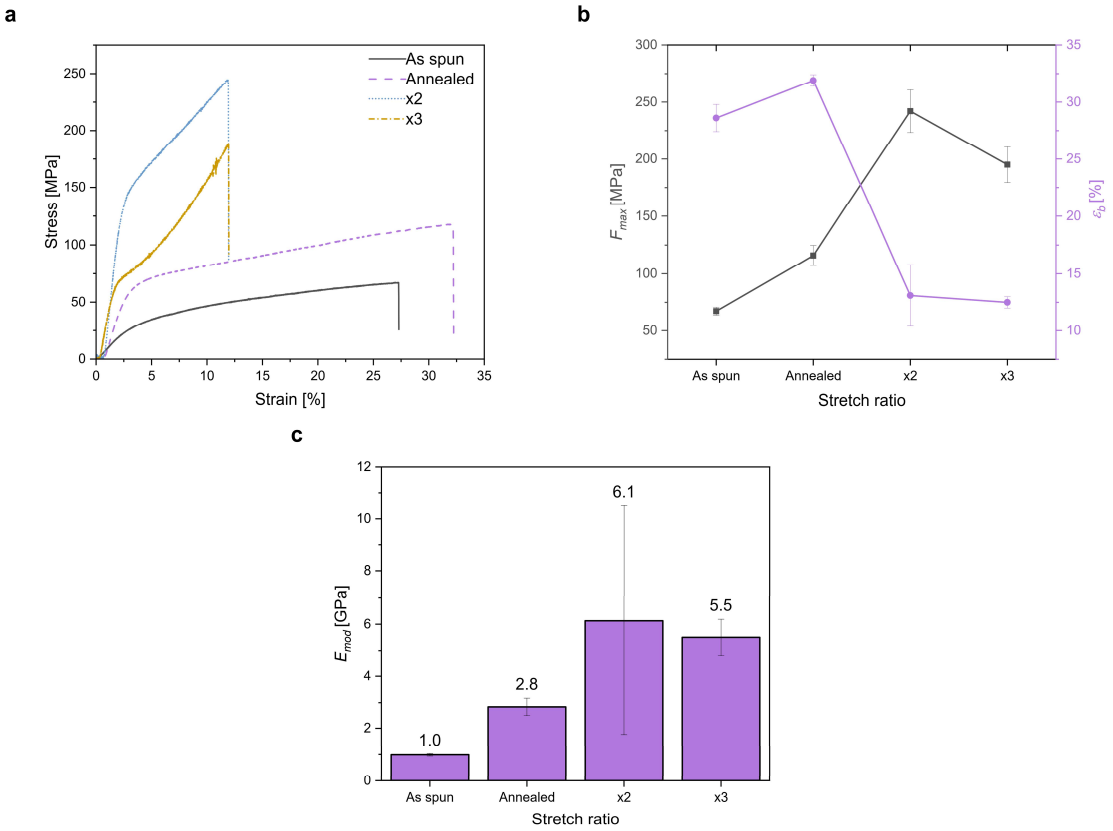

Figure 26: Mechanical analysis of PEI modified 1D PAN yarns: stress-strain plots (**a**), F_{max} as well as ε_b values (**b**) and E_{mod} as a function of stretch ratio (**c**).

The modification process introduces the necessary chemical anchoring sites for subsequent AgNW functionalization in the final section of this chapter. The introduction of branched PEI significantly enhances the surface reactivity and hydrophilicity of the PAN yarns - crucial for uniform AgNW deposition. But this benefit is accompanied by a notable reduction in mechanical stability. The trade-off between improved chemical functionality and diminished tensile properties underscores the challenges inherent in optimizing both surface chemistry and structural integrity during advanced fiber modification.

3.1.3 Yarn functionalization

The final step in the functionalization process involves the adsorption of AgNWs onto the PEI modified 1D PAN yarns, as depicted in Figure 27. This approach provides coordination and electrostatic binding sites for AgNWs - a strategy previously demonstrated to impart effective conductivity to electrospun nanofiber yarns.[111,114]

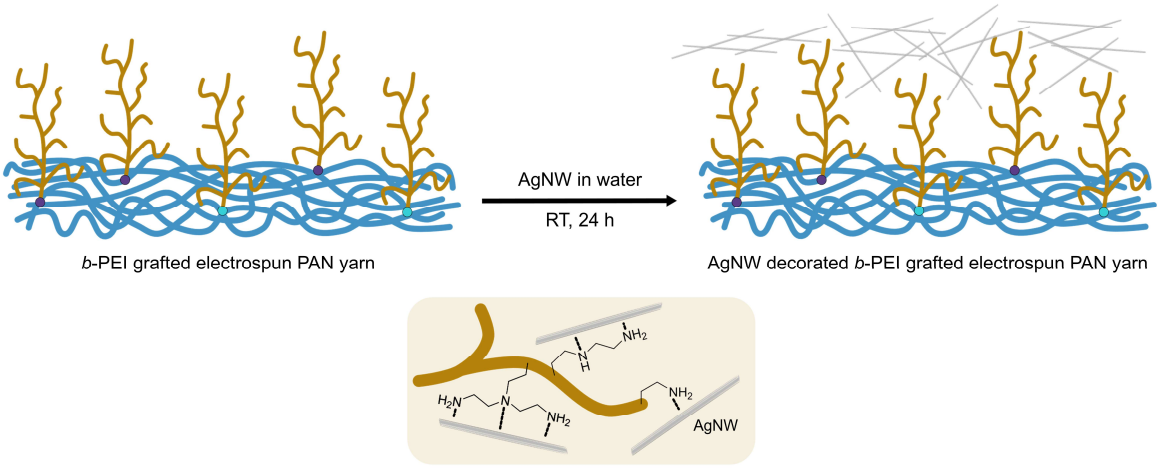

Figure 27: Illustration of 1D PAN yarn functionalization: the adsorption of AgNW onto the electrospun PEI modified yarn from dip-coating in aqueous suspensions.

For this purpose, AgNWs were synthesized *via* the polyol method according to REICH et al., yielding high aspect ratio nanowires with diameters of approximately 200 nm and lengths ranging from 3 to 34 µm.[121] The AgNW suspension, with a concentration of 0.9 wt% ($AgNW_{1D}$ batch), exhibited good stability in water, which is crucial for achieving homogeneous dip-coating of the various yarn samples. The high aspect ratio and 1D geometry of AgNWs are particularly advantageous, as they shall enable the formation of percolating conductive networks at low filler loadings and enhance both electrical and thermal transport properties of the composite material.

SEM analysis, as depicted in Figure 28, reveals the limitations of the applied functionalization approach. After dip-coating, the originally well-aligned nanofibers within the PAN yarns are largely obscured by a randomly distributed layer of AgNWs. These nanowires form a rigid, stand-alone shell around the fiber bundles, which, while potentially beneficial for conductivity, introduces new challenges. The structure makes the yarns particularly susceptible to defects and breakage of the AgNW shell, especially in thinner samples such as the x2 and x3 yarns. This vulnerability for discontinuities in the shell can compromise both the electrical, thermal and structural integrity of the yarn. Furthermore, the coating technique does not provide any control over the orientation of the anisotropic AgNWs, resulting in a lack of alignment on the yarn surface. This absence of directional arrangement is a significant drawback, as it prevents the exploitation of the nanowires' as well as x2 and x3 stretched yarns' intrinsic anisotropic properties. Consequently, no orientation parameter was determined for these samples, as the random distribution of AgNWs precludes meaningful analysis of alignment.

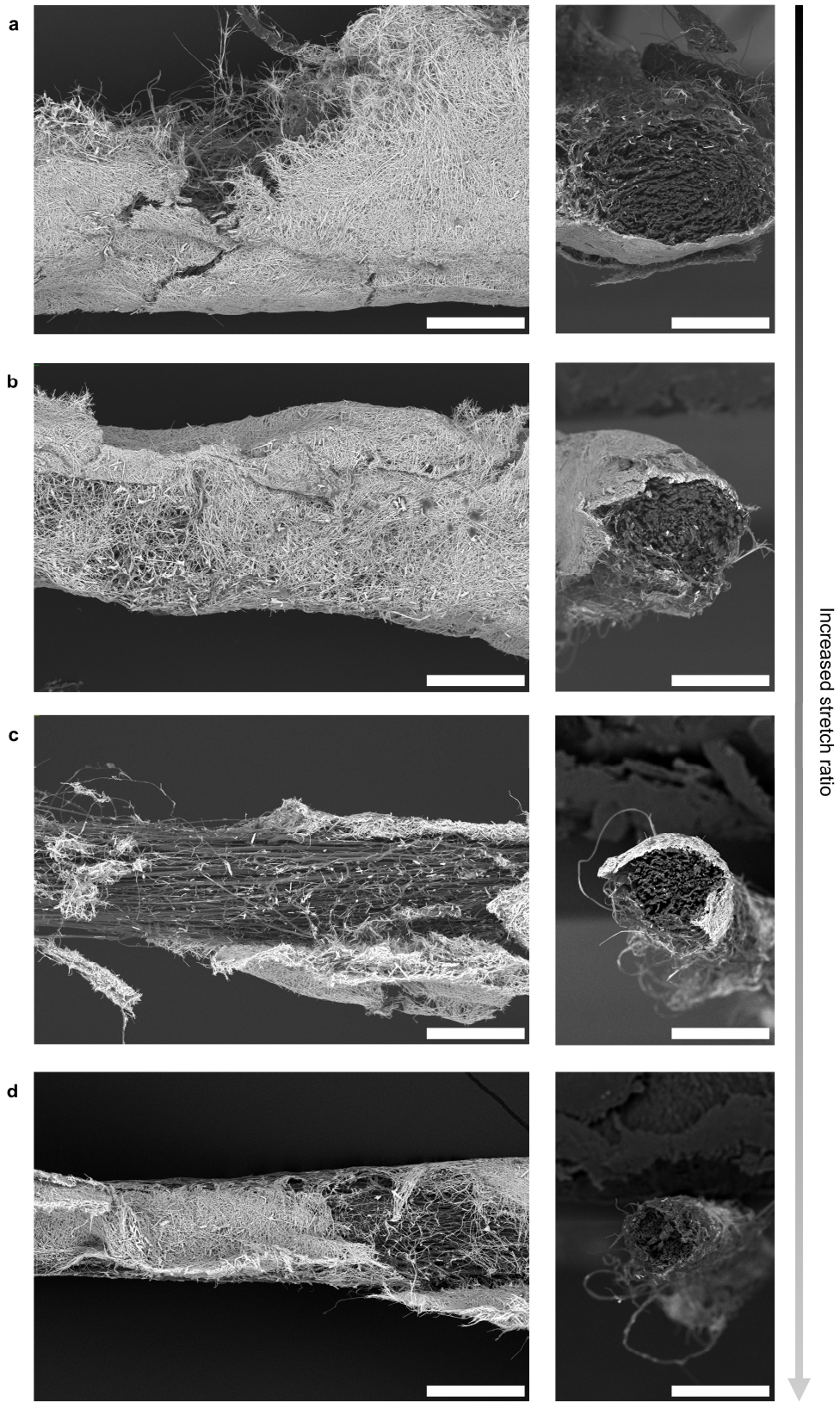

Figure 28: SEM images (top view and cross section) of AgNW functionalized 1D PAN yarns in the as spun (**a**), annealed (**b**) as well as x2 (**c**) and x3 stretching state (50 µm scale bar) (**d**).

To assess the stability of the AgNW coating after dip-coating and drying, a leaching test was performed.

For this analysis, a 2 cm segment of the as spun AgNW functionalized 1D PAN yarn was immersed in 5 mL of deionized water and subjected to strong shaking for 24 h. The resulting leaching solution was analyzed using UV-Vis spectroscopy to detect any potential release of AgNWs from the yarn surface. As a positive control, a diluted $AgNW_{1D}$ suspension (0.5 mL diluted with deionized water to a final dilution of 1:100) was measured in parallel to ensure the method's sensitivity. The UV-Vis spectra, presented in Figure 29, indicates that there is no significant evidence of AgNW leaching from the yarns under these conditions. The absence of characteristic AgNW absorption peaks in the leaching solution, compared to the positive control, demonstrates that the nanowires remain firmly anchored to the PEI modified PAN surface even after prolonged exposure to water and vigorous shaking. This suggests that the dip-coating process, combined with the PEI anchoring layer, provides sufficient adhesion to maintain AgNW stability during aqueous handling.

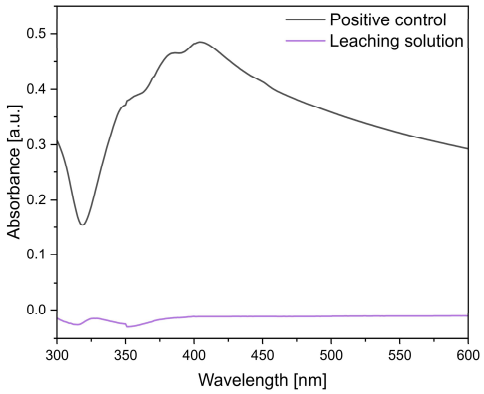

Figure 29: UV-Vis absorbance spectrum of an AgNW positive control solution alongside the solution resulting from the leaching experiment.

The electrical properties of the AgNW functionalized PAN yarns were evaluated using a potentiostat, with the test circuit visually monitored *via* an LED, as illustrated in Figure 30a. For these experiments, both neat and AgNW coated 1D PAN yarns were mounted as electrical element in the circuit (see Figure 30c). Due to their greater robustness and ease of handling, only the as spun yarn representatives could be reliably integrated into the set-up. Yarns with higher stretch ratios proved too thin and fragile for consistent electrical contact.

Upon applying a voltage of 3 V, the AgNW functionalized yarn successfully completed the circuit, causing the LED to illuminate - clear evidence of effective electrical conductivity imparted by the silver nanowire coating. In contrast, the neat PAN yarns did not conduct sufficient current to light the LED, confirming their insulating nature. Quantitative current measurements further support these findings.

While the current passing through the AgNW yarn was lower than that of a direct closed circuit, it is in fact comparable to values reported for AgNW-coated PAN yarns by SHAO et al.[114]

These results demonstrate that the dip-coating process with AgNWs confers significant electrical functionality on the PAN yarns, enabling their use as conductive elements in circuits, even though this is limited to the thicker as spun yarns.

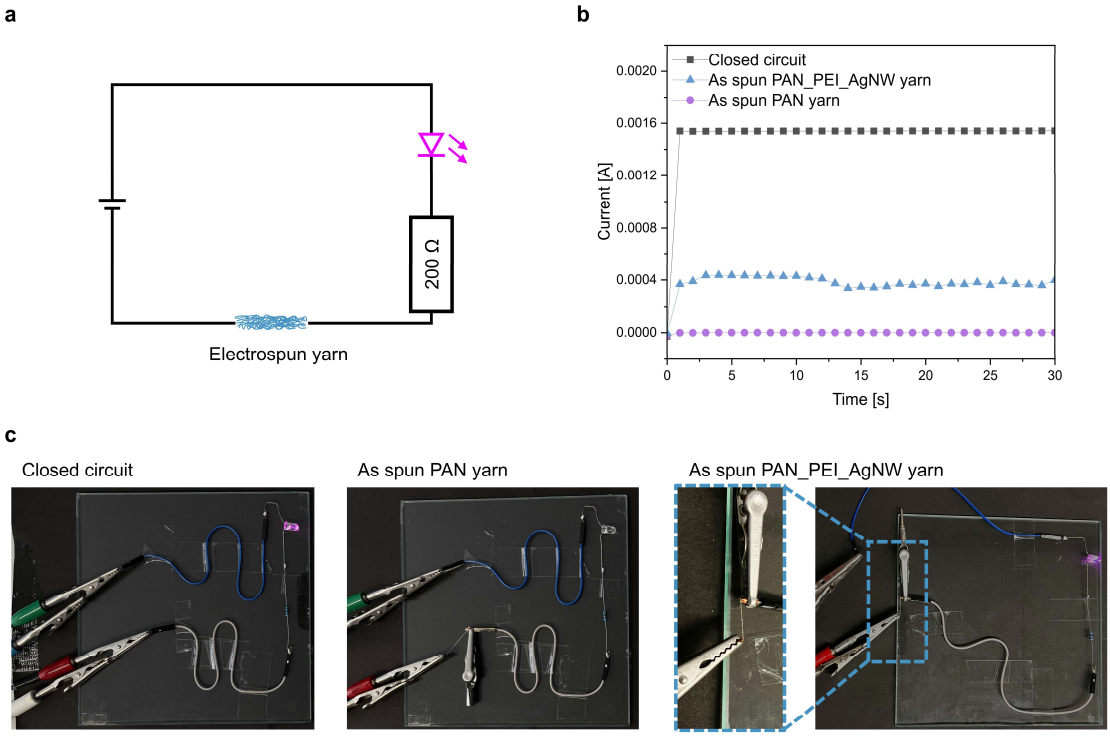

Figure 30: Illustration of the assembled circuit for testing the electrical performance (**a**), current-time plots in case of a closed circuit, incorporated neat or AgNW functionalized 1D PAN yarn (**b**) and optical images of the three cases (**c**).

While the electrical testing confirms that AgNW functionalization introduces conductivity to PAN yarns - albeit limited to thicker, mechanically robust samples - the thermal analysis reveals complementary insights into the coating's structural limitations. Both characterization approaches face shared challenges: the inhomogeneous AgNW distribution and mechanical fragility of the nanowire shell, particularly in thinner yarns, not only complicate electrical but also thermal measurements. The thermal analysis of the four different AgNW functionalized PAN yarn types focused on evaluating their heat transfer properties and the impact of the nanowire coating. Considering the LIT analysis of neat PAN yarns (see Chapter 3.1.1, Figure 21), where both phase and amplitude values could be processed, the current measurements for AgNW coated yarns were limited to phase values due to inhomogeneities in the AgNW shell that complicated the measurements. For comparison, only the phase values for the thermal diffusivity α of neat 1D PAN yarns were considered (summarized in Chapter 7, Table 20).

The results from the LIT analysis, conducted by Ina Klein (Physical Chemistry I, Prof. Dr. Markus Retsch), in Figure 31 reveal distinct differences across the yarn types. For as spun and annealed AgNW functionalized yarns, thermal diffusivity values are uniformly higher than those of their neat counterparts (37 % respectively 32 %), reflecting the partial integration of AgNWs onto the fiber matrix. However, for stretched yarns (x2, x3), thermal diffusivity stagnates at levels comparable to neat PAN yarns. This stagnation persists despite the incorporation of AgNWs, which possess intrinsic thermal conductivities of 190 - 330 $W \cdot (m \cdot K)^{-1}$.[122,123] The lack of improvement in stretched samples can be attributed to pronounced defects in the AgNW shell, such as cracks and discontinuities, which disrupt the formation of a continuous percolation network (see Figure 28). These defects prevent efficient heat transfer along the yarn axis effectively negating the nanowires' high thermal conductivity. Critically, the low absolute thermal diffusivity values observed across all functionalized yarns suggest that heat transfer remains dominated by the PAN matrix rather than the AgNW filler. Even in samples with intact nanowire layers (as spun and annealed), the matrix's inherently low thermal conductivity (~ 0.26 $W \cdot (m \cdot K)^{-1}$ for bulk PAN) governs the overall thermal response, masking potential contributions from the AgNWs.[124] This dominance explains why the stretch ratio-dependent trends in thermal diffusivity for AgNW functionalized yarns closely mirror those of neat PAN yarns: the matrix's alignment and crystallinity, rather than the filler's properties, dictate the thermal behavior. Only when a continuous, defect-free AgNW network forms - a condition unmet here - the filler's thermal conductivity would dominate.

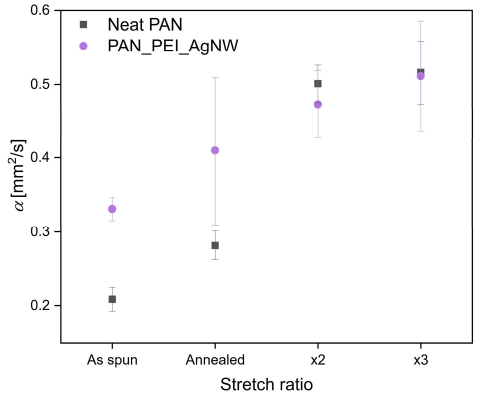

Figure 31: Thermal diffusivity α determined from phase value evaluations resulting from LIT as a function of stretch ratio for neat as well as AgNW functionalized 1D PAN yarns.

The experimental results align with established theory on heat transfer in composite materials, where the thermal performance is strongly influenced by several parameters: the interface between filler and matrix, the orientation and geometry of the filler, and the overall spatial distribution and dispersion of conductive elements.[125]

In the present system, the combination of anisotropic AgNW fillers, confined 1D matrix architecture, and non-specific surface functionalization created a tripartite challenge where these factors mutually impeded directed thermal transport. While anisotropic fillers theoretically enabled preferential heat flow along their longitudinal axis, their random orientation within the rigid PAN shell - amplified by dip-coating's inherent limitations - failed to leverage this directional potential.[125,126] The confined yarn geometry further restricted optimal filler alignment strategies developed for 2D planar systems, while non-targeted functionalization introduced interfacial phonon scattering sites that negated the benefits of any partial alignment.

Recent advances in fiber processing suggest combinatorial approaches could overcome these limitations. TANG et al.'s multistep process (including wet spinning, saturated salt-induced aggregation and plasmonic welding) demonstrates how directed assembly during spinning can achieve both stable dispersion and strong interfacial bonding in all-metal fiber systems.[127] Approaches like these can address the fundamental conflict between filler anisotropy, matrix confinement, and interfacial optimization - three factors that current layer-by-layer assembly methods struggle to reconcile simultaneously.

3.2 2D nonwovens

The transition from 1D yarn architectures to 2D nonwoven structures marks a significant expansion in dimensionality, opening new possibilities for the implementation of morphologies and alignment strategies. The following chapter is based on work previously published in: I. Klein, S. E. Fritze, A. Berger, H. Schmalz, M. Retsch, A. Greiner, *ACS Appl. Polym. Mater.* **2026**, *8*, 1954.[128] In contrast to the confined, 1D systems discussed previously, 2D nonwovens allow for greater flexibility in controlling the spatial arrangement of fibers and fillers,[129] which directly influences their thermal and electrical transport properties.

In this chapter, alignment within the nonwoven structure was achieved using a high-speed rotating collector during fiber processing *via* electrospinning. Among the various electrospinning techniques, Stable Jet Electrospinning (SJES) stands out for its ability to produce nonwovens with an exceptionally high degree of fiber orientation.[130–132] PS was selected as the base material due to its amorphous nature, which avoids complications from crystallinity fluctuations and allows for a clear assessment of the effects of structural changes on transport properties. Three distinct degrees of fiber orientation were prepared: random, oriented, and extremely oriented 2D PS nonwovens (see Figure 32). This systematic variation enables a detailed investigation of how alignment influences the macroscopic properties of 2D fiber materials.

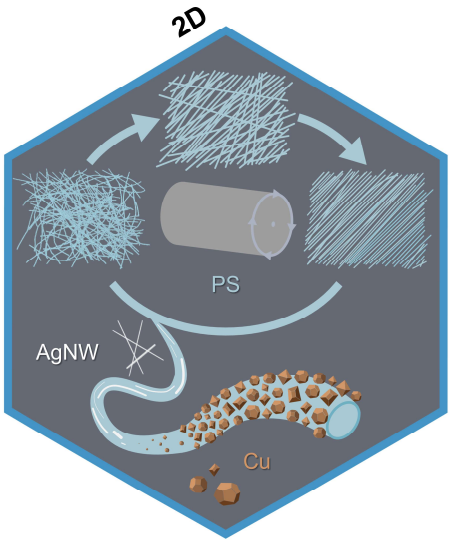

Figure 32: Overview illustrating the second chapter's content, introducing the realization of 2D PS nonwovens with various fiber orientations and either internal (AgNW) or external (Cu) metallization.

Functionalization of the nonwoven structures was carried out using two complementary routes. The first involves the internal incorporation of AgNWs within the PS fibers.[133]

In this approach, AgNWs are dispersed throughout the polymer matrix prior to electrospinning, which enforces their alignment along the fiber axis during processing. This method differs from the previous chapter, where AgNWs were applied to the exterior of yarns. Here, the encapsulation of AgNWs within the fibers - combined with their controlled alignment at a distinct length scale - stands out as a defining characteristic. Moreover, the polymer matrix also effectively prevents nanowire aggregation within the composite structure. The second functionalization route adapts a post-processing approach, creating a copper layer onto the nonwoven substrates *via* wet chemical deposition.[56] In this case, the filler is again located on the exterior of the fibers, but now exhibits an isotropic geometry, in contrast to the anisotropic AgNWs. This dual approach - internal and external functionalization - provides a comprehensive framework for studying the effects of both filler geometry and distribution on thermal and electrical transport in 2D nonwovens.

Building on the initial exploration of AgNW coatings applied to 1D yarns, the second chapter shifts its focus towards the controlled alignment of anisotropic fillers within a 2D nonwoven architecture. It systematically explores the relationship between fiber alignment, filler incorporation, and transport properties in 2D nonwoven architectures.

3.2.1 Nonwoven preparation

To fabricate 2D PS nonwovens with controlled fiber alignment, Conventional Electrospinning was employed using a high-speed rotating drum collector (see Figure 33a). Further analytical data on the spinning material can be found in Chapter 5.1 (see Table 6) and Chapter 7 (see Figure 60c). In this set-up, the grounded drum collector was positioned between a positively charged syringe containing the polymer solution and a negatively charged back electrode, creating an electric field that directed the fiber jet towards the collector surface. By systematically varying the drum rotation speed from 30 to 3000 rpm, nonwovens with random or oriented fiber arrangements were obtained. For ultrahigh alignment, Stable Jet Electrospinning (SJES) was implemented (see Figure 33b), adapting previous methodologies to align with Conventional Electrospinning processing conditions.[131,132] In this modified configuration, the back electrode was removed, and the syringe was positioned directly above the drum. Critical to SJES success were a high-viscosity PS solution (28 wt% in DMF), which suppressed bending instabilities and enabled the formation of a continuous, unsplit jet. High-speed camera images (see Figure 33b) captured the jet's stability over distances exceeding 15 cm, a hallmark of the "low moving velocity" regime described by Xu et al.[132] The combination of this stable jet trajectory and the drum's rapid rotation (3000 rpm) produced nonwovens with near-perfect fiber alignment, hereafter termed SJES nonwovens.

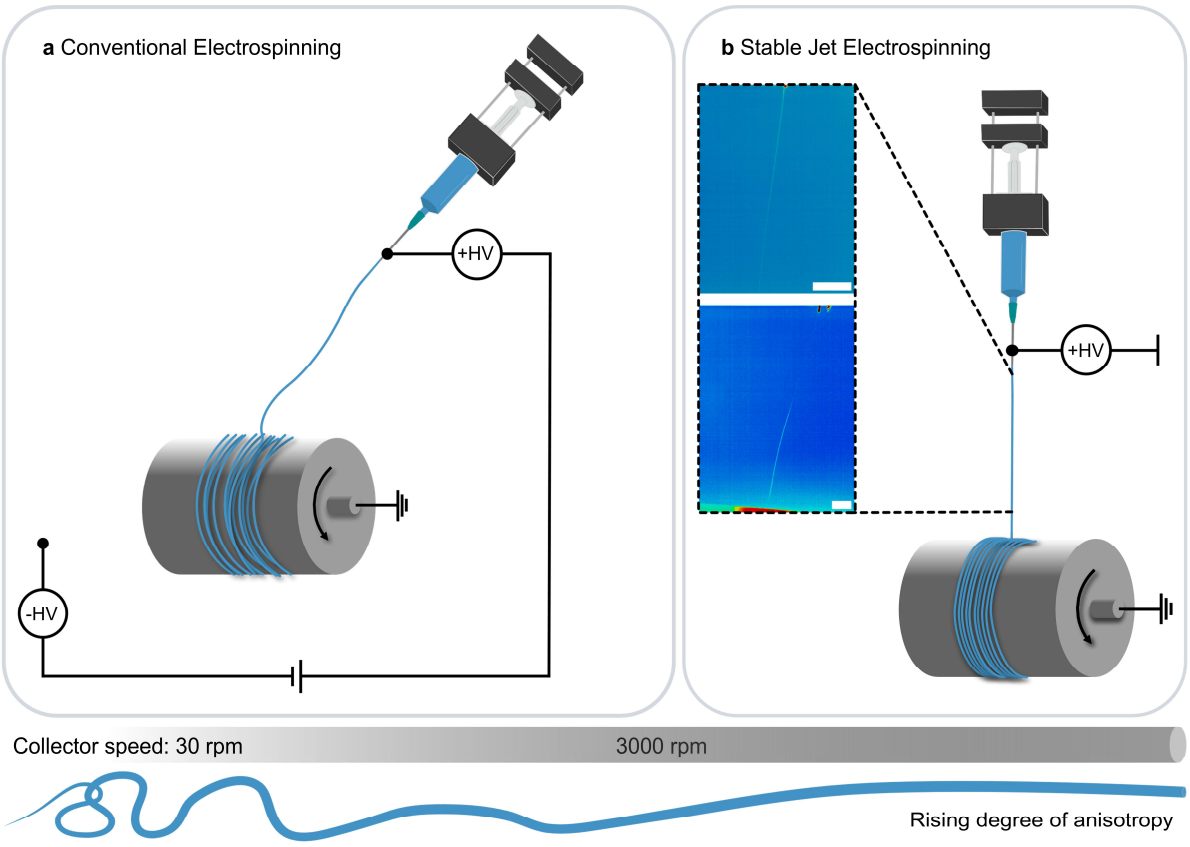

Figure 33: Illustration of the Conventional Electrospinning set-up consisting of the solution filled syringe fixed on the right alongside a back electrode in form of an empty syringe fixed left to the high-speed drum collector (**a**) as well as the Stable Jet Electrospinning set-up equipped with the solution filled syringe fixed above the high-speed drum collector. The produced unsplit fiber jet is visualized in high-speed camera images (1 cm scale bar) (**b**). Reprinted in parts with permission from KLEIN et al.[128] Copyright © 2026, American Chemical Society.

To avoid misinterpretation of fiber orientation in the 2D nonwoven samples, the direction in which the majority of fibers align in oriented or SJES nonwovens is defined as the “preferred orientation”, “preferred direction” or “long axis”. Conversely, the direction perpendicular to this alignment is designated as the “cross-orientation”, “cross-direction” or “short axis”.

Prior to thermal analysis, all nonwoven samples underwent post-processing modification to guarantee sufficient flatness and uniformity for LIT. This involved either compression molding at room temperature under a pressure of 2 t or thermal annealing at 115 °C for 3 or 24 h. The latter was done by Ina Klein (Physical Chemistry I, Prof. Dr. Markus Retsch). These procedures not only improved sample planarity but also induced structural transformations that can affect thermal transport properties. For example, random nonwovens exhibited isotropic shrinkage, while oriented and SJES nonwovens shrank primarily along the preferred direction, reflecting the underlying fiber alignment.

The SEM images in Figure 34 visually document the increasing degree of fiber alignment achieved with each electrospinning method. The progression from random to oriented and finally to SJES nonwovens is clear, with the latter displaying a near-perfect alignment of fibers.

The distinction between oriented and SJES nonwovens is particularly striking, as the SJES method yields more uniform and tightly packed fiber arrangements. In addition, the SEM images highlight the morphological evolution of the fibers after post-processing: compression molded samples feature predominantly straight fibers, whereas thermal annealing transforms the fiber morphology, resulting in increased waviness and, over extended annealing times, the formation of larger fiber bands or bundles with pronounced contact points. The latter is attributed to a shrinkage of fibers induced by thermal treatment.

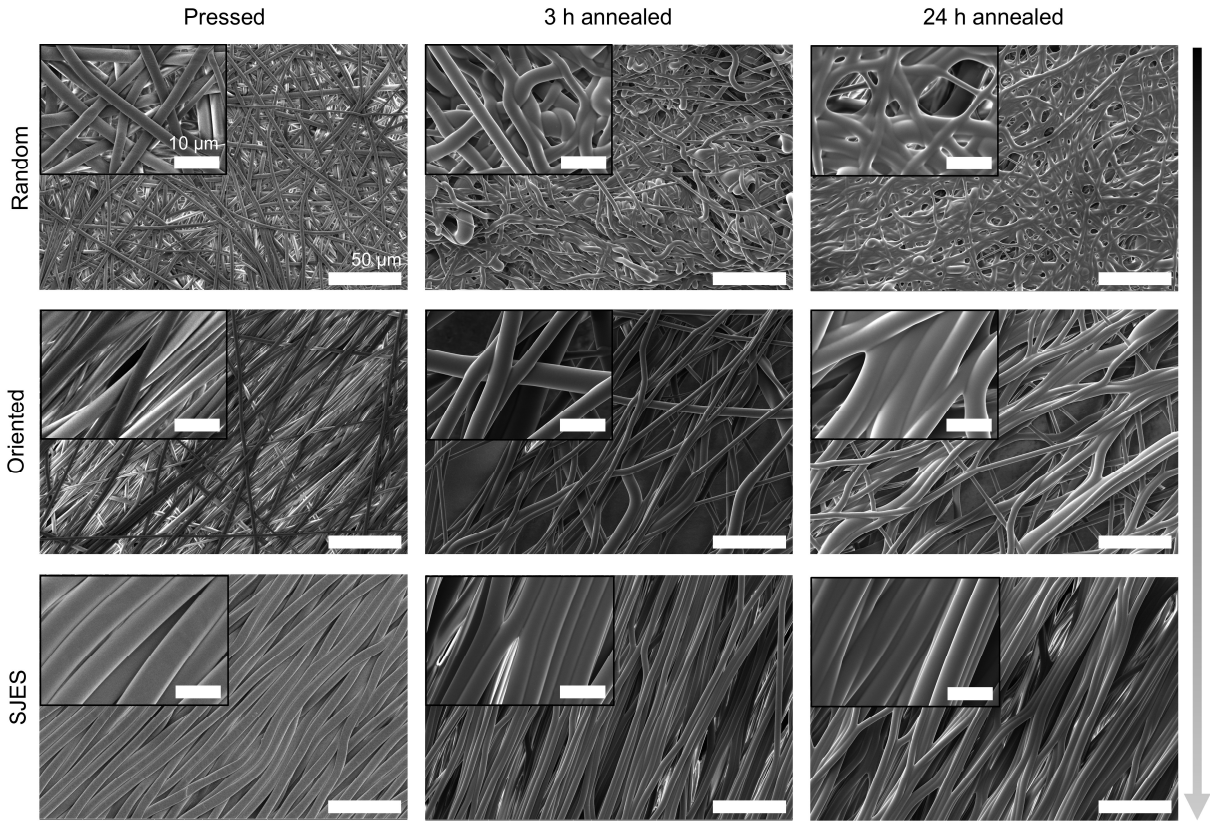

Figure 34: SEM images of 2D PS nonwovens after compression molding at room temperature at 2 t, annealing at 115 °C for 3 or 24 h exhibiting random, oriented or extremely oriented (SJES) fiber alignment (10 respectively 50 µm scale bar). Reprinted in parts with permission from KLEIN et al.[128] Copyright © 2026, American Chemical Society.

SEM images provided the basis for determining the fiber diameters of each nonwoven type (summarized in Chapter 7, Table 21). These data clearly demonstrate that fiber diameters increase with longer annealing times, as illustrated in Figure 35a. Additionally, fibers of nonwovens with higher degrees of orientation - such as the SJES nonwovens - tend to be slightly thicker than those in random or oriented counterparts.

Beyond SEM, Laser Scanning Confocal Microscope (LEXT) imaging enabled the calculation of the orientation parameter S_{2D} performed by Ina Klein (Physical Chemistry I, Prof. Dr. Markus Retsch) (for procedure see Chapter 5.1 - LEXT and Chapter 7, Figure 65). This time, 10 images per nonwoven type were acquired.

That allowed the calculation of mean values and standard deviations (see Chapter 7, Table 21). The S_{2D} parameter again quantifies the degree of fiber alignment, ranging from 0 (completely random) to 1 (perfectly aligned), and the trend in these values closely mirrors the qualitative impressions from the SEM images. The S_{2D} parameter in Figure 35b increases steadily from random to oriented to SJES nonwovens, confirming that the SJES method yields near-perfect alignment of fibers. However, annealing slightly reduces the S_{2D} values for the oriented and SJES nonwovens, as the thermal treatment induces shrinkage along the preferred orientation and the formation of wavy, multi-fiber bands, thereby diminishing the overall alignment.

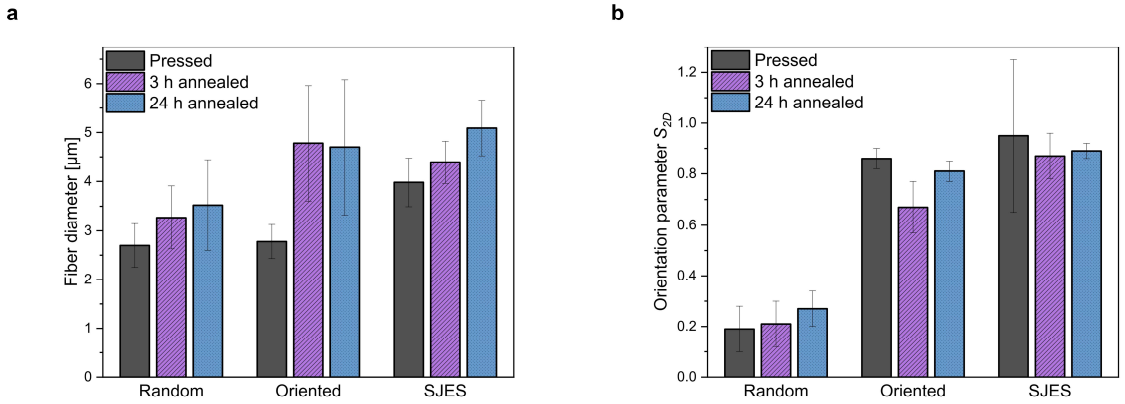

Figure 35: Fiber diameter of pressed and thermally annealed 2D PS nonwovens (**a**) as well as the orientation parameter S_{2D} as a function of fiber alignment (**b**) (adapted from KLEIN et al.).[128]

The combination of SEM imaging and LEXT-based analysis provided quantitative insights into how processing methods influenced fiber architecture, while LIT measurements directly linked these structural features to macroscopic thermal transport properties. Phase and amplitude data from LIT (see Chapter 7, Figure 66 for measurement characteristics), generated and evaluated by Ina Klein (Physical Chemistry I, Prof. Dr. Markus Retsch), demonstrated distinct patterns: randomly oriented nonwovens exhibited circular thermal response profiles, while oriented and SJES samples showed elliptical distributions with distinct short- and long-axis thermal diffusivity values, representing the cross- respectively preferred fiber orientation. A hot-pressed homogeneous PS film served as an isotropic non-fibrous reference.

Random 2D PS nonwovens, prepared using a rotating drum collector (in low speed), exhibit negligible structural orientation. These samples consistently demonstrate intermediate thermal diffusivity values between the preferred and cross-direction measurements of oriented counterparts across all post-processing conditions (see Figure 36). This behavior stems from their uniform distribution of inter-fiber contact points and gaps, as visualized in SEM images in Figure 34. Oriented nonwovens display contrasting thermal behavior depending on measurement direction.

Most gaps and contact points align perpendicular to the preferred orientation, increasing thermal resistance in the cross-direction while enhancing axial transport along aligned fibers. The SJES samples surpass oriented nonwovens in preferred direction thermal diffusivity, consistent with their superior fiber alignment quantified through S_{2D} values (see Figure 35b) Surprisingly, SJES nonwovens also show elevated cross-direction diffusivity compared to oriented samples. This counterintuitive result is attributed to the near-perfect fiber alignment in SJES specimens, which maximizes longitudinal contact areas between adjacent fibers. In contrast, moderate misalignment in oriented samples disrupts these contacts, impeding cross-directional heat transfer. Thermal anisotropy ratios (preferred/cross-direction diffusivity) highlight these structural effects: SJES samples show moderate anisotropy of 2.8, while oriented specimens exhibit significantly higher ratios of 8.6 due to severely restricted cross-direction transport.

Annealing induced substantial changes, particularly in random nonwovens where thermal diffusivity increases by > 50 % after 3 h and > 70 % after 24 h. Figure 34 illustrates how fiber fusion at contact points, combined with membrane shrinkage, reduces interfacial thermal resistance. Extended annealing times produce more extensive fusion, further enhancing the transport. For oriented and SJES samples, annealing increases preferred direction diffusivity to α values approaching those of hot-pressed PS films (indicated by the yellow line in Figure 36). Annealed SJES samples are even exceeding this α value. This behavior cannot only be attributed to improved alignment. This is why polarized RAMAN spectroscopy was performed by Dr. Holger Schmalz (Macromolecular Chemistry II) to detect possible changes at the molecular level, but no significant differences in polymer chain orientation were observed (see Chapter 7, Figure 67). The increased fiber waviness noted after annealing suggests a PS polymer chain relaxation - a structural modification that typically reduces thermal transport. The enhancements observed instead correlate with improved inter-fiber contact quality.

Cross-direction diffusivity in oriented samples increase significantly post-annealing, reducing the thermal anisotropy ratio from 8.6 to 2.8 (3 h) and 2.2 (24 h). Shrinkage contributes minimally to an increasing total cross-fiber contact area due to directional specificity for the preferred direction. In fact, SEM images (see Figure 34) confirm that fiber fusion dominates this enhancement by lowering contact resistance. SJES specimens display opposite behavior, with 3 h annealing reducing cross-direction diffusivity through gap formation between previously tightly packed fibers for the pressed counterpart. After 24 h annealing, extensive fusion compensated for these gaps, restoring diffusivity near initial values (from pressed nonwovens) despite persistent structural changes.

In combination with an enhanced thermal diffusivity in the preferred direction, this leads to higher thermal anisotropy (5.1) compared to the pressed SJES nonwoven (2.8).

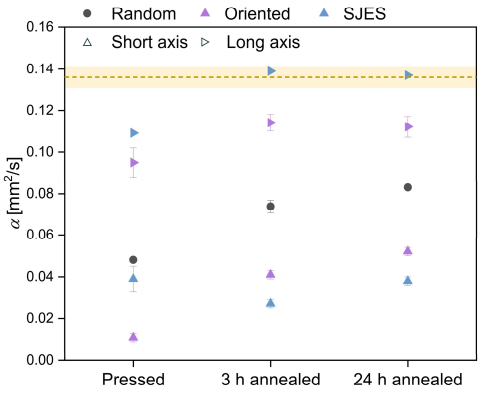

Figure 36: Thermal diffusivity α of neat 2D PS nonwovens determined from amplitude-phase product evaluations resulting from LIT as a function of post-processing treatment. The yellow line represents the thermal diffusivity of a hot-pressed PS film (adapted from KLEIN et al.).[128]

These findings demonstrate that optimal thermal anisotropy requires balancing alignment quality with controlled inter-fiber contact. Near-perfect alignment (SJES) promotes cross-direction transport through extensive fiber contacts, while moderate alignment (oriented) enables high anisotropy by limiting such pathways. Even minor gaps between fibers substantially hinder heat transfer, emphasizing that structural control outweighs perfect alignment for tailoring thermal properties.

3.2.2 Nonwoven functionalization

The next step involves functionalizing 2D PS nonwovens using two distinct strategies. First, a pre-processing functionalization was achieved by embedding AgNWs within the nonwovens, adapting an approach from CHEN et al. to match previous processing conditions.[133]

AgNW synthesis, conducted similarly to Chapter 3.1.3, yielded a new aqueous suspension, designated as the $AgNW_{2D}$ batch, with a concentration of 2.2 wt%. The nanowires in this suspension possess a diameter of approximately 100 nm and lengths that range from 5 to 23 µm. Figure 37 illustrates the preparation process, which commenced with the freeze drying of the AgNW suspension. The dried nanowires were then redispersed in DMF before PS was added to create the spinning solution. This solution was processed using Conventional Electrospinning (see Chapter 3.2.1, Figure 33a) to realize composite nonwovens characterized by both random and oriented fiber alignments. Before proceeding with further analyses, the composite nonwovens underwent a post-processing modification consisting of compression molding, similar to the procedure used for the neat 2D PS nonwovens in Chapter 3.2.1, but did not include thermal annealing.

As a macroscopic observation documented in Chapter 7, Figure 68 a, the functionalized composite nonwovens exhibit a slight yellow-brown color, in contrast to their white, unfunctionalized 2D PS counterparts.

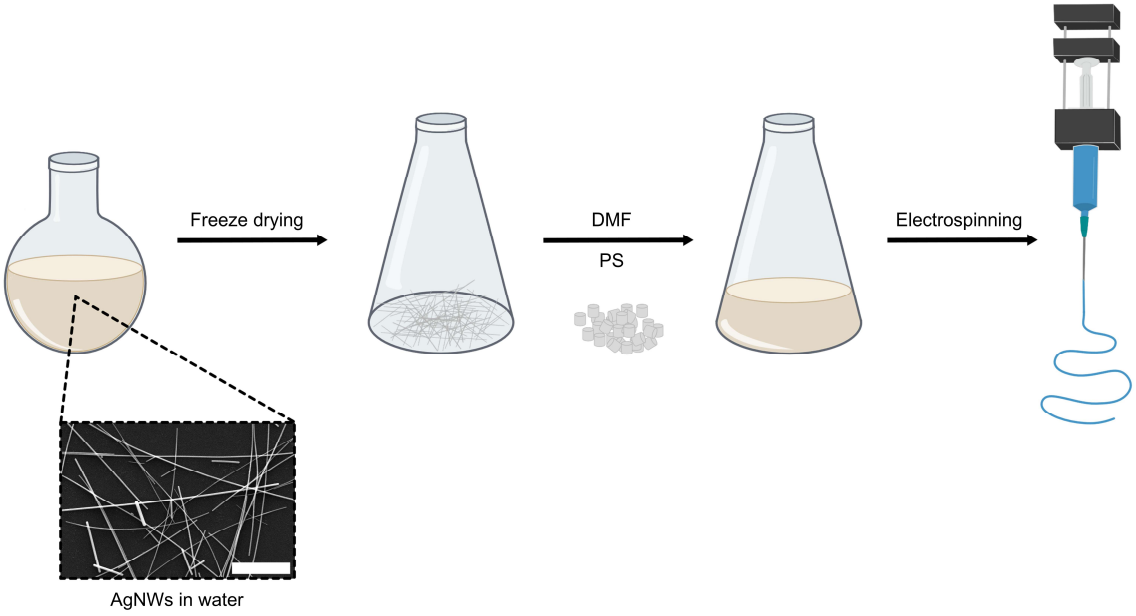

Figure 37: Illustration of internal 2D PS nonwoven functionalization: starting with the freeze drying of an aqueous AgNW suspension (further visualized in a SEM image, 3 µm scale bar). This is followed by the additon of DMF and PS to form the final composite electrospinning solution. Reprinted with permission from KLEIN et al.[128] Copyright © 2026, American Chemical Society.

The SEM analysis provides critical insights into the structural integration and distribution of AgNWs within the PS nonwovens. By employing both secondary electron (SE) and backscattered electron (BSE) detectors, the investigation differentiates between surface topography and compositional contrast. As illustrated in Figure 38, the BSE-detector, sensitive to atomic number variations, confirms the embedding of AgNWs within the PS fiber matrix rather than surface deposition. This observation aligns with the absence of nanowire traces in SE-detector images, which primarily capture topographical features of the fiber shell. Additionally, the electrospinning process facilitates the alignment of AgNWs along the fiber axis, as evidenced by the directional orientation of nanowires in SEM images captured with the BSE-detector. This outcome contrasts with earlier attempts described in Chapter 3.1.3, where AgNWs in stretched 1D PAN yarns exhibited random agglomeration and lacked preferential alignment. Despite the successful integration and orientation, quantitative analysis *via* ICP-OES reveals a critical limitation, detecting an AgNW content of 2.6 wt% (equivalent to approximately 0.27 vol%), matching the maximum value reported in the literature and indicating that higher amounts cannot be incorporated.[134] In combination with the sparse nanowire distribution observed in the SEM images in Figure 38, it can be assumed that the inter-nanowire distances exceed the critical range for building up a percolation network.

Unfortunately, an increase in nanowire concentration is constrained by viscosity limitations, ultimately preventing the achievement of conductive pathways at this loading level.[133]

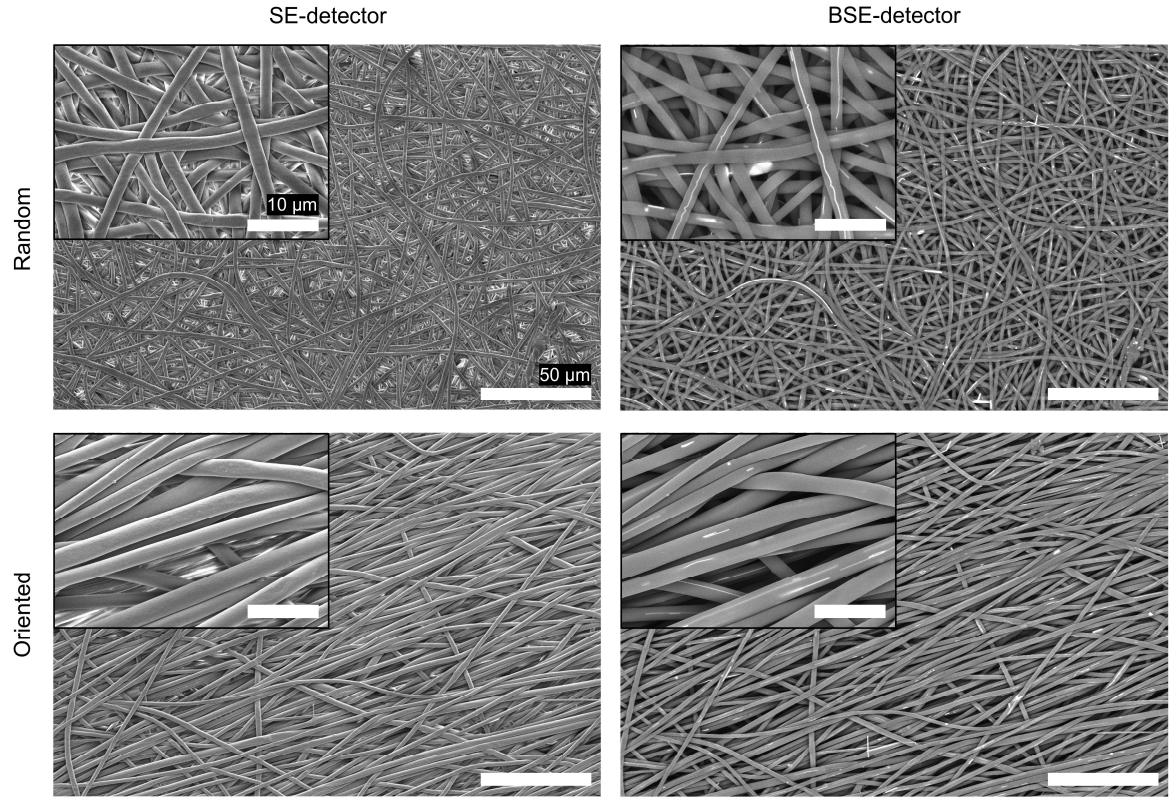

Figure 38: SEM images of pressed AgNW functionalized 2D PS nonwovens exhibiting random or oriented fiber alignment revealing the incorporated AgNWs using a SE- as well as BSE-detector (10 µm respectively 50 µm scale bar). Reprinted with permission from KLEIN et al.[128] Copyright © 2026, American Chemical Society.

When evaluating the structural properties of the AgNW functionalized 2D PS nonwovens, both SEM and LEXT images provided the foundation for determining fiber diameters and the orientation parameter S_{2D}. Detailed results for each nonwoven type are compiled in Chapter 7, Table 21. The calculation of these parameters followed the methodology established in Chapter 3.2.1 and was done by Ina Klein (Physical Chemistry I, Prof. Dr. Markus Retsch). A direct comparison, as presented in Figure 39a, indicates that the introduction of AgNWs leads to a reduction in fiber diameter for both randomly oriented and aligned nonwovens. This decrease, although notable, remains within the typical micrometer range observed for neat PS fibers. The shift towards thinner fibers is likely linked to a reduction in solution viscosity, which occurred despite the polymer and solvent ratio remaining unchanged compared to the neat PS spinning solution.

Turning to fiber orientation, the random nonwovens retain their isotropic arrangement both before and after functionalization. In contrast, the orientation parameter S_{2D} for the oriented AgNW functionalized 2D PS nonwovens decreases relative to the neat sample (see Figure 39b).

This trend is attributed once more to the lower solution viscosity, which compromises the stability and control of the electrospinning jet and reduces the effectiveness of fiber alignment on the high-speed rotating drum. Nevertheless, the difference in alignment between random and oriented samples remains pronounced. The SEM images in Figure 38 visually reinforce these findings, highlighting that, while subtle differences exist, the overall structural integrity and fiber organization of the AgNW functionalized nonwovens remain closely related to those of the neat 2D PS nonwovens.

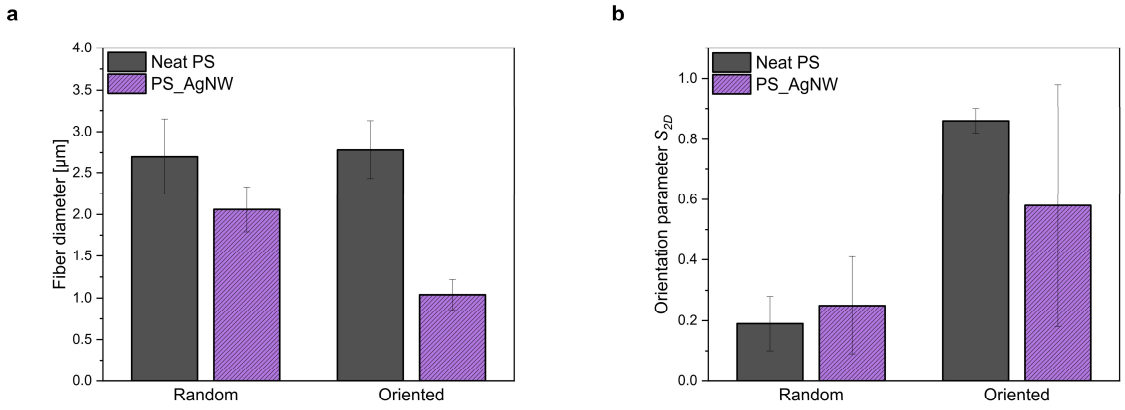

Figure 39: Fiber diameter of pressed neat and AgNW functionalized 2D PS nonwovens (**a**) as well as the orientation parameter S_{2D} as a function of fiber alignment (**b**) (adapted from KLEIN et al.).[128]

Finally, thermal analysis *via* LIT was conducted by Ina Klein (Physical Chemistry I, Prof. Dr. Markus Retsch) to evaluate the changes in thermal diffusivity caused by the presence and orientation of highly conductive AgNWs. Figure 40 compares the α values of pressed neat and AgNW functionalized samples, revealing a consistent trend with anisotropic splitting for oriented nonwovens in long and short axis. The random nonwovens exhibited intermediate α values between the preferred and cross-directions of their oriented counterparts, mirroring observations from Chapter 3.2.1.

Incorporating 0.27 vol% AgNWs lead to an increase in thermal diffusivity of random nonwovens from 0.048 mm^2/s to 0.090 mm^2/s. Despite the high intrinsic thermal conductivity of AgNWs (190 - 330 $W \cdot (m \cdot K)^{-1}$),[122,123] this enhancement remains modest. The limited improvement underscores the dominance of interfacial thermal resistance at PS fiber boundaries, which restricts heat transfer even when AgNWs align with the fiber axis. For oriented nonwovens, AgNW functionalization elevates α in the preferred direction by 1.6-fold (from 0.095 to 0.152 mm^2/s) and in the cross-direction by 3.8-fold (from 0.011 to 0.042 mm^2/s). This disparity arises from the reduced orientation parameter of AgNW functionalized samples (0.58) compared to neat, oriented counterpart (0.86), as quantified in Chapter 7, Table 21).

The lower alignment increased the proportion of misaligned fibers, facilitating cross-directional heat transfer while slightly diminishing axial transport efficiency.

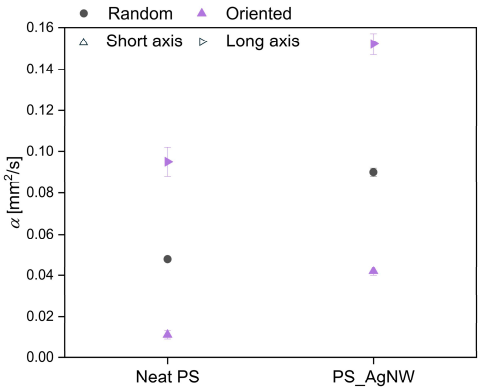

Figure 40: Thermal diffusivity α of pressed neat and AgNW functionalized 2D PS nonwovens determined from amplitude-phase product evaluations resulting from LIT as a function of fiber functionality (adapted from KLEIN et al.).[128]

The pre-processing functionalization of 2D PS nonwovens with AgNWs involved integrating the conductive nanofiller inside the polymer fiber matrix through electrospinning. Despite the successful alignment of AgNWs along the fiber axis, the resulting composite failed to establish a continuous conductive network. Thermal transport measurements demonstrated that the polymer matrix remains the primary determinant of thermal properties, even with the inclusion of AgNWs. While the nanowires enhanced thermal diffusivity in both random and oriented 2D nonwovens, the improvements remained modest relative to the intrinsic conductivity of silver. This limitation stems from interfacial phonon scattering at fiber boundaries, which dominates heat transfer resistance and diminishes the impact of conductive fillers.[135] The findings underscore that structural imperfections at fiber interfaces, rather than filler alignment alone, govern thermal performance. Minimizing interfacial scattering through optimized contact quality and reduced defects emerges as a critical requirement for maximizing the potential of conductive additives in hierarchical composites.

The second functionalization strategy therefore employed a post-processing approach to deposit a layer of isotropic copper particles on the 2D PS nonwoven fiber surfaces, adapting the methodology established by LANGNER et al. Silver deposition was avoided due to excessive dendrite formation during the final reduction step, as previously documented.[56] Preparation steps (see Figure 41) began with mounting pre-processed pressed random and oriented 2D PS nonwovens in rectangular frames (3 x 4 cm) to ensure structural integrity during the wet chemical modification. The nonwovens underwent sequential treatments: first, a poly(4-vinylpyridine) (P4VP) coating was applied to create anchoring sites for subsequent nanoparticle seeding.

Immersion in a silver nanoparticle (AgNP) suspension followed, where the P4VP facilitated uniform AgNP adhesion across the fiber surfaces. These AgNPs then served as catalytic seeds for the electroless copper deposition in the final step.[56]

To ensure consistency, all framed nonwovens were treated simultaneously in a custom-made Teflon reaction container designed to prevent contact between frames while allowing full solution access (see Chapter 7, Figure 68b). Upon this, the PS nonwovens acquired a distinct coppery metallic finish (see Chapter 7, Figure 68 a).

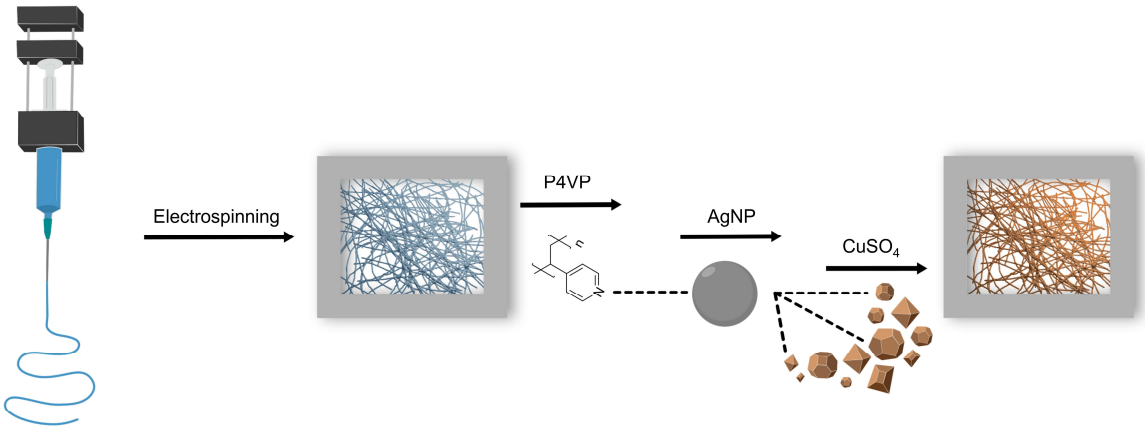

Figure 41: Illustration of external 2D PS nonwoven functionalization: starting with the processing of random and oriented neat PS nonwovens before their fixation in rectangular frames (3 x 4 cm). This is followed by the dip-coating in a P4VP solution that allows the attachment of AgNPs in the next step. The procedure is concluded *via* electroless deposition of copper. Reprinted with permission from KLEIN et al.[128] Copyright © 2026, American Chemical Society.

SEM analysis, as depicted in Figure 42, was carried out using both top view and cross-sectional perspectives to investigate the external copper coating applied to the functionalized PS nonwovens. The BSE-detector played again a crucial role in distinguishing between the PS fiber matrix and the metallic copper coating, highlighting the compositional contrast between the two materials. The images demonstrate that a uniform layer of copper particles conformally coats each individual fiber, resulting in a consistent, homogenous coating across the nonwoven structure. This metallization strategy enables direct contact points between adjacent fibers, facilitating the formation of a percolative network - an essential feature for efficient electron and heat transport that could unfortunately not be realized within the AgNW functionalized PS nonwovens.

Despite the presence of the ~ 100 nm thick copper shell, the underlying fiber alignment - whether random or oriented - remains, preserving the structural anisotropy introduced during electrospinning.

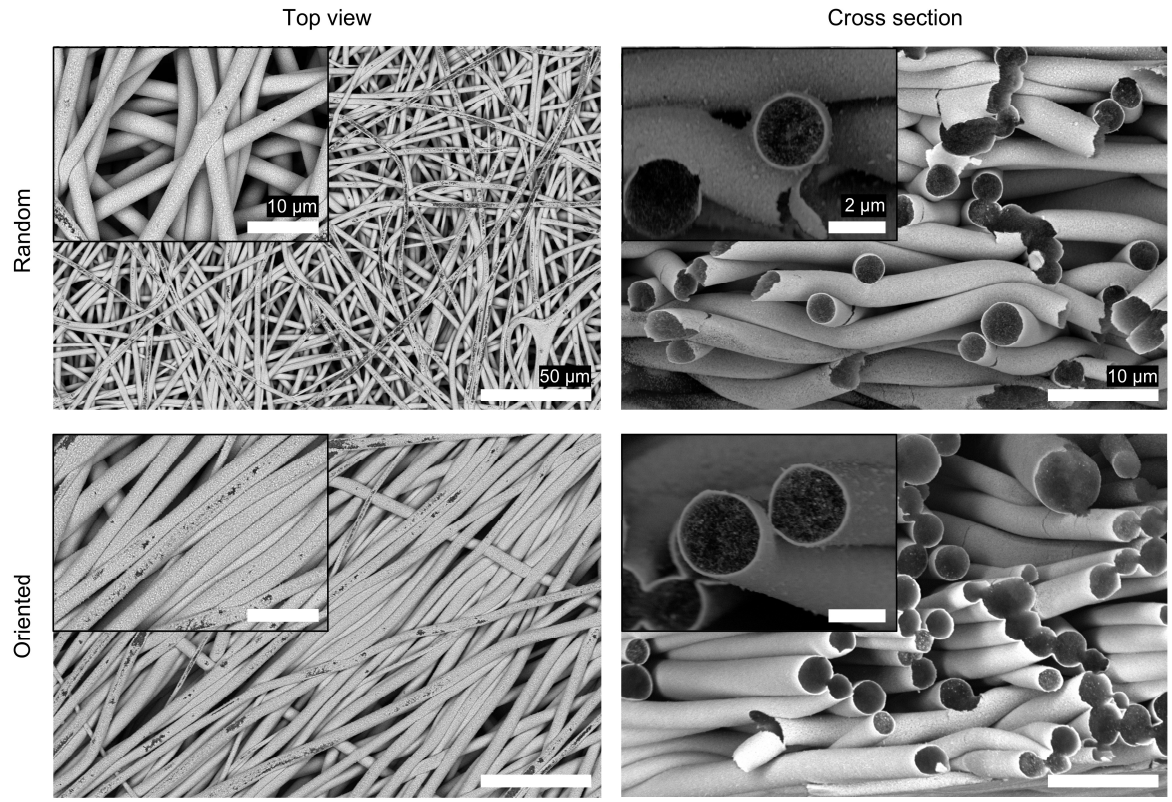

Figure 42: SEM images of pressed Cu functionalized 2D PS nonwovens exhibiting random or oriented fiber alignment revealing the copper plating using a top view (10 µm respectively 50 µm scale bar) and cross section perspective (2 µm respectively 10 µm scale bar). Reprinted with permission from KLEIN et al.[128] Copyright © 2026, American Chemical Society.

The structural properties of neat and functionalized 2D PS nonwovens were systematically compared using SEM and LEXT imaging, with fiber diameters and orientation parameters S_{2D} quantified by Ina Klein (Physical Chemistry I, Prof. Dr. Markus Retsch) as already outlined in Chapter 3.2.1. Exact values for each nonwoven type are again summarized in Chapter 7, Table 21. Figure 43a demonstrates that the introduction of a copper coating *via* post-processing metallization leaves fiber diameters largely unchanged, maintaining values comparable to those of the neat nonwovens. This consistency arises from the ultrathin nature of the Cu layer, which minimally impacts the underlying fiber morphology.

While fiber diameters remain stable, the orientation parameter S_{2D} decreases slightly for both random and oriented nonwovens after metallization. This reduction, evident in Figure 43b, is attributed to the wet chemical deposition process, which introduces localized mechanical stress during immersion and drying. These stresses perturb the initial fiber alignment in pressed nonwovens, particularly affecting the oriented samples. However, the integrity of the fiber network is preserved despite the metallization-induced disturbances, ensuring that macroscopic anisotropic properties remain functionally relevant.

These findings align with earlier observations for AgNW functionalized 2D PS nonwovens, where solution viscosity changes similarly impacted alignment without erasing structural distinctions.

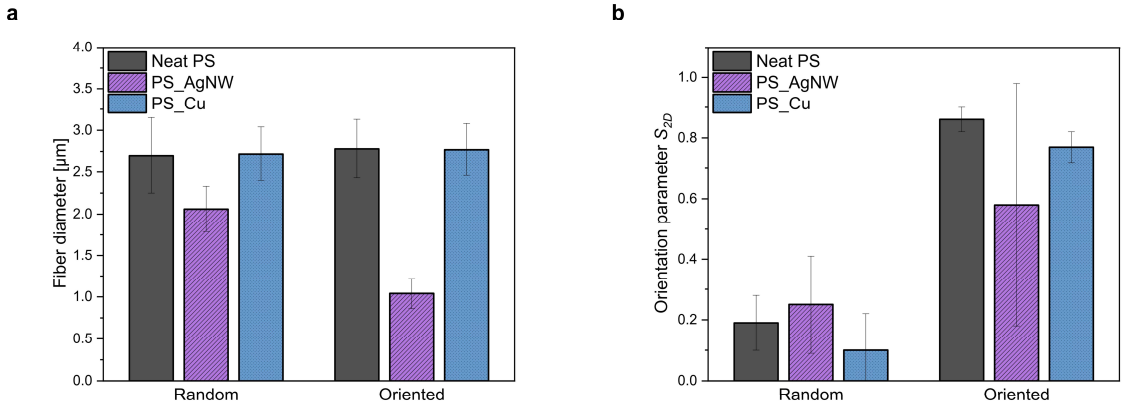

Figure 43: Fiber diameter of pressed neat, AgNW and Cu functionalized 2D PS nonwovens (**a**) as well as the orientation parameter S_{2D} as a function of fiber alignment (**b**) (adapted from KLEIN et al.).[128]

The SEM images in Figure 42 distinctly illustrate the formation of a continuous percolative network by the copper coating, in contrast to the previously discussed AgNW functionalized nonwovens, where such a percolating network could not be established. This enabled the first electrical conductivity measurements of the functionalized 2D nonwovens using a Four-Point Probe set-up. The measurements were conducted by Alexander Berger and Ina Klein (Physical Chemistry I, Prof. Dr. Markus Retsch), assuming square geometry with appropriate correction factors applied to compensate for the relatively small sample dimensions (for procedure see Chapter 5.1 - 4PP). Electrical characterization yields a sheet conductance of 26.2 ± 2.6 S sq^{-1} for the random nonwoven, substantially exceeding the values obtained for the oriented counterpart. The latter demonstrates a slight directional dependence, with the preferred direction exhibiting a marginally higher sheet conductance of 8.3 ± 0.3 S sq^{-1} compared to 7.4 ± 0.1 S sq^{-1} in the cross-direction.

This is when LEXT cross section imaging, conducted by Ina Klein (Physical Chemistry I, Prof. Dr. Markus Retsch), became important, since it exposed critical structural variations between the two nonwoven types (see Figure 44). While the random sample featured homogeneous copper distribution throughout its entire volume, ensuring that all fibers contributed to electrical transport, the oriented nonwoven displayed a markedly different pattern. Here, the deposition occurred predominantly at the surfaces, leaving approximately one-third of the interior volume uncoated.

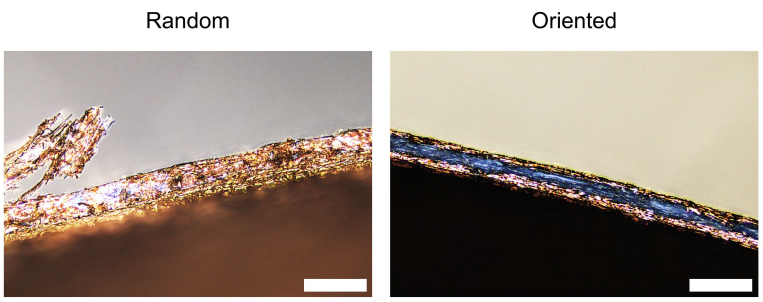

Figure 44: LEXT images of pressed Cu functionalized 2D PS nonwovens exhibiting random or oriented fiber alignment revealing the partial discontinuity of the cooper plating using a cross-section perspective (200 µm scale bar). Reprinted with permission from KLEIN et al.[128] Copyright © 2026, American Chemical Society.

This observation necessitated an adjustment in the conductivity calculations. For the random sample, the full thickness was incorporated into the calculation, whereas only one-third of the measured thickness was considered for the oriented sample. With this correction applied, the resulting conductivity values converge remarkably: 2405 S/cm for the random sample, 2168 S/cm in the cross-direction, and 2436 S/cm in the preferred direction of the oriented nonwoven. Particularly noteworthy is the unexpectedly low degree of electrical anisotropy exhibited by the oriented Cu coated nonwoven. The fiber bundles and their copper coating appear to facilitate electrical conductivity in the cross-direction that nearly matches that of the preferred direction. The sparse elongated cavities present in the structure only minimally impede effective electrical transport across the inter-fiber contacts. This phenomenon parallels observations made with the neat SJES 2D PS nonwoven described in Chapter 3.2.1, where the cross-orientation thermal diffusivity was unexpectedly high due to extensive inter-fiber contact areas, as evidenced in Figure 36.

Finally, LIT was conducted by Ina Klein (Physical Chemistry I, Prof. Dr. Markus Retsch) to evaluate the impact of copper functionalization on heat transport in 2D PS nonwovens, though measurement reliability faced challenges. The high reflectivity of the copper coating introduced significant noise in the signals, even after applying a carbon layer to enhance emissivity. While absolute thermal diffusivity values require cautious interpretation (see Figure 45), directional comparisons provide critical insights into the interplay between nonwoven architecture and heat conduction. The Cu coated nonwovens exhibit markedly higher thermal diffusivity compared to both neat PS and AgNW functionalized counterparts, attributable to the continuous metallic network facilitating efficient heat propagation. Unlike the isolated AgNWs embedded within fibers, the percolating copper shells enable bulk-like thermal transport. For random nonwovens, thermal diffusivity values fall between the preferred and cross-directional measurements of oriented samples, mirroring trends observed in unfunctionalized PS materials.

This suggests that the global fiber architecture, rather than localized copper distribution, predominantly governs heat transfer. Notably, the oriented Cu functionalized nonwovens display a thermal anisotropy ratio of ~ 2.8, significantly lower than the ratio observed in neat oriented PS samples (~ 8.2). This reduction coincides with a decrease in the orientation parameter S_{2D} from 0.86 to 0.77 (see Chapter 7, Table 21), resulting from fiber alignment disruptions during wet chemical deposition. In contrast, electrical anisotropy remains nearly isotropic (1.1), highlighting divergent transport mechanisms: thermal conduction relies on structural continuity across the entire network, while electrical conductance benefits from localized percolation paths even in misaligned regions. The disparity emphasizes that hierarchical composites can exhibit direction-dependent transport properties tailored to specific applications. For instance, the copper coating's ability to maintain structural anisotropy for heat dissipation while enabling omnidirectional electrical pathways aligns with requirements for flexible electronics enabling thermal management. Nonetheless, this observation and its underlying mechanisms warrant further research.

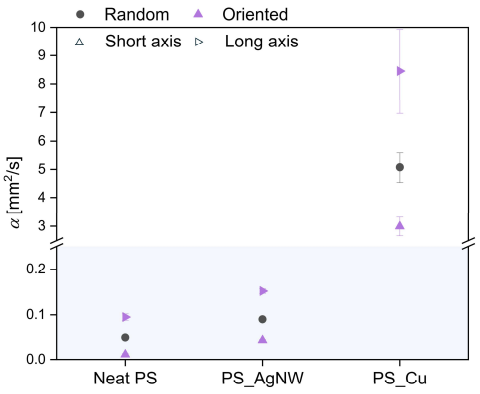

Figure 45: Thermal diffusivity α of pressed neat, AgNW and Cu functionalized 2D PS nonwovens determined from amplitude-phase product evaluations resulting from LIT as a function of fiber functionality (adapted from KLEIN et al.).[128]

The systematic investigation of 2D PS nonwovens with controlled fiber orientations (random, oriented, SJES) and dual functionalization strategies (AgNW incorporation vs. external Cu coating) established a robust foundation for understanding thermal transport mechanisms in hierarchical fibrous systems. While fiber alignment enhanced directional thermal transport, optimal performance emerged from balancing structural architecture with interfacial contact quality rather than pursuing perfect anisotropy. The AgNW functionalized nonwovens demonstrated limited thermal improvements due to non-percolating networks and interfacial phonon scattering, whereas Cu-coated architectures achieved significant conductivity gains through continuous metallic pathways.

These insights complement previous observations from 1D PAN yarns functionalized with randomly distributed AgNW coatings (see Chapter 3.1), reinforcing the principle that structural architecture dominates transport behavior in these functional fibrous assemblies regardless of dimensionality and nanofiller functionality. Particularly noteworthy is the observation that perfect anisotropy does not necessarily translate to optimal directed transport performance. The copper-coated nonwovens exemplified this concept, where electrical anisotropy remained nearly isotropic despite pronounced thermal anisotropy in the same material system. This phenomenon demonstrates the complex interplay between structural hierarchy and transport mechanisms, suggesting that the 2D PS fiber architecture concept could be expanded to encompass 1D yarn configurations for future comparative studies.

Alternative approaches for controlling fiber alignment extend beyond conventional rotating drum collectors to include macroscopically structured templates. A preliminary study employed a metal grid collector (with 1.2 mm mesh spacing) for electrospinning PCL, successfully reproducing the grid template geometry in the resulting fiber architecture (see Chapter 7, Figure 69). Further analytical data on the spinning material can be found in Chapter 5.1 (see Table 6) and Chapter 7 (see Figure 60d). The pressed grid nonwoven underwent subsequent thermal analysis *via* LIT performed by Ina Klein (Physical Chemistry I, Prof. Dr. Markus Retsch), capturing the grid structure through the IR camera at discrete measurement locations (see Chapter 7, Figure 69a and b). However, this structural complexity introduced significant analytical challenges that reveal broader limitations in current characterization methodologies. While the grid pattern remained clearly visible in both phase and amplitude images, these data could not be processed further to extract quantitative thermal diffusivity values. This illustrates that increasing structural complexity demands parallel advancements in characterization methodologies. The importance of such progress is particularly evident when evaluating advanced fibrous structures generated by transformative approaches like Near-Field Electrospinning (NFES). Utilizing high-precision programmable stages, this innovative technique enables defined fiber deposition in distinct, predetermined patterns. Unlike Conventional Electrospinning's chaotic fiber placement, NFES operates through controlled electric fields at reduced working distances. NFES represents the next significant advancement in realizing complex structures for smart textile applications.[19] When combined with the functionalization strategies adapted in this work, NFES could enable spatially resolved conductive/insulating domains within single nonwovens, paving the way for integrated thermal management systems with zone-specific properties. The transition from bulk anisotropy to designed heterogeneity represents the next frontier in fibrous material engineering.

3.3 3D sponges

Concluding the thesis in the third and final chapter, the expansion from 2D nonwovens to the highest spatial dimension through the introduction of the third dimension represents a significant advancement in material design. These 3D fiber sponges offer highly porous systems with accessible pores, yet they also exhibit the highest complexity among electrospun architectures. The integration of the third dimension becomes essential to overcome the inherent limitations of 2D materials, particularly their restricted porosity and their lack of functional integration and adaptability to complex environments.[25,136,137]

The fabrication of porous macroscopic 3D sponges with porosities exceeding 99 % based on electrospun fibers has been successfully established through various approaches. Techniques such as freeze drying of short electrospun fiber suspensions were developed to enable controllable pore architecture with remarkable material diversity.[25] A critical step in expanding the application potential lies in the targeted functionalization of such sponges. This work implemented a combinatorial approach that simultaneously modified both the sponge morphology by incorporating BOS fibers and achieved precise blending of AgNWs prior to freeze drying to ensure homogeneous nanofiller distribution throughout the 3D volume. The composite fiber system also integrated pyridine units within the beads that also function as dynamic anchor groups for the AgNWs,[138] thereby promoting the attachment of the anisotropic nanofiller along the pore-forming fibers. This architectural strategy aims to address the evolving challenges of achieving efficient thermal and electrical percolation as the system transitions from 2D to 3D architectures.

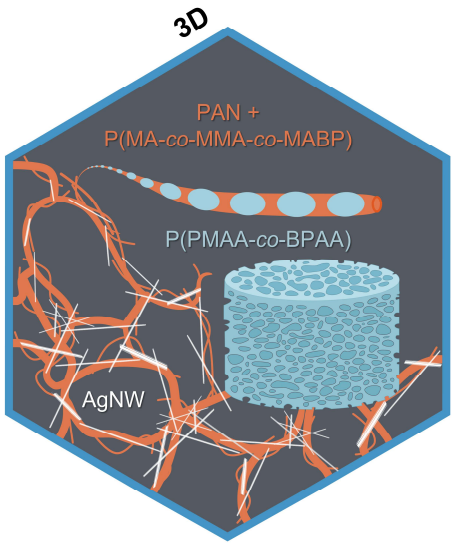

Figure 46: Overview illustrating the third chapter's content, introducing the realization of 3D BOS sponges composed of short electrospun fibers that are homogenously decorated with AgNWs.

All preparation of base polymers and electrospun BOS fibers, their analysis as well as the fabrication of neat string, bead and BOS fiber sponges was conducted by Marius Schmidt (Macromolecular Chemistry II, Prof. Dr. Andreas Greiner).

3.3.1 Polymer synthesis

To fabricate the BOS composite fibers, two distinct copolymers were required: poly(methyl acrylate-*co*-methyl methacrylate-*co*-(4-benzoylphenyl)methacrylate) (P(MA-*co*-MMA-*co*-MABP)) for the string component and poly(*N*-(pyridin-4-ylmethyl)acrylamide-*co*-*N*-(4-benzoylphenyl)acrylamide) (P(PMAA-*co*-BPAA)) for the bead domains. The string polymer, P(MA-*co*-MMA-*co*-MABP), has previously been utilized and is well-established for producing electrospun fibers.[139] In contrast, the bead polymer, P(PMAA-*co*-BPAA), exhibits sufficient incompatibility with the string component, which facilitates the formation of discrete beads along the fiber during processing, as discussed in the following Chapter 3.3.2.

Both copolymers were synthesized *via* free radical polymerization by Marius Schmidt (Macromolecular Chemistry II, Prof. Dr. Andreas Greiner) (see Scheme 1). Initially, P(NAS-*co*-BPAA) was obtained by copolymerizing *N*-acryloxy-succinimide (NAS) with *N*-(4-benzoyl phenyl)acrylamide (BPAA). In a subsequent step, 4-(aminomethyl)pyridine was employed to transform the NAS units *via* post-polymerization modification, yielding the desired P(PMAA-*co*-BPAA) copolymer. The synthesis of P(MA-*co*-MMA-*co*-MABP) was carried out using the same polymerization approach, starting from methyl acrylate (MA), methyl methacrylate (MMA), and (4-benzoylphenyl)methacrylate (MABP), adapting protocols from literature.[139]

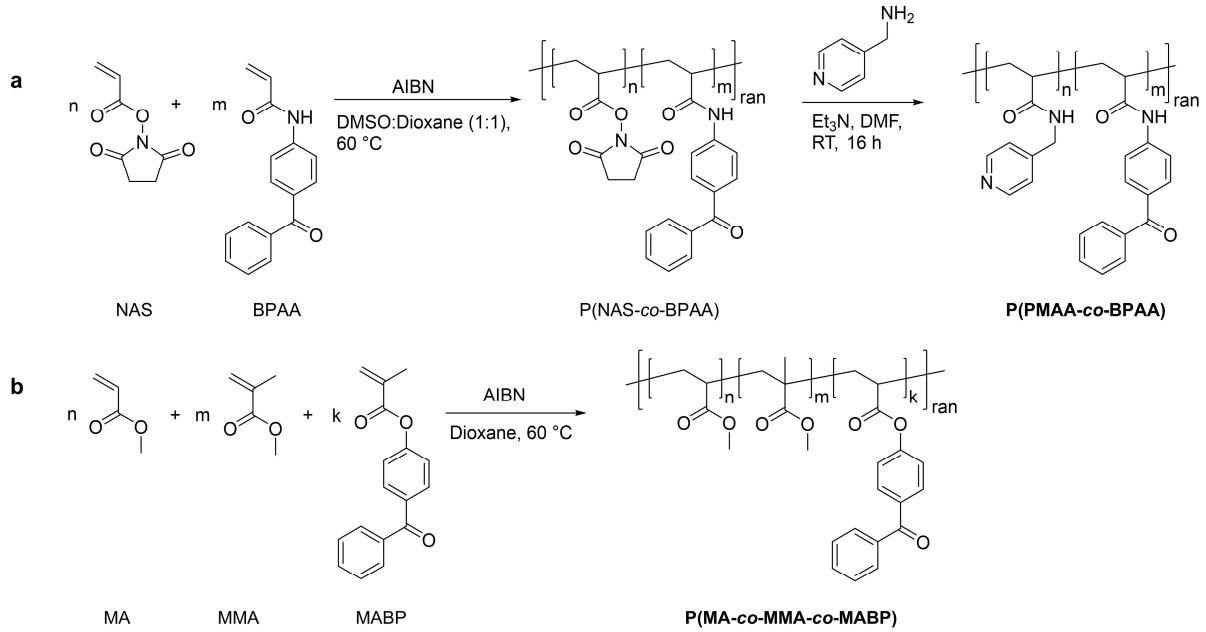

Scheme 1: Free radical polymerization of P(NAS-*co*-BPAA) and its subsequent modification with 4-(aminomethyl)pyridine to obtain P(PMAA-*co*-BPAA) (**a**) and free radical polymerization of P(MA-*co*-MMA-*co*-MABP) (**b**).

The bead copolymer P(PMAA-*co*-BPAA), synthesized *via* a two-step reaction approach, was subjected to analytical characterization proving first the complete conversion of 4-(aminomethyl)pyridine. This was realized by FT-IR spectroscopy and demonstrates the disappearance of the characteristic ester and imide vibrations associated with the NAS units after the post-polymerization modification, as depicted in Figure 47b. GPC chromatograms, presented in Figure 47c, reveal a shift to lower molar mass after the post-polymerization modification yielding an apparent number average molecular weight $M_{n,app}$ of 85 000 g/mol, apparent weight average molecular weight $M_{w,app}$ of 224 000 g/mol and a polydispersity index $Đ$ of 2.6. Finally, the copolymer composition was determined using ^{1}H-NMR spectroscopy (see Figure 47d). The results confirm a molar ratio of NAS to BPAA of 95:5 mol%, matching with the intended copolymer composition. The calculation was adapted from SCHMIDT et al.[140]

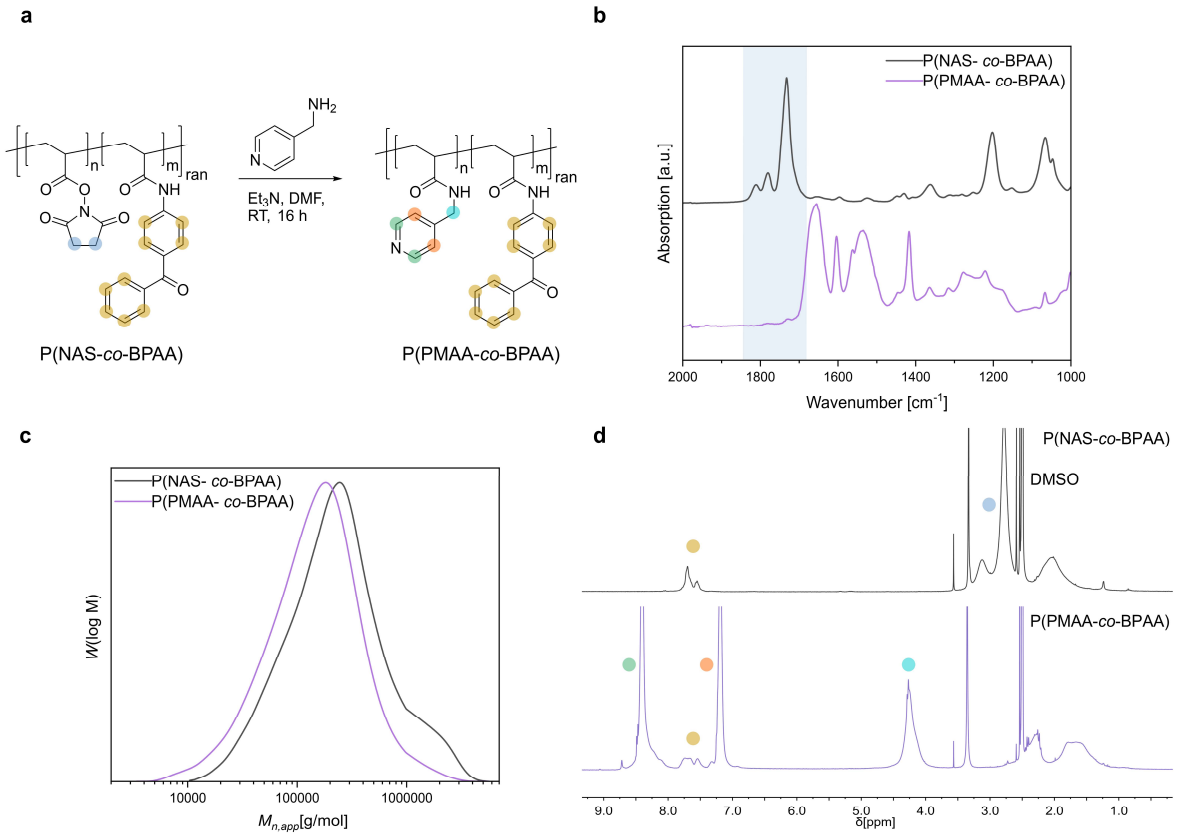

Figure 47: Post-polymerization modification and characterization of P(NAS-*co*-BPAA) copolymers: Reaction scheme for the aminolysis of P(NAS-*co*-BPAA) with 4-aminomethylpyridine, converting NAS units into PMAA *via* substitution of the succinimide ester (**a**), FT-IR spectra showing the disappearance of ester and imide vibrations highlighted in blue (**b**), GPC chromatograms demonstrating a shift to lower molar mass for the final P(PMAA-*co*-BPAA) (**c**) and ^{1}H-NMR of both copolymers in DMSO-d$_6$ (**d**).

The analytical procedures were all done by Marius Schmidt (Macromolecular Chemistry II, Prof. Dr. Andreas Greiner) and were repeated for the string copolymer, P(MA-*co*-MMA-*co*-MABP), which was synthesized in a single step polymerization without further modification.

The GPC chromatogram, as presented in Figure 48b, quantifies an apparent number average molecular weight $M_{n,app}$ of 94 000 g/mol, apparent weight average molecular weight $M_{w,app}$ of 214 000 g/mol and a polydispersity index $Đ$ of 2.3. The copolymer composition determined *via* ^{1}H-NMR spectroscopy reveals a molar ratio of MA, MMA, and MABP of 55:39:6 mol%, respectively (see Figure 48c). This result matches with the intended incorporation ratio of the monomer units into the final copolymer structure. The calculation of this ratio was adapted again from the method described by SCHMIDT et al.[140]

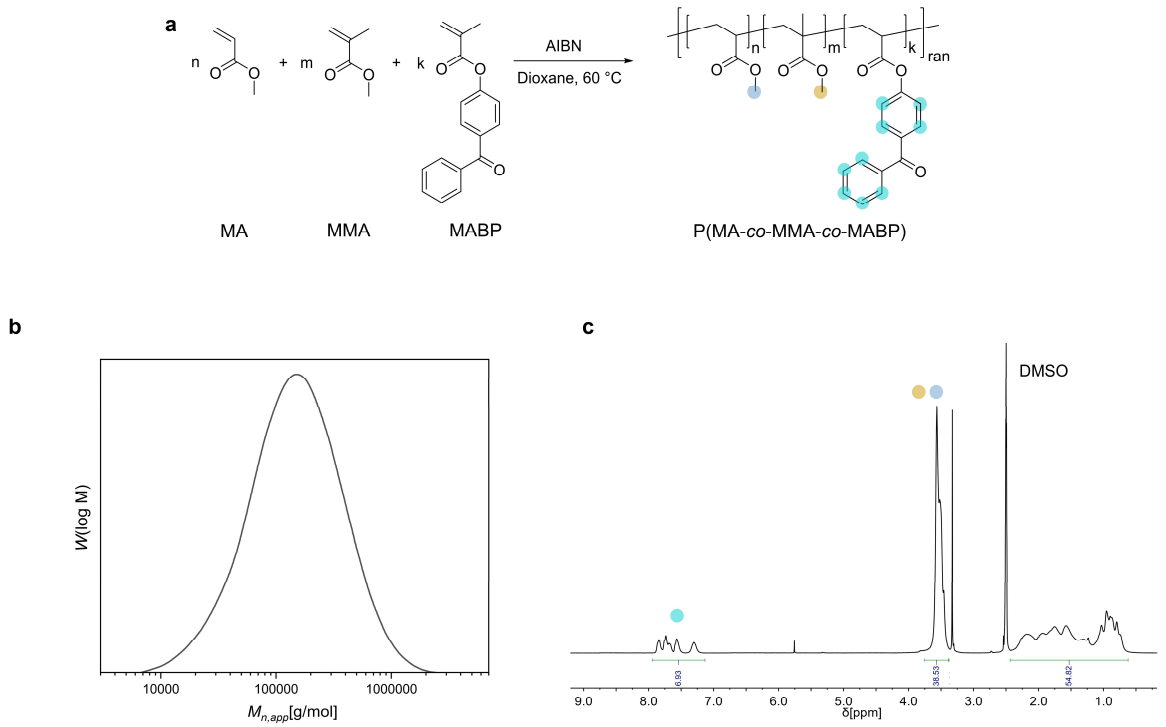

Figure 48: Polymerization and characterization of P(MA-*co*-MMA-*co*-MABP): Reaction scheme for the free radical polymerization of MA, MMA and MABP leading to corresponding copolymer (**a**) as well as GPC chromatograms (**b**) and ^{1}H-NMR of the copolymer in DMSO-d_6 (**c**).

TGA and DSC curves for both copolymers are provided in Chapter 7, Figure 71, offering addition insight into the respective thermal properties and stability.

3.3.2 Nonwoven preparation

The fabrication of BOS fibers was done by Marius Schmidt (Macromolecular Chemistry II, Prof. Dr. Andreas Greiner) using Side-by-Side Electrospinning, as illustrated in Figure 49. This approach provides localized mechanical reinforcement at the fiber-fiber junctions within the composite network. The formation of these distinctive structures relies on the control of key electrospinning parameters, such as solvent volatility, polymer selection, and concentration. A key prerequisite is a significant incompatibility between the bead and string polymers, driven by a sufficient difference in their HILDEBRAND solubility parameters, which prevents molecular mixing and promotes phase separation during processing.[140,141]

Additionally, solvents with high boiling points, such as DMF, are essential to ensure sufficient time for RAYLEIGH instabilities and viscoelastic effects to drive bead formation before fiber solidification. Without this extended processing window, rapid solvent evaporation would favor the formation of janus fibers rather than the desired BOS morphology.[140,141] For the electrospinning process, both copolymer solutions were prepared in DMF and positioned side-by-side in the electrospinning set-up. The string component, P(MA-*co*-MMA-*co*-MABP), was further blended with PAN, following established protocols in the literature to enhance fiber formation and mechanical properties.[139] Further analytical data on the PAN spinning material can be found in Chapter 5.1 (see Table 6) and Chapter 7 (see Figure 60a). The bead component, P(PMAA-*co*-BPAA), was processed as a pure solution. Notably, the presence of BPAA units within the copolymer enables subsequent UV crosslinking of the composite fibers, imparting significant solvent resistance. This feature is essential for the subsequent preparation of short fiber suspensions for the realization of 3D sponges, as discussed in the following Chapter 3.3.3.

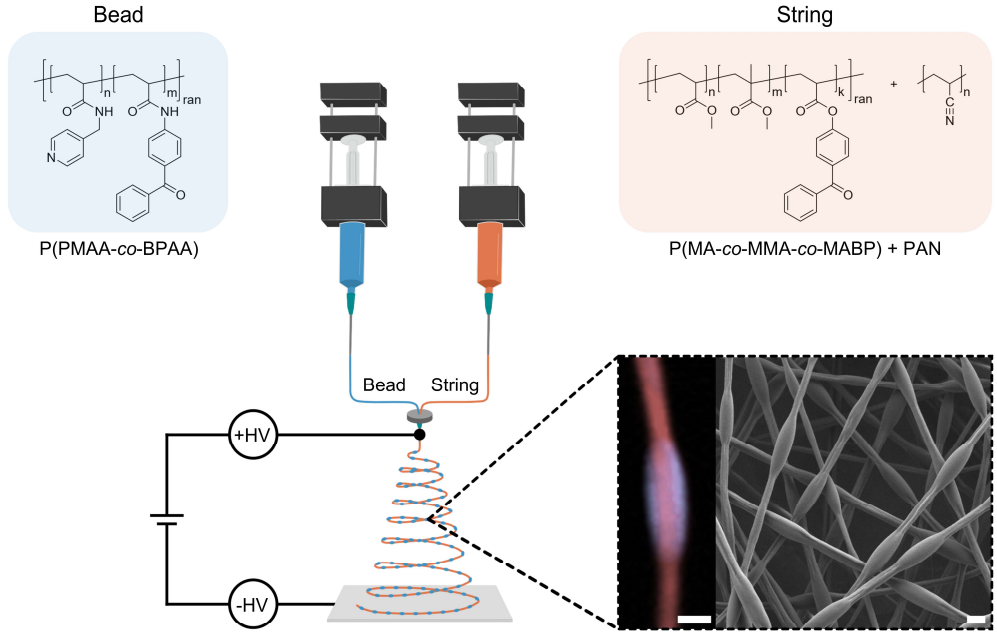

Figure 49: Illustration of the BOS fiber preparation *via* Side-by-Side Electrospinning: feeding a blend of P(MA-*co*-MMA-*co*-MABP) and PAN serving as the string material (colored in orange) alongside P(PMAA-*co*-BPAA) serving as the bead material (colored in blue). The fiber morphology is further visualized in spatial distributions extracted from RAMAN imaging (using the same color code) and a SEM image (1 µm scale bar).

The morphology and spatial distribution of the two distinct polymer phases within the BOS fibers were thoroughly investigated by Marius Schmidt (Macromolecular Chemistry II, Prof. Dr. Andreas Greiner) using RAMAN imaging and SEM. These analyses, as depicted in Figure 49, provide clear evidence for the successful separation and periodic alignment of beads along the continuous string fibers.

RAMAN spectra further quantify this structural assignment. The spectra presented in Figure 50 highlight the characteristic nitrile stretching vibration of PAN at 2245 cm^{-1},[142] which is exclusively detected in the string-forming phase of the fibers. In contrast, the spectrum corresponding to the bead region lacks this distinctive band, confirming the absence of PAN in the bead domains and thereby verifying the successful material separation within the composite structure.

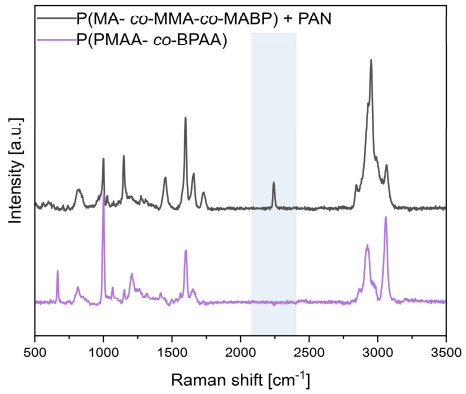

Figure 50: RAMAN spectra of the BOS fiber components consisting of a blend of P(MA-*co*-MMA-*co*-MABP) and PAN (string) as well as P(PMAA-*co*-BPAA) (bead). The blue area highlights the characteristic nitrile stretching vibration of PAN at 2245 cm^{-1} within the string domain.[142]

In addition to the BOS fibers, single-component fibers were also fabricated from the individual string and bead copolymers to enable a direct comparison of their intrinsic morphological characteristics. The preparation of these neat fibers allowed for a systematic study of the material-specific properties in isolation, providing a reference for evaluating the composite BOS architecture. A comparative analysis of SEM images, as presented in Figure 51a, highlights the morphological differences among the string, bead, and BOS fibers. Quantitative evaluation of the fiber diameters, summarized in Table 4, demonstrates that the single component fibers exhibit a high degree of homogeneity in their diameter, reflecting the uniformity of the electrospinning process. The processing parameters were specifically adjusted to closely match the string diameter of the BOS fibers, to isolate the influence of the beads.

Table 4: Results of the fiber diameter determination resulting from SEM images of the different string, bead and BOS fibers.

Sample		**Fiber diameter [µm]**
String		0.55 ± 0.09
Bead		0.54 ± 0.08
BOS	String	0.53 ± 0.10
	Bead	0.89 ± 0.21

In contrast, the BOS fibers reveal a distinct structural feature: while the string segment within the BOS fibers maintains its diameter, the bead domains are significantly thicker. This pronounced increase in diameter at the bead sites quantifies the thickening effect imparted by the bead shell surrounding the core string fiber.

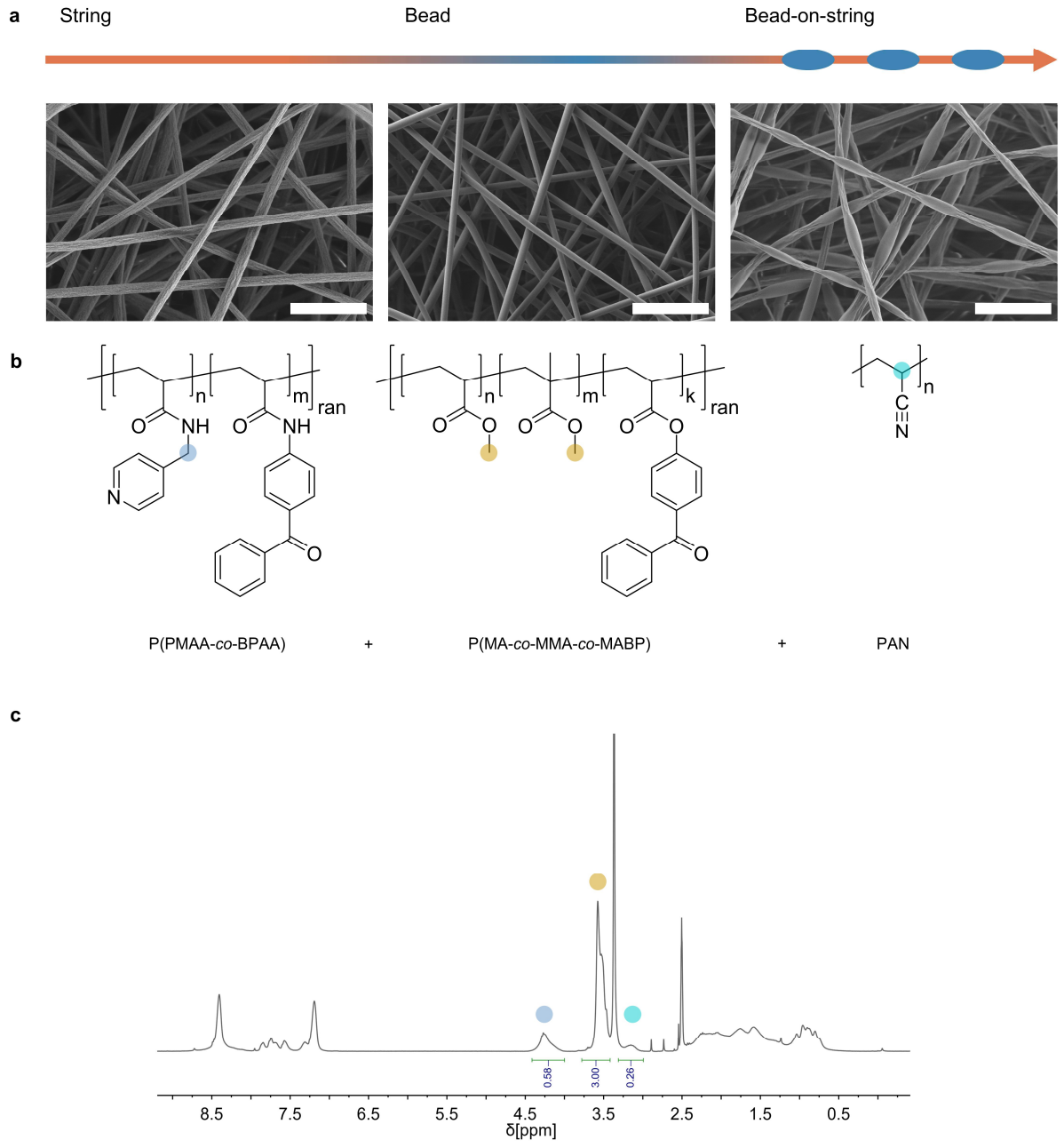

Figure 51: SEM images of neat string, bead and composite BOS fibers (5 µm scale bar) (**a**) and molecular illustrations of the BOS fiber components color-coded according to proton assignments (**b**) from the ^{1}H-NMR spectrum of the BOS fibers in DMSO-d_6 (**c**).

Finally, the ratio of bead and string segments within the BOS composite nonwovens was quantitatively determined by analyzing the ^{1}H-NMR spectrum (captured by Marius Schmidt (Macromolecular Chemistry II, Prof. Dr. Andreas Greiner) presented in Figure 51c.

This analysis involved integrating the characteristic signals corresponding to P(PMAA-*co*-BPAA), P(MA-*co*-MMA-*co*-MABP), and PAN, as depicted in Figure 51b (for determination of the corresponding wt% see Chapter 5.1 - NMR). The results yield a bead content of 29 wt% complemented with a 71 wt% string content.

The established BOS fibers serve as a robust foundation for subsequent processing steps, particularly the formation of highly porous 3D sponges. Moreover, the presence of P(PMAA-*co*-BPAA) bead domains within the fibers introduces functional anchor points, which are crucial for the integration of AgNWs, thereby enabling advanced functionalization strategies for the resulting sponge materials.

3.3.3 Sponge preparation

The fabrication of 3D sponges from short electrospun fibers is a well-established approach in literature, offering a versatile platform for creating highly porous and mechanically robust 3D architectures.[143] As illustrated in Figure 52, the process typically starts by mechanically cutting electrospun fiber mats and dispersing them in an appropriate solvent with the help of a blender, resulting in a stable fiber suspension. In the next step, this fiber suspension is transferred into a container and subsequently freeze-dried. During the sublimation step, the solvent crystals act as templates, generating a network of interconnected pores throughout the sponge matrix.[139] This freeze-drying technique is particularly advantageous, as it preserves the original fiber morphology and ensures a uniform distribution of fibers within the resulting 3D structure. Once the 3D sponge has been formed, various functionalization strategies can be applied. Most commonly, post-fabrication modification is achieved through dip-coating methods, which allow for the introduction of additional functionalities such as hydrophobicity, conductivity, or catalytic activity.[83,144,145]

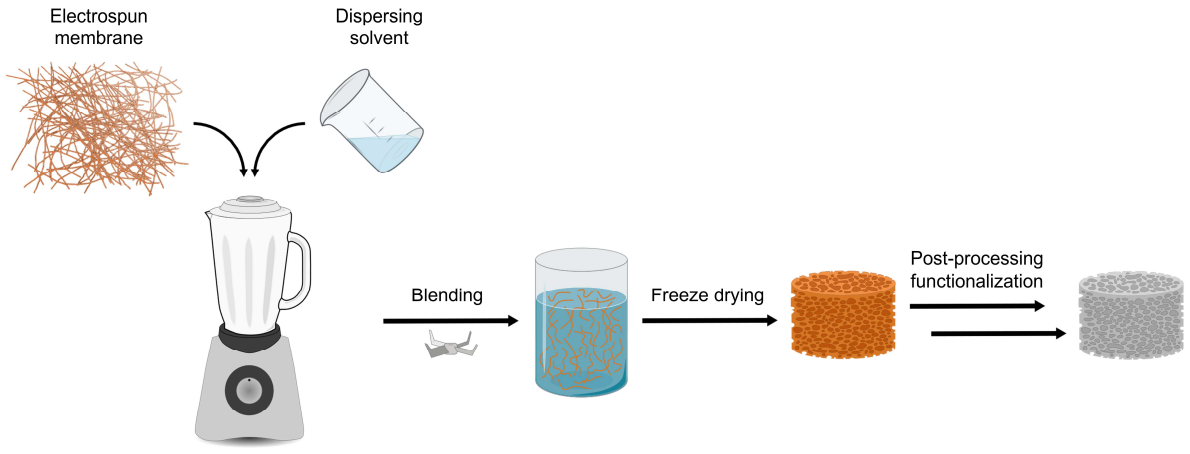

Figure 52: Illustration of the established multistep dip-coating approach used in literature for functionalizing 3D sponges produced by freeze drying short electrospun fibers.

In the functionalization of 3D BOS sponges with AgNWs, the common multi-step dip-coating approach has been replaced by a more efficient one-step blending approach. The dip-coating technique, illustrated in Figure 53a, involved immersing preformed sponges into AgNW-containing solutions, which often led to a superficial and uneven distribution of nanowires, with fillers predominantly localized near the surface rather than throughout the sponge matrix.[83,146] This also restricted the formation of a continuous conductive network utilizing the whole sponge volume. To address these shortcomings, the new one-step blending method was introduced. In this approach, AgNW suspensions were mixed directly with the short fiber suspension before the freeze-drying step that forms the sponge, as depicted in Figure 53b. This modification in the preparation protocol ensures that the nanowires are distributed homogeneously throughout the entire sponge, effectively overcoming the surface-localization issues associated with dip-coating.[83,146] Furthermore, the blending approach shall facilitate a process analogous to phase separation, leading to an *in situ* organization of the AgNWs along the emerging phase boundaries - namely, the pore walls. While previous studies have demonstrated the self-organization of AgNWs at phase boundaries in porous 2D bulk polymer matrices, this study extends the concept to a 3D porous sponge architecture.[147]

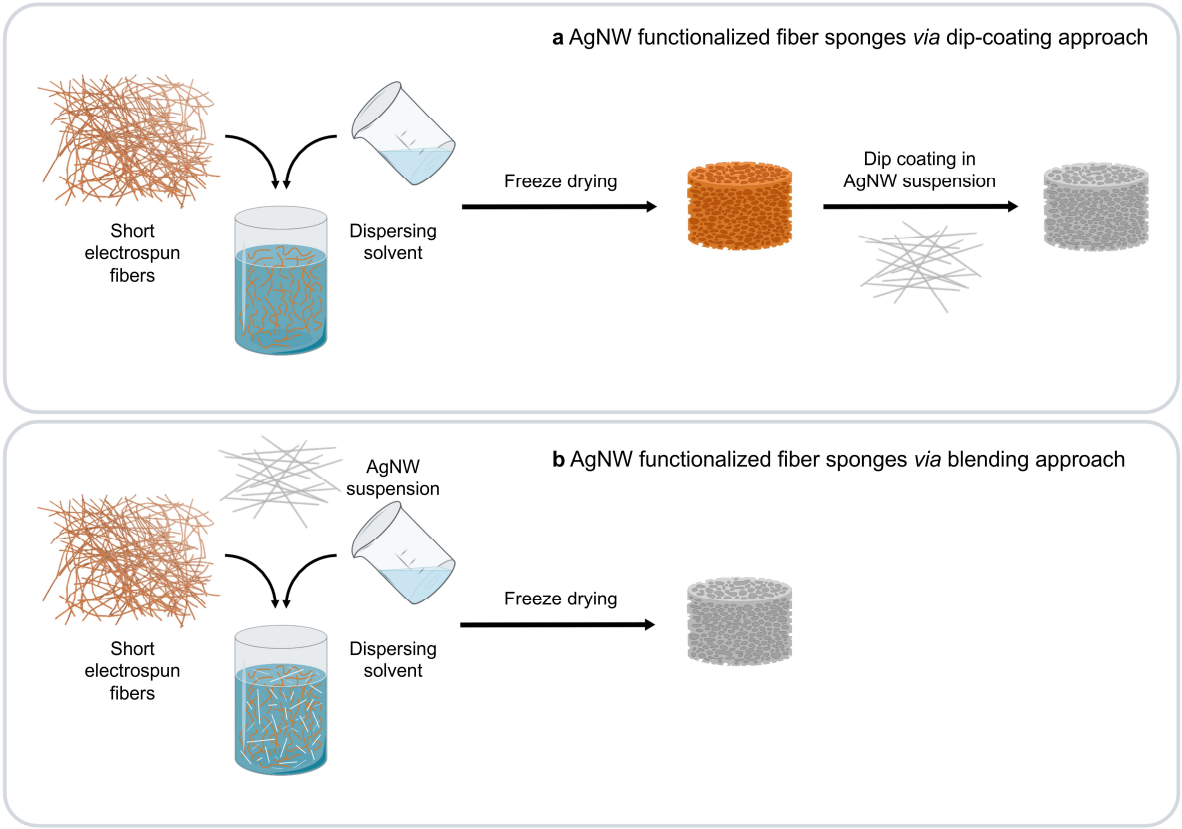

Figure 53: Comparative illustration of the conventional multistep dip-coating approach, where 3D sponges are functionalized with AgNWs after freeze drying short electrospun fiber suspensions (**a**) and the new one-step blending approach, in which AgNWs are incorporated prior to freeze drying (**b**).

Additionally, the structural organization is enhanced by the incorporation of a bead-forming copolymer such as P(PMAA-*co*-BPAA), which introduces dynamic Ag-N coordination bonds with the AgNWs. These bonds are capable of reversibly breaking and reforming under mechanical deformation, allowing the nanowires to reorient and dissipate energy while maintaining robust interfacial connectivity.[138]

To fabricate the neat 3D BOS sponges, short fibers with lengths ranging from 70 to 200 µm were first generated by cutting the fiber membranes in solution. Two distinct types of 3D sponges were then realized by varying the initial short fiber concentration c_{SF}, specifically using concentrations of 5.00 mg/mL and 8.76 mg/mL. Sponges resulting from a c_{SF} of 5.00 mg/mL display a density of approximately 10 mg/cm^3. However, the presence of beads along the BOS fibers results in a lower fiber count in these sponges compared to reference sponges composed solely of neat bead or string fibers. To achieve a comparable number of fibers to the neat fiber sponges, the BOS sponges were also prepared with a higher short fiber concentration of 8.76 mg/mL, which led to a density of approximately 14.2 mg/cm^3. This adjustment compensates for the additional mass contributed by the beads on the BOS fibers.

The freeze-drying process applied to the BOS short fiber suspensions consistently yields highly porous sponges. The porosity *P* of the two types of neat BOS sponges was determined with the following expressions:[148]

$$P = \left(1 - \frac{\rho_{sponge}}{\rho_{bulk}}\right) \cdot 100\ \% \tag{3}$$

$$\rho_{sponge} = \frac{m_{sponge}}{V_{sponge}} \tag{4}$$

P: porosity, ρ_{sponge}: density of the sponge, ρ_{bulk}: density of the bulk was equated with the density of PAN (1.16 g/cm^3),[149] m_{sponge}: mass of the sponge, V_{sponge}: volume fraction of the sponge.

This results in porosities of 99.2 % for the 5.00 mg/mL sponges and 98.5 % for the 8.76 mg/mL.

The composite 3D BOS sponges were further complemented with AgNWs. The AgNWs were synthesized following the established protocol described in Chapter 3.1.3, resulting in a new aqueous suspension, referred to as the $AgNW_{3D}$ batch, with a concentration of 1.9 wt%. These nanowires exhibit diameters of approximately 125 nm and lengths ranging from 11 to 41 µm, ensuring a high aspect ratio suitable for network formation within the sponge structure. For the functionalization process, the AgNW suspensions were thoroughly mixed with the short fiber suspensions before the freeze-drying step, enabling a homogeneous distribution of nanowires throughout the composite suspension.

This preparative strategy allowed for the fabrication of eight distinct sponge types by systematically varying two key parameters: the short fiber concentration c_{SF} (5.00 and 8.76 mg/mL), and the AgNW volume V_{AgNW} (0.0, 0.2, 0.4, 0.6 mL). It was not possible to add more AgNW suspension, as higher amounts of nanowires caused the sponge to collapse due to the excessive nanowire content (see Chapter 7, Figure 72a). Figure 54 provides a visual summary of these parameters and shows representative images of the resulting 3D BOS sponges. These two parameters (c_{SF} and V_{AgNW}) define the nomenclature that is used throughout the following discussion, facilitating clear identification of sponge types. By increasing the AgNW content, the experimental design enables a systematic investigation into how the presence and concentration of nanowires influence the mechanical, thermal, and electrical conductivity properties of the 3D BOS sponges.

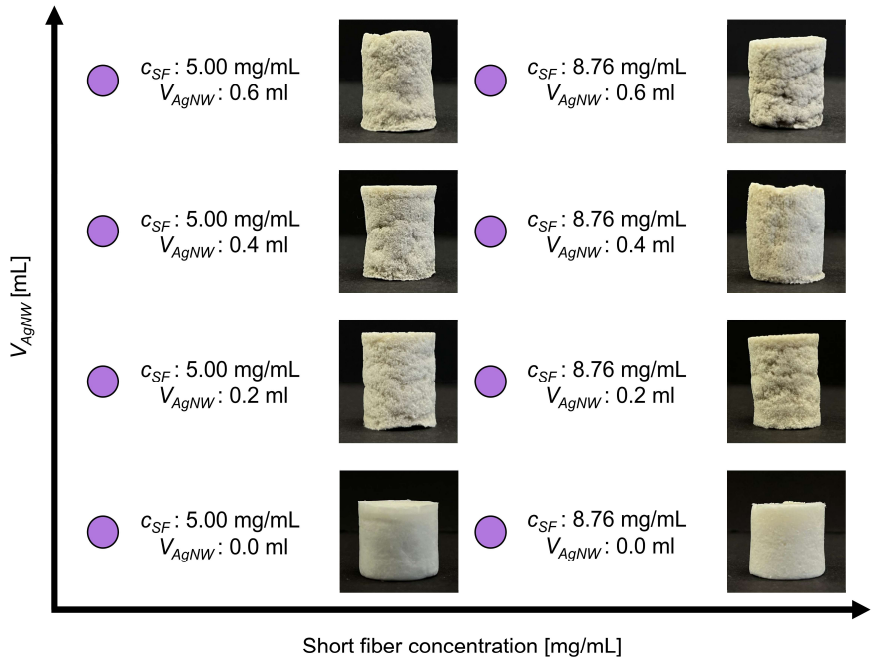

Figure 54: Illustration of different 3D BOS sponge types based on short fiber concentration c_{SF} and AgNW volume V_{AgNW} alongside optical images of the corresponding sponges.

The BSE-SEM images presented in Figure 55 offer a comprehensive view of the various 3D BOS sponges, highlighting how AgNWs integrate within the porous fiber network. In these images, the AgNWs appear distinctly bright against the darker background of the sponge matrix. Notably, the nanowires predominantly attach to the walls of the pores rather than being suspended in the open void spaces, reinforcing the pore structure. This selective localization also facilitates direct contact between adjacent nanowires, promoting the formation of a continuous network at higher nanowire loadings. This proximity is crucial for establishing effective nanowire-nanowire contacts and for maximizing the conductive pathways within the sponge.

The observed arrangement supports the intended concept of phase separation induced self-organization, where AgNWs are driven to assemble along the emerging phase boundaries - specifically, the pore walls - during the freeze-drying process.

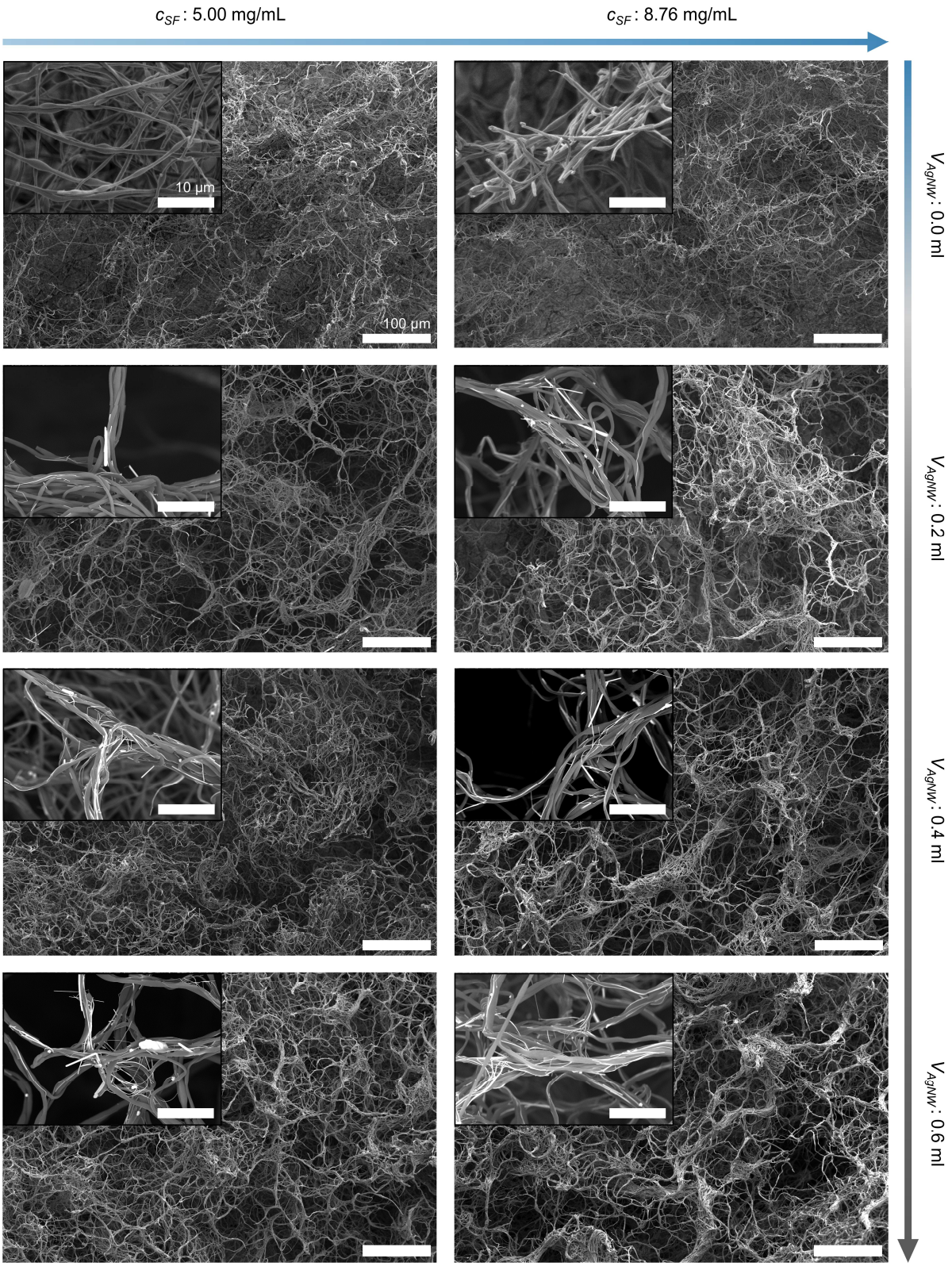

Figure 55: SEM images of different 3D BOS sponge types: Comparison based on short fiber concentration c_{SF} and AgNW volume V_{AgNW} revealing the incorporated AgNWs by using a BSE-detector (10 µm respectively 100 µm scale bar).

In addition to the morphological characterization of the 3D BOS sponges, a quantitative analysis of the silver content was conducted using ICP-OES, which delivered the silver concentration in wt% for each sample. The determination of the corresponding vol% is outlined in Chapter 5.1 - ICP-OES. Both values, as compiled in Table 5, demonstrate that the silver content in the sponges increases in direct proportion to the amount of AgNW suspension added during sample preparation, resulting in a maximum silver content of 13.8 wt% (1.7 vol%) at the highest loading for the 3D BOS sponge with a c_{SF} of 5.00 mg/mL.

Table 5: Silver content, compressive strength at 50 % compression $\sigma_{50\%\ comp}$ and thermal conductivity κ at 10 % and 50 % compression for 3D BOS sponges with varying short fiber concentration c_{SF} and AgNW volume V_{AgNW}.

Sample (c_{SF}; V_{AgNW})	**Ag content[a]**		**$\sigma_{50\%\ comp}$ [kPa][b]**	**$\kappa_{10\%\ comp}$ [W/m·K][c]**	**$\kappa_{50\%\ comp}$ [W/m·K][c]**
	[wt%]	**[vol%]**			
5.00 mg/mL; 0.0 mL	-		1.8 ± 0.1	0.0178	0.0218
5.00 mg/mL; 0.2 mL	5.0 ± 0.6	0.6 ± 0.1	4.1 ± 0.1	0.0195	0.0241
5.00 mg/mL; 0.4 mL	10.7 ± 1.5	1.3 ± 0.2	5.7 ± 0.7	0.0220	0.0255
5.00 mg/mL; 0.6 mL	13.8 ± 2.8	1.7 ± 0.4	6.3 ± 1.0	0.0203	0.0256
8.76 mg/mL; 0.0 mL	-		4.2 ± 0.8	0.0200	0.0242
8.76 mg/mL; 0.2 mL	5.6 ± 1.1	0.7 ± 0.1	7.1 ± 1.1	0.0202	0.0261
8.76 mg/mL; 0.4 mL	9.4 ± 1.5	1.1 ± 0.2	10.8 ± 0.6	0.0216	0.0280
8.76 mg/mL; 0.6 mL	13.6 ± 3.1	1.6 ± 0.4	13.4 ± 3.2	0.0221	0.0298

[a] determined from ICP-OES, [b] determined from tensile testing, [c] determined from MTPS (5 % inaccuracy).

Compression tests (illustrated in Figure 56) confirm that all sponge types retain partial recovery after 50 % strain. The compressive strength $\sigma_{50\%\ comp}$ exhibits a distinct upward trend correlated with AgNW content and distribution homogeneity. For instance, sponges with higher AgNW loading (e.g., c_{SF} of 8.76 mg/mL and V_{AgNW} of 0.6 mL) achieved $\sigma_{50\%\ comp}$ values up to 13.4 ± 3.2 kPa. This enhancement contrasts with dip-coated SiO_2 sponges reported by FANG et al., where inhomogeneous AgNW distribution caused mechanical destabilization due to localized stress concentrations and poor nanowire integration.[83] Concurrently, the intrinsic BOS fiber architecture itself contributes significantly to mechanical stability. Neat string fiber sponges (with a c_{SF} of 5.00 mg/mL) exhibit $\sigma_{50\%\ comp}$ of 1.3 ± 0.2 kPa, while bead-only counterparts show even lower strength (0.7 ± 0.1 kPa). The BOS sponge structure therefore synergistically combines bead reinforcement at nodal points with string fiber continuity. This yields in a 28 % and 61 % improvement in compressive strength of the 3D BOS sponge with a c_{SF} of 5.00 mg/mL (1.8 ± 0.1 kPa) over neat string and bead sponges, respectively.

This highlights the crucial role of morphological hierarchy in stress dissipation, where beads act as microstructural knots preventing fiber slippage under load.

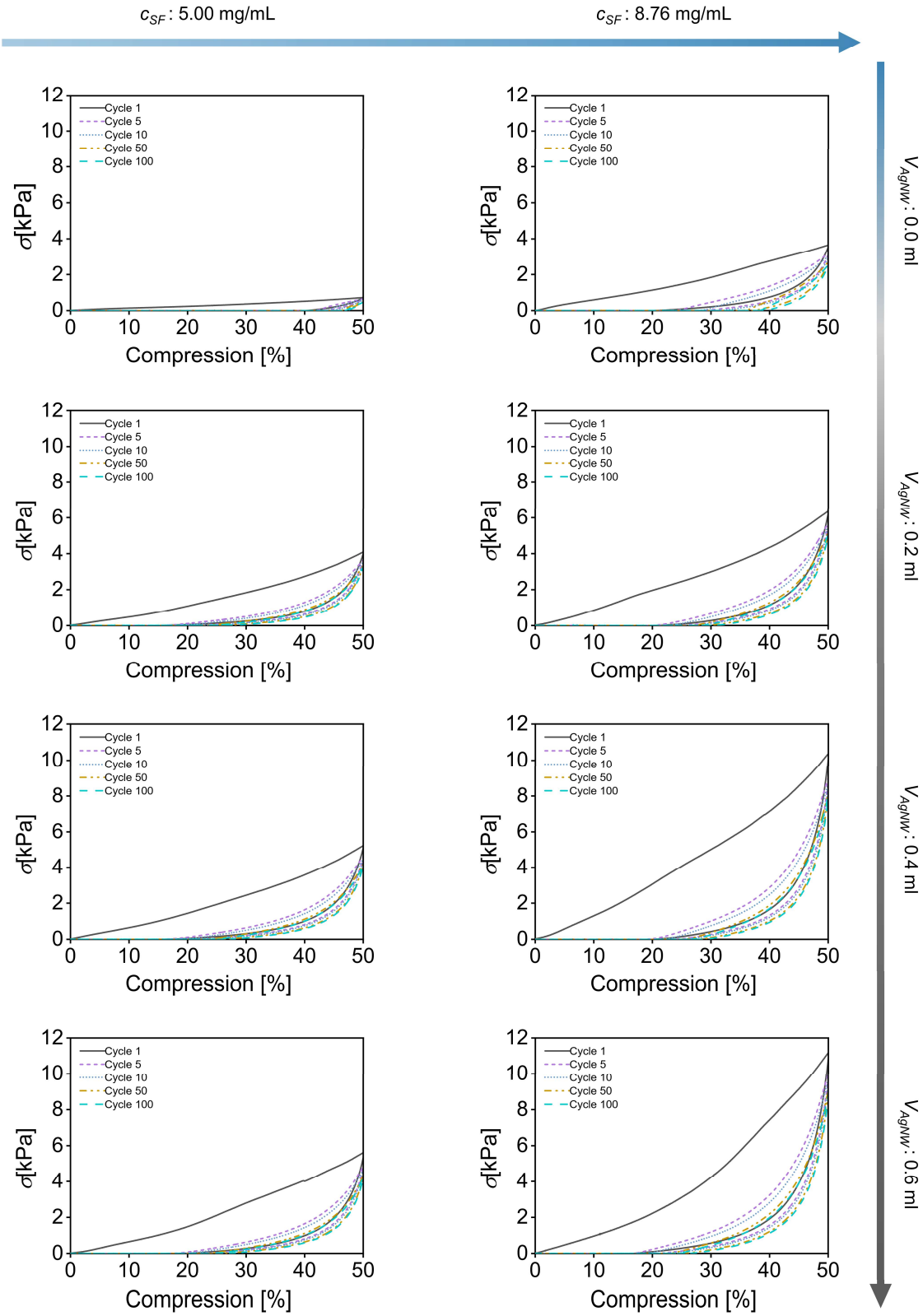

Figure 56: Mechanical analysis of different 3D BOS sponge types: Comparison based on short fiber concentration c_{SF} and AgNW volume V_{AgNW}.

Thermal conductivity measurements were conducted by Ina Klein (Physical Chemistry I. Prof. Dr. Markus Retsch) using the Modified Transient Plane Source (MTPS) technique at 10 % and 50 % compression, in order to ensure good contact with the sample. This method, distinct from the LIT employed in the previous chapters, was selected to accommodate the 3D porous architecture of the sponges. The third spatial dimension precludes the use of LIT due to its limitations in analyzing thick 3D structures. The results demonstrate a systematic increase in thermal conductivity κ with higher short fiber concentration c_{SF} and AgNW volume V_{AgNW} (see Table 5). Notably, a pronounced difference emerged between κ values at 10 % and 50 % compression for each sponge type, highlighting the sensitivity of thermal transport to mechanical deformation. This enhancement originates in the loss of free volume under compression, which reduces pore size and intensifies fiber-filler contact points. Such densification facilitates more efficient heat transfer through tighter interfacial connections, a phenomenon consistent with hierarchically porous materials. Structural compaction thus critically promotes phonon and electron transport pathways by promoting contact and minimizing thermal resistance at junctions.

Despite the incorporation of AgNWs (considering the high bulk silver thermal conductivity of ~ 450 W/m·K),[150] the sponges retain their thermally insulating character (κ < 0.03 W/m·K). This limited contribution arises from two key factors: the reduced intrinsic conductivity of AgNWs due to structural defects inducing grain boundary scattering, which lowers their thermal conductivity to approximately 45 % of bulk silver values,[123] and the absence of percolation, even at peak loading (13.8 wt%, 1.7 vol%), homogeneous dispersion prevented the formation of continuous conductive pathways. Consequently, phonon conduction along the BOS fiber matrix dominates thermal transport, while AgNWs primarily reinforce pore walls mechanically without significantly contributing to heat transfer. The κ values align with typical thermal insulators (0.01 - 0.1 W/m·K),[151] confirming that insulation properties persist despite metallic filler integration.

Sponges with higher c_{SF} (8.76 mg/mL) consistently exhibit superior κ values, attributable to the BOS architecture's ability to stabilize the fibrous network while maintaining high porosity (98.5 %). Both κ and mechanical performance initially increased with rising V_{AgNW} but plateau between 0.4 and 0.6 mL, indicating saturation in AgNW-mediated thermal and mechanical performance enhancement.

Even at the highest AgNW loading (V_{AgNW}: 0.6 mL, 13.8 wt%, 1.7 vol%), no measurable electrical conductivity was detected in the composite sponges. For these measurements, the sponges were clamped between two parallel metal electrodes, fully occupying the interelectrode space (for further procedure see Chapter 5.1 - 4PP). This absence of conductivity aligns with thermal conductivity data, which already indicated the lack of a continuous percolating AgNW network within the 3D architecture. Electrical percolation in AgNW-based systems depends critically on load quantity, nanowire aspect ratio, distribution homogeneity, and matrix porosity.[83,152–155] While high aspect ratio AgNWs can achieve efficient percolation at low volume fractions (0.7 vol%) in isotropic porous polyurethane systems,[147] the hierarchical porosity (> 99 %) of the presented 3D BOS sponge matrix significantly dilutes the effective nanowire concentration. This structural characteristic substantially elevates the percolation threshold.

The results indicate that establishing electrical continuity would require a denser nanowire network capable of bridging interconnected pore walls. Unfortunately, increasing the amount of nanowires was not possible in this system. This limitation is particularly relevant in the context of the homogeneous blending strategy applied here, which, while preventing localized nanowire aggregation, also hinders the formation of a sufficiently dense network necessary for electrical percolation.

To investigate and compare the limitations of the blending and dip-coating approach for achieving volumetric AgNW distribution, neat BOS sponges with short fiber concentrations c_{SF} of 5.00 and 8.76 mg/mL were dip-coated in aqueous AgNW suspensions with a V_{AgNW} of 0.6 mL, replicating the AgNW concentration used for the blending approach. The inherent hydrophilicity of the BOS sponge (see Figure 57), contrasting with the hydrophobic nature of neat string fiber sponges, ensured effective wetting during immersion. Electrical conductivity measurements of the dip-coated sponges yielded values of $0.50 \cdot 10^{-3}$ S/cm and 0.06 S/cm for c_{SF} of 5.00 mg/mL and 8.76 mg/mL, respectively. These values are significantly lower than the electrical conductivity of bulk silver ($6.16 \cdot 10^{7}$ S/cm) or pristine AgNWs (~ 50 - 65 % of bulk silver),[156] which is attributed to the high porosity, dead volume within the 3D matrix, and filler confinement effects. Nevertheless, the measured conductivities confirm percolation pathways in the dip-coated sponges due to a change in AgNW distribution across the 3D BOS sponge volume.

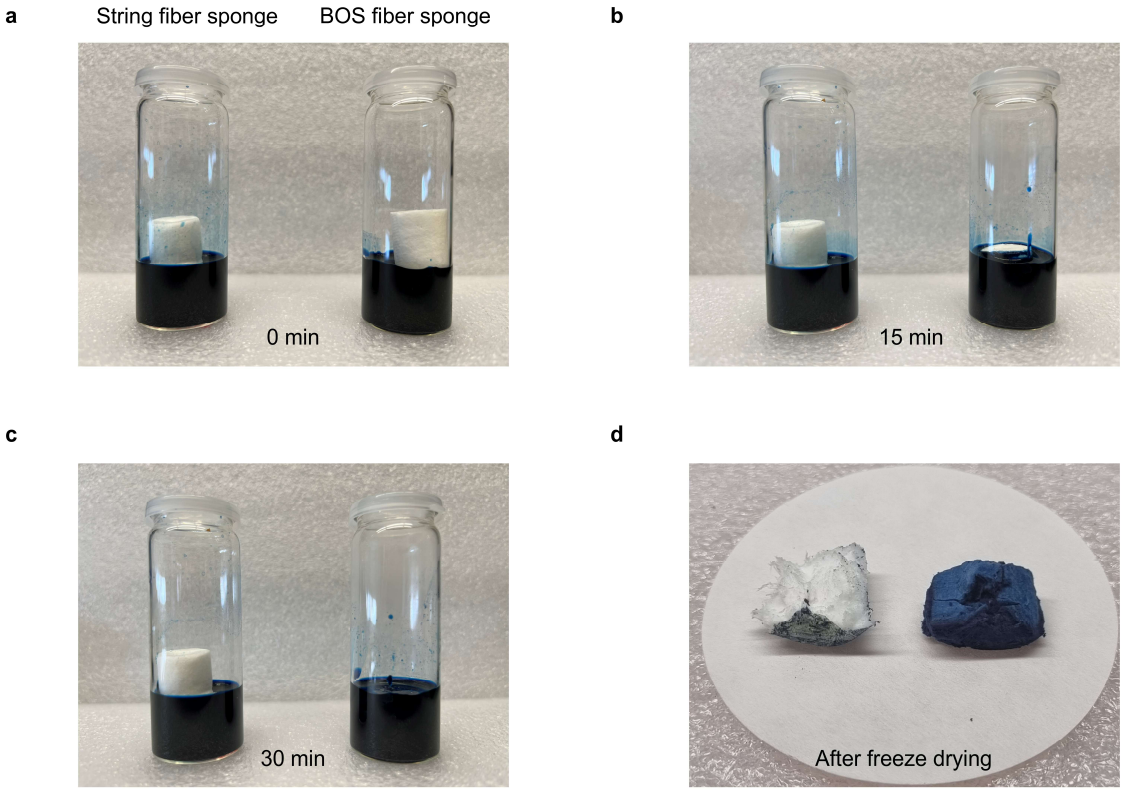

Figure 57: Comparison of hydrophilicity of the two 3D sponge types. In each optical image, the left vial contains the neat string sponge, while the right vial contains the BOS sponge after immersion in a wetting solution (colored with the dye *Wusitta Lebensmittelfarbe Blau*) for 0 (**a**), 15 (**b**) and 30 min (**c**). The final image shows cross-sections of both sponge types after freeze-drying (**d**).

SEM and EDX mapping in Figure 58a and b provide direct visualization of this AgNW distribution. The latter was performed by Martina Heider and Dr. Ulrich Mansfeld (Bayerisches Polymerinstitut, KeyLab Electron and Optical Microscopy). For sponges functionalized *via* blending approach, both outer and inner layers exhibit uniform AgNW dispersion, irrespective of c_{SF}. In contrast, dip-coated sponges display severe AgNW agglomeration limited to outer layers, with no significant penetration into the interior. This inhomogeneity intensifies at higher c_{SF}, explaining the enhanced conductivity observed for the sponge with a c_{SF} of 8.76 mg/mL. The conductivity set-up, which measured bulk resistance between parallel electrodes, primarily detected the '2D' percolation network formed in the sponge's surface shell - proximal to the electrodes but failing to utilize the full 3D volume. These results underscore the intrinsic limitation of dip-coating for achieving volumetric functionality in highly porous architectures.

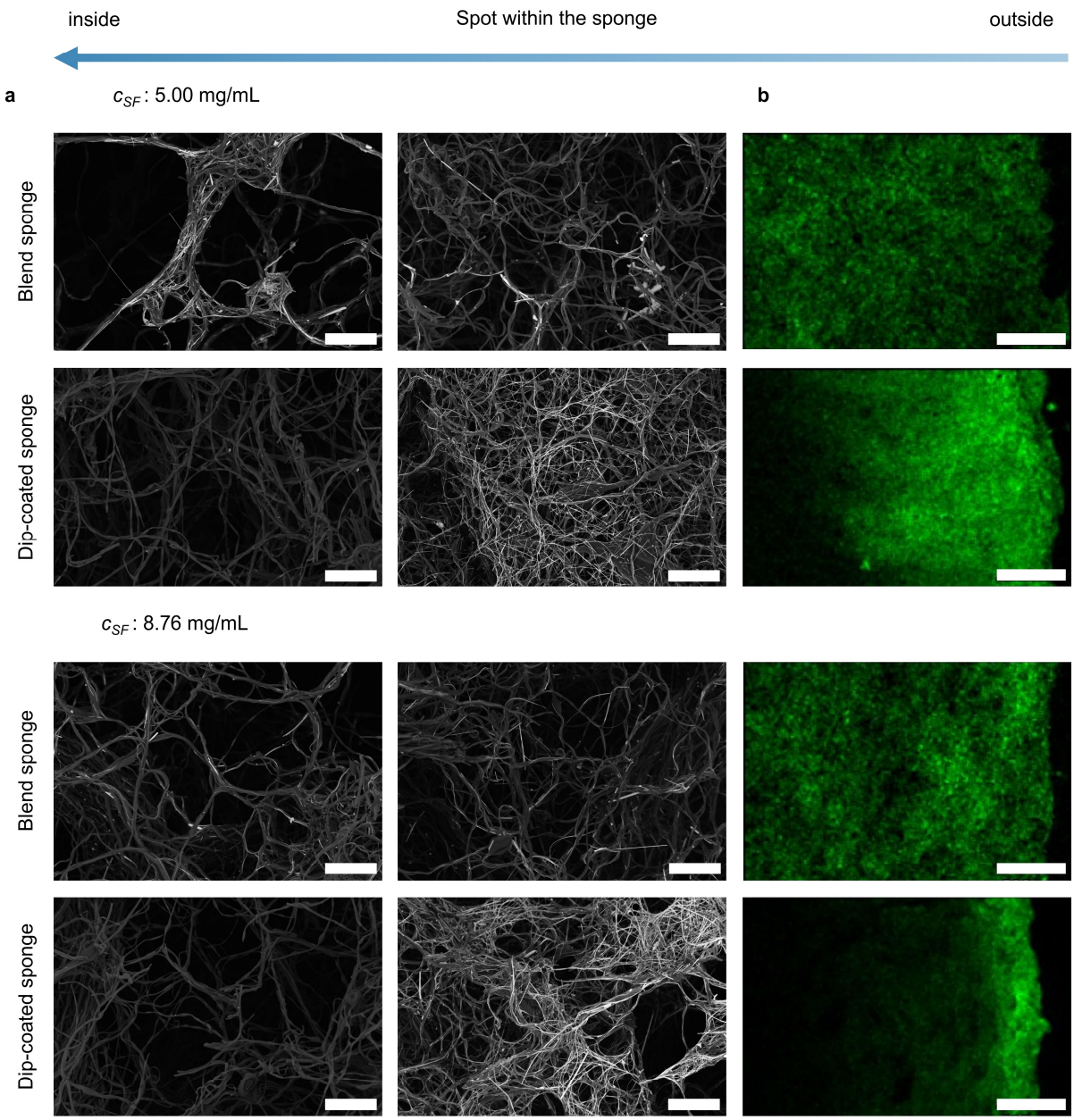

Figure 58: BSE-SEM images of AgNW functionalized sponges (V_{AgNW}: 0.6 mL) with two different short fiber concentrations c_{SF} (5.00 and 8.76 mg/mL), comparing the blending and dip-coating approaches for nanowire incorporation at different spots within the sponge (20 µm scale bar) (**a**). Corresponding EDX mapping images display the spatial distribution of silver (shown in green) within the sponge structure (500 µm scale bar) (**b**). These images demonstrate that the dip-coating approach results in a superficial and thus inhomogeneous distribution of AgNWs from the outside to the inside of the sponge, while the blending approach ensures a homogeneous distribution throughout the entire sponge volume.

In this chapter, a novel one-step blending approach was introduced for fabricating highly porous, mechanically robust 3D sponges that integrate BOS fiber architecture with homogeneous AgNW dispersion. This innovative strategy opened new possibilities through a synergistic dual reinforcement: the BOS fiber morphology combined with AgNW content significantly enhanced mechanical stability.

The enhanced compressive strength observed with increasing AgNW loading, while preserving high porosity levels, demonstrated that this dual reinforcement strategy exceeded the performance improvements achieved by sponges containing exclusively string or bead fibers. In contrast to conventional functionalization methods like dip-coating, the blending approach ensured uniform nanowire distribution throughout the entire sponge volume, thereby preventing surface-only functionalization and enabling true 3D filler penetration and distribution. The latter was particularly beneficial for achieving consistent mechanical properties.

However, this advancement also introduced new challenges. Despite the incorporation of conductive AgNWs, the sponges maintained their thermally insulating character. The thermal conductivity experienced only modest increases with elevated AgNW content, exemplified by values rising from 0.0178 W/m·K for neat BOS sponges to 0.0203 W/m·K at maximum AgNW loading (both measured at 10 % compression), with all measurements remaining within the established range for thermal insulators (0.01 - 0.1 W/m·K).[151] This behavior confirmed that AgNW incorporation does not compromise the insulating properties but rather produces controlled and limited thermal transport enhancement, attributed to the absence of a percolating AgNW network. Concurrently, this lack of percolation prevented electrical conductivity within the 3D sponge, emphasizing the fundamental challenges of establishing stable 3D electrical percolation networks at low nanowire volume fractions and the need to reevaluate "homogeneity" in 3D confinement. Unlike 2D systems, where uniform dispersion ensures percolation, 3D architectures may require strategically designed gradients.

To address these questions, dip-coating was implemented as a comparative strategy. These dip-coated 3D sponges exhibited measurable electrical conductivities ($0.50 \cdot 10^{-3}$ S/cm for a c_{SF} of 5.00 mg/mL and 0.06 S/cm for a c_{SF} of 8.76 mg/mL). SEM and EDX mapping investigations documented that AgNWs were predominantly localized at the sponge surfaces. Figure 59 provides comparative illustrations demonstrating this superficial 2D percolation accompanied by pore clogging with nanowires, rather than penetrating the whole 3D network. This surface-exclusive functionalization has been documented to induce mechanical destabilization and compromise structural integrity.[83] Consequently, the blending approach offers distinct advantages in preserving both mechanical robustness and homogeneous filler distribution, despite the absence of an electrically percolating network within the 3D sponge structure. The achievement of volumetric electrical conductivity therefore remains a significant challenge requiring future research attention.

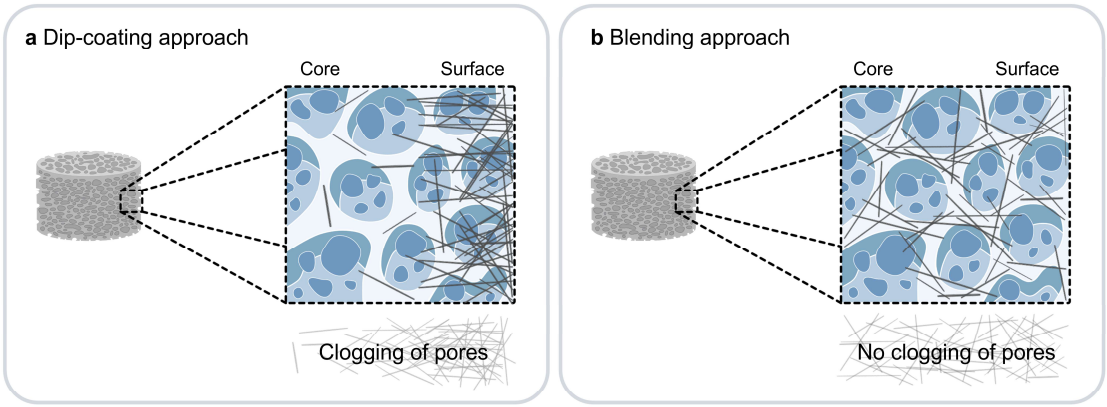

Figure 59: Illustration of functionalization approaches for 3D BOS sponges comparing the effects of the dip-coating (**a**) and blending approach (**b**) on the distribution of AgNWs within the porous system (colored in blue).

The findings highlight the difficulty of reconciling electrical functionality with mechanical stability in 3D porous architectures, while emphasizing the critical importance of matrix-filler connectivity and challenging established nanowire distribution concepts for localized property control. In comparison to the previous chapters that concentrated on coating and aligning anisotropic nanowires, this chapter demonstrates that in the third dimension, the distribution of nanofiller throughout the volume becomes the crucial factor for percolation.

This recognition necessitates the development of new conceptual frameworks that genuinely consider dimensionality and its associated prerequisites, including a reconsideration of homogeneity requirements and exploration of gradient-based approaches. Additional experiments were conducted that demonstrated multi-layered janus-type sponges featuring two unfunctionalized layers at the top and bottom, with an AgNW functionalized fiber layer positioned between them (see Chapter 7, Figure 72b). This configuration could serve as a foundation for future investigations examining distinct gradients in 3D confinement to enhance understanding and improve percolation thresholds in these systems, ultimately enabling multifunctional applications in sensing, insulation, and flexible electronics.

4 Conclusion and outlook

Within this work the integration of metallic nanofillers into hierarchical fibrous polymer networks of 1D, 2D and 3D confinement was investigated. The aim was to establish fundamental principles governing thermal and electrical transport properties by investigating the interplay between structural hierarchy, orientation, nanofiller characteristics, and integration methods. The work was guided by three main objectives. First, it sought to construct hierarchical fibrous networks using electrospinning and various set-ups to unlock all three spatial dimensions; second, to establish percolative pathways by incorporating commonly used conductive AgNWs as the main metallic mediator within these fibrous environments; and third, to investigate the influence of structural architecture and nanofiller integration principles on thermal and electrical properties.

In the first part of the thesis, AgNWs were coated onto electrospun 1D PAN yarns, which were prepared at different stretch ratios. This approach revealed a fundamental tripartite challenge governing transport in confined fibrous systems: the interplay between filler anisotropy, matrix architecture dimensionality, and interfacial optimization. While anisotropic fillers like AgNWs hold theoretical potential for directional transport, their practical implementation within the 1D PAN matrix demonstrated how random orientation (inherent to dip-coating) and non-specific surface functionalization critically limit the realization of tailored structure-guided percolation. This established that confined matrix geometries impose distinct constraints on nanofiller alignment strategies effective in higher dimensions.

Subsequently, the work advanced to 2D PS nonwovens, where the degree of polymer fiber orientation was controlled and combined with a dual functionalization strategy. Here, the polymer fibers were either complemented with AgNWs that were aligned within the polymer fiber matrix or with an external copper coating. The results indicated that fiber alignment enhanced directional thermal transport, but optimal performance arose from balancing structural architecture with interfacial contact quality rather than from perfect anisotropy. AgNW functionalized nonwovens exhibited limited thermal improvements due to non-percolating networks and interfacial phonon scattering. In contrast, copper-coated architectures achieved significant conductivity gains through continuous metallic pathways. These findings echoed previous observations from 1D PAN yarns, reinforcing that structural architecture is the dominant factor for the transport performance, independent of dimensionality or nanofiller functionality.

Notably, the copper-coated nonwovens demonstrated that pronounced thermal anisotropy did not necessarily translate to strong electrical anisotropy, highlighting the complex interplay between structural hierarchy and percolation principles.

The thesis culminated in the realization of homogeneously distributed AgNWs within 3D BOS sponges, fabricated from short electrospun fibers using a novel blending approach. This successfully leveraged the unique morphology of BOS fibers and demonstrated a processing-induced self-organization of the conductive nanofiller along the pore walls. Increasing dimensionality and complexity revealed that nanofiller distribution within the volume was a critical factor for designing effective percolation pathways. While the blending approach induced mechanical robustness through the homogeneous AgNW distribution, it faced challenges to establish electrically percolating networks within the thermally insulating 3D sponge structure.

Collectively, this work significantly advanced the understanding of how filler anisotropy, matrix confinement, and interfacial interactions collectively govern transport in fibrous networks across all spatial dimensions. Exploring the coating, aligning, and spacing of nanofillers within tailored architectures yielded fundamental insights into how fillers and the fiber matrix influence each other, and revealed critical design parameters for functional fibrous assemblies and their application in thermal management systems.

Looking ahead, the materials, structures, and dimensionalities explored in this thesis create opportunities for future research. Regarding materials, a deeper investigation into the properties of polymer base materials, such as crystallinity and their impact on percolation at the molecular level, merits further investigation. In terms of structure, new fiber processing and functionalization techniques, including the integration of 3D printing principles into electrospinning - for instance, *via* Near-Field Electrospinning - will enable an enhanced architectural control and unlock the creation of novel fiber morphologies. Additionally, future functionalization approaches should consider the specific demands imposed by the dimensionality of the fiber object. This work has demonstrated how functionalization procedures critically shape the macroscopic properties of fibrous assemblies, underscoring the need for tailored strategies that match the complexity and requirements of each architecture.

5 Experimental part

5.1 Materials and methods

Technical solvents were distilled before further use. All other chemicals were used as received if not stated otherwise.

Table 6: List of used chemicals.

Chemical compound	**Supplier**	**Additional information/ Purity**
4-(Aminomethyl)pyridine	*Fisher Scientific*	98 %, distilled under reduced pressure form CaH_2
Acetone	-	Technical grade
Acryloyl chloride	*Fisher Scientific*	96 %, recondensed under vacuum ($\sim 1 \cdot 10^{-3}$ mbar) at room temperature
Azobisisobutyronitrile	*Sigma Aldrich*	98 %, recrystallized from methanol
Chloroform	*Fisher Scientific*	p.a. ≥ 99.8 %, distilled from CaH_2
Copper(II) sulfate pentahydrate	*Alfa Aesar*	99 %
Dichloromethane	-	Technical grade
Diethyl ether	-	Technical grade
Dimethylformamide	*Fisher Chemical*	p.a. 99.5 %, distilled under reduced pressure from CaH_2
Dimethyl sulfoxide	*Fisher Scientific*	p.a., distilled under reduced pressure from CaH_2
Dioxane	*Fisher Scientific*	p.a., distilled from CaH_2
Ethanol	-	Technical grade
Ethylene glycol	*Fisher Scientific*	p.a. ≥ 99.5 %
Formaldehyde	*Alfa Aesar*	37 wt%, w/w aq. soin. stab. with 7 - 8 % methanol
Iron(III) chloride	*Fisher Chemical*	≥ 97.0 %
Iso-hexane	-	Technical grade
Magnesium sulfate	*Grüssing*	99 %, anhydrous
Methanol	-	Technical grade
Methyl acrylate	*TCI*	> 99 %, recondensed under vacuum ($\sim 1 \cdot 10^{-3}$ mbar) at room temperature

Methyl methacrylate	*TCI*	>99.8 %, recondensed under vacuum (~$1 \cdot 10^{-3}$ mbar) at room temperature
N-hydroxy succinimide	*Roth*	≥ 97.0 %
Poly(4-vinylpyridine)	*Sigma Aldrich*	M_n 160 000
Poly(ε-caprolactone), Capa 6800	*Perstorp*	M_n 155 000
Poly(acrylonitrile), PAN-N	*Dolan*	Copolymer with 6 wt% methyl acrylate
Poly(ethylene glycol) 400	*Sigma Aldrich*	-
Poly(ethyleneimine), branched	*Sigma Aldrich*	M_w ~ 25 000 by LS, M_n ~ 10 000 by GPC
Polystyrene	*Sigma Aldrich*	M_n 119 000
Poly(vinylpyrrolidone)	*Sigma Aldrich*	M_w 1 300 000 by LS
Potassium sodium tartrate tetrahydrate	*Alfa Aesar*	99 %
Pyridine	*Fisher Scientific*	p.a. ≥ 99.5 %
Silver nitrate	*VWR Chemical*	99 - 100.5 % Ph. Eur.
Sodium borohydride	*Fluka*	≥ 96 %
Sodium citrate	*Fisher Chemical*	98 %
Sodium chloride	*Bernd Kraft*	p.a.
Sodium hydrogen carbonate	*Fisher Scientific*	p.a. ≥ 99.7 %
Sodium hydroxide	*Fisher Chemical*	p.a.
Tert-butanol	*Grüssing*	p.a. 99.5 %
Triethylamine	*Grüssing*	99 %, distilled from CaH_2

N-(4-benzoylphenyl)acrylamide (BPAA)[157] and (4-benzoylphenyl)methacrylate (MABP)[158] were previously synthesized accoarding to literature procedures.

In the following methods section, each paragraph is prefaced with a dimensional label (1D, 2D, or 3D) to indicate the corresponding part of the thesis, with multiple assignments if a method is applied across different dimensionalities. Graphical data representations were created using *Origin* (*OriginLab Corp.*), while optical analysis methods were evaluated using *ImageJ* software.

All figures in this thesis were created using the vector graphics software *Inkscape*, while chemical structures were drawn with *ChemDraw Ultra 14.0* (*PerkinElmer Inc.*). *Google NotebookLM* (*Google Labs*) and *Perpexity Pro* (*Perplexity AI Inc.*) were used for literature research and management. The latter was also used to improve the readability of this work. However, all content, analysis, and conclusions were developed independently by the author. *Citavi* (*Lumivero LLC*) was used as reference management software.

Contact angle

1D - Contact angle measurements were conducted using a *Drop Shape Analyzer* equipped with the *Krüss Advance* software (*Krüss GmbH*) at room temperature. The volume of each deionized water drop was 4 µL.

Differential Scanning Calorimetry (DSC)

3D - DSC measurements were performed using a *204 F1 Phoenix* system (*Netzsch-Gerätebau GmbH*). Approximately 5 mg of sample were placed in aluminum crucibles (*THEPRO GbR*) with a pierced lid. These crucibles were exposed to a temperature range from - 50 °C to 200 °C at a heating rate of 10 K/min in a nitrogen atmosphere. Data analysis was carried out using *Proteus 8.0* software.

Elemental analysis

1D - To determine the content of carbon, hydrogen, nitrogen and sulfur (CHNS) in the (un)modified nonwovens an *UNICUBE* elemental analyzer (*Elementar Analysensysteme GmbH*) was used. Prior to analysis, the samples were carefully dried to remove any residual moisture and weighed with an *WXTS3DU* microbalance (*Mettler-Toledo GmbH*). Approximately 2 mg of sample material was used for each measurement. The combustion was conducted in an oxygen-rich atmosphere at temperatures up to 1 200 °C and the resulting gases were quantitatively analyzed to determine the elemental composition. The reported values represent the average of three independent measurements performed at the Inorganic Chemistry II chair.

Energy-dispersive X-ray (EDX) spectroscopy

3D - EDX spectroscopy was conducted at an accelerating voltage of 10 kV using a *Zeiss LEO 1530* scanning electron microscope (*Carl Zeiss Microscopy GmbH*), fitted with a *Thermo Fisher UltraDry* EDX detector (60 mm² active area). This analysis was conducted by Martina Heider and Dr. Ulrich Mansfeld (Bayerisches Polymerinstitut, KeyLab Electron and Optical Microscopy).

Four-Point Probe (4PP)

2D - Electrical conductivity within the copper-coated 2D nonwovens was determined by Alexander Berger and Ina Klein (Physical Chemistry I, Prof. Dr. Markus Retsch) using a custom-made set-up. The system employs four spring-loaded pin electrodes with spherical rhodium-coated gold tips (0.42 mm diameter, *NP58-N*, *MISUMI Europa GmbH*), arranged at 1 mm spacing. These are mounted on a 3D printed holder equipped with a *Series-4* force sensor (*MARK-10 Corp.*) to control the contact pressure. Measurements were conducted in constant current and auto mode using a *Keithley 2400* source meter (*Keithley Instruments Corp.*), applying a contact force between 0.34 N and 0.44 N. For each coated nonwoven, three measurements of the electrical resistance were performed at different positions, with each measurement consisting of 500 data points. The effective side lengths of the samples were estimated by taking the square roots of their respective areas. Based on these side lengths, correction factors were determined through interpolation of literature values.[159] These correction factors were then used to calculate the electrical sheet conductance. To obtain the electrical conductivity σ, the sheet conductance was multiplied by the sample thickness (for values see Section LEXT). For the random sample, the measured thickness was used directly, whereas for the oriented sample, the thickness was divided by three before multiplication to account for the partial copper coating.

3D - Electrical conductivity within the functionalized 3D sponges was determined using a *Keithley 2420* source meter (*Keithley Instruments Corp.*) in combination with custom-made molds featuring two parallel copper plates (1 mm thickness) for clamping the sponges in between. The conductivity was calculated based on the following Equation 5:

$$\sigma = \frac{l}{R \cdot A} \tag{5}$$

σ: electrical conductivity, l: height of the sponge equal to the distance between the contact points (1.3 cm), R: electrical resistivity, A: cross-sectional area of the sponge (2.01 cm^2).

FOURIER Transform Infrared Spectroscopy (FT-IR)

1D, **3D** - FT-IR spectra were recorded with a *Spectrum Two* spectrometer (*PerkinElmer Inc.*) equipped with an Attenuated Total Reflection (ATR) accessory. In the case of 1D yarns, optical transmission was analyzed, whereas for the fiber components used in 3D sponges, absorption measurements were conducted. Measurements were carried out over a spectral range of 4000 cm^{-1} to 650 cm^{-1}. A background subtraction was applied to all recorded spectra.

Gel Permeation Chromatography (GPC)

1D, **2D**, **3D** - The molecular weights of all commercial base polymers (PAN, PEI, PS, PCL), as well as the copolymers synthesized for the 3D sponges were determined using a *1200 series* GPC system with a refractive index detector (*Agilent Technologies Inc.*). Depending on the solubility of the polymers, three different solvent systems were employed, each with distinct column configurations and calibration standards (*PSS Polymer Standards Service GmbH*). For PAN and PEI, measurements were performed in DMF containing 5 g/L LiBr using two *GRAM* columns (10 µm particle size, 100 - 3 000 Å porosity). PS and PCL were analyzed in chloroform with a *SDV* precolumn and a *SDV linear XL* column (5 µm particle size), while the copolymers were measured in HFIP containing potassium trifluoroacetate (4.8 g/600 mL HFIP) using two *PFG linear M* columns (7 µm particle size, 100 - 300 Å). All analyses were conducted by Rika Schneider (Macromolecular Chemistry II) at a flow rate of 0.5 mL/min. Calibration was performed with narrowly dispersed PS standards for DMF and chloroform, and with PMMA standards for HFIP. Prior to injection, all samples were filtered through a 0.22 µm PTFE filter. Toluene (HPLC grade, *Sigma Aldrich*) served as an internal standard, with an injection volume of 20 µL. All columns were maintained at room temperature. Reported molar masses are relative to respective standards.

High-speed camera

2D - Images of the stable PS fiber jet were taken by using a *CR5000X2* Ultra Highspeed camera (*Optronis GmbH*), equipped with a *24-70mm f/2,8 EX DG* lens (*Sigma Corp.*).

Inductively Coupled Plasma Optical Emission Spectroscopy (ICP-OES)

1D, **2D**, **3D** - The silver content in both the AgNW suspensions and the AgNW functionalized composite 2D nonwovens and 3D sponges was quantified in cooperation with Simon Knorr (Macromolecular Chemistry II) using an *Avio 200* system (*PerkinElmer Inc.*), equipped with a *S10* autosampler, echelle polychromator, argon nebulizer, and CCD semiconductor detector. Calibration was carried out using a single-element silver standard solution (1000 µg/mL, *PerkinElmer Inc.*). For sample preparation, 0.1 mL of the AgNW suspension or 20 mg of the corresponding nonwoven or sponge were each dissolved in 5 mL of nitric acid. The resulting solutions were transferred into glass inserts placed within Teflon digestion vessels and subjected to microwave-assisted digestion in a *Multiwave GO* (*Anton Paar Germany GmbH*) using two 15-minute cycles at 185 °C. After digestion, the samples were diluted to a final volume of 100 mL with deionized water (*Millipore Milli-Q Plus* system, *QPAK*2* purification cartridge).

For the determination of the volume fraction of silver within 3D sponges, the following equation was used:

$$vol\%\ (Ag) = \frac{V_{Ag}}{V_{sponge}} = \frac{\frac{m_{Ag}}{\rho_{Ag}}}{V_{Ag} + \frac{m_{sponge}}{\rho_{bulk}}} \quad (6)$$

V_{Ag}: volume fraction of silver, V_{sponge}: volume fraction of the sponge, m_{Ag}: mass of silver fraction, ρ_{Ag}: density of silver (10.49 g/cm^3),[160] m_{sponge}: mass of the sponge fraction, ρ_{bulk}: density of the bulk was equated with the density of PAN (1.16 g/cm^3).[149]

Laser Scanning Confocal Microscope (LEXT)

2D - Microscopy images and surface topographies were acquired using a LEXT OLS5000 (*Olympus Corp.*) operated in reflection mode with both a white light source and a 405 nm laser. To assess the orientation parameters S_{2D}, ten overexposed images were converted to grayscale and analyzed using the *MountainsLab* software (*Digital Surf*) to extract orientation, diameter, and length of individual fiber segments (see Chapter 7, Figure 65). To standardize orientation, the images were rotated by adjusting all segment angles such that their mean orientation aligned with 0°. The adjusted angles, ranging between -90° and 90°, were then used to compute the S_{2D} parameters according to Equation 7 and Equation 8. To determine the electrical conductivity of the copper-coated samples, the area and thickness were measured using the confocal microscope's data analysis software (*Olympus Corp.*). For the random sample, these values were 166.7 mm² and 109.1 µm, respectively, while for the oriented sample, the area was also 166.7 mm² and the thickness was 102.0 µm.

$$S_{2D} = 2\left[\sum_{i=1}^{N} \cos^2(\alpha_i - \bar{\alpha})\ \omega_i\right] - 1 \quad (7)$$

S_{2D}: orientation parameter, α_i: orientation angles, ω_i: fiber segment weighing factor.

$$\omega_i = \frac{l_i\ d_i}{\sum_{k=1}^{N} l_k\ d_k} \quad (8)$$

ω_i: fiber segment weighing factor, l_i: segment length, d_i: segment diameter.

The area and thickness of the copper-coated samples were measured with the data analysis software associated with the confocal microscope (*Olympus Corp.*), yielding 166.7 mm^2 and 109.1 µm for the random nonwoven, and 166.7 mm^2 and 102.0 µm for the oriented nonwoven. These dimensions served as the basis for subsequent electrical conductivity calculations (see Section 4PP). This analysis was done by Ina Klein (Physical Chemistry I, Prof. Dr. Markus Retsch).

Lock-In Thermography (LIT)

All measurements were conducted by Ina Klein (Physical Chemistry I, Prof. Dr. Markus Retsch).

1D - The PAN yarns were coated with a thin layer of carbon on both sides (PAN yarns both sides: 11 nm; AgNW functionalized yarns side facing laser: 11 nm, side facing camera: 45 nm - 48 nm) with a *EM ACE600* carbon thread coater (*Leica Microsystems GmbH*). The PAN and AgNW functionalized PAN yarns were excited periodically with a frequency of 0.3 Hz and 0.9 Hz, respectively using a *51nano-N520-0.9-O05-P-12-4-28-0-150*-point laser (*Schäfter + Kirchhoff GmbH*) delivering power between 0.037 mW - 0.090 mW. The thermal response was recorded using an *ImageIR 9430* infrared camera (*InfraTec GmbH*), operating in the 1.5 - 5.5 µm spectral range with a 8.0 x magnification lens. All measurements were performed under vacuum ($< 10^{-5}$ bar) inside a chamber equipped with an *N-BK7* glass window to suppress convective heat losses. The time-temperature data were converted to an amplitude and phase signal *via* the software *IRBIS* by *InfraTec GmbH*. Depending on the sample type, the linearized phase data or the linearized phase and amplitude data as a function of the distance from the excitation point of the laser were used to calculate the thermal diffusivity values (slope method).

2D - LIT measurements were conducted on 2D nonwovens that were coated on both sides with a thin carbon layer (10 - 40 nm) to increase their surface emissivity. A *51nano-N520-0.9-O05-P-12-4-28-0-150*-point laser (*Schäfter + Kirchhoff GmbH*) delivering up to 0.9 mW was used to apply periodic thermal excitation. Depending on the sample type and its thermal penetration depth, different excitation frequencies were selected: 0.18 Hz for pressed and annealed samples, 0.3 Hz for silver-nanowire-functionalized samples, 1.0 Hz for copper-coated nonwovens, and 0.1 Hz for homogeneous pressed PS thin films. All other conditions were kept identical to the analysis of 1D yarns, except for a 1.0 x magnification lens of the infrared camera. Thermal diffusivity was then determined in a manner similar to that used for the 1D PAN yarns. But for the 2D nonwovens, both amplitude and phase data were consistently utilized for the calculation.

Microscope

3D - Optical images of the bead-on-string fibers were obtained by a *SmartZoom 5* digital microscope (*Carl Zeiss Meditec AG*), equipped with a *PlanApo D 5x/0.3 FWD 30 mm* and *PlanApo D 1.6x/0.1 FWD 36 mm* lens (*Carl Zeiss Meditec AG*).

Modified Transient Plane Source (MTPS)

3D - Thermal conductivity measurements were conducted by Ina Klein (Physical Chemistry I, Prof. Dr. Markus Retsch) using a *Trident Thermal Conductivity Analyzer* and the corresponding software (*C-Therm Technologies Ltd.*), in accordance with ASTM D7984. Each sample was tested under a compressive load corresponding to the pressure previously determined to achieve 10 % or 50 % compression of the sample thickness. The reported thermal conductivity values represent the average of five performed measurements per sample with an inaccuracy of 5 %.

Nuclear Magnetic Resonance (NMR)

3D - ^{1}H-NMR spectra were acquired by Marius Schmidt (Macromolecular Chemistry II, Prof. Dr. Andreas Greiner) on an *UltraShield* spectrometer (*Bruker Corp.*) operating at 300 MHz. Chemical shifts (δ) were referenced to the residual proton signal of the solvent $CDCl_3$ at δ (1H) = 7.26 ppm respectively DMSO-d_6 at δ (1H) = 2.50 ppm. Data analysis was performed using the *MestreNova* software (*Mestrelab Research*).

To determine the weight fractions *w* of the bead and string components in the BOS fibers, the calculation began with the determination of the molar fractions *x* in of the individual monomers within the two copolymers (and the additional PAN component), following the method described by SCHMIDT et al.[140] Based on these molar fractions, the weight fraction for each monomer within its copolymer was calculated using the following equation:

$$w_i = \frac{x_i \cdot M_i}{\sum_k x_k \cdot M_k} \tag{9}$$

w: weight fraction, *x*: molar fraction, *M*: Molar mass.

Subsequently, the individual weight contributions of each fiber component (bead and string) to the nonwoven were summed according to the following expressions:

$$w_{string} = \frac{\sum w_{string}}{\sum w_{string} + \sum w_{bead}} \tag{10}$$

$$w_{bead} = \frac{\sum w_{bead}}{\sum w_{string} + \sum w_{bead}} \tag{11}$$

w_{string}: weight fraction of the string components, w_{bead}: weight fraction of the bead components.

Potentiostat

1D - The electrical behavior of the functionalized 1D yarns was examined by applying a constant voltage of 3 V using a potentiostat/galvanostat *Interface 1010E* device (*Gamry Instruments Inc.*), while monitoring the resulting current flow through the nanofiber yarns.

RAMAN Spectroscopy

All measurements were conducted by Dr. Holger Schmalz (Macromolecular Chemistry II).

2D - Polarized RAMAN spectroscopy was carried out using a confocal *WITec Alpha RA+* Raman imaging system, featuring a *UHTS 300* spectrometer and a back-illuminated *Andor Newton 970 EMCCD* detector (*Suite SEVEN 7.0*, *WITec GmbH*). Spectra were acquired at an excitation wavelength of 532 nm using a 50 x long working distance objective (*LD EC Epiplan-Neofluar DIC*, *Zeiss AG*, NA = 0.55), with a laser intensity of 12 mW, an integration time of 0.5 s, and 50 accumulations. A background subtraction was applied to all recorded spectra.

3D - The same set-up was used again for analyzing the bead-on-string fibers. Measurements were performed using an excitation wavelength of 532 nm using a 100 x long working distance objective (NA = 0.9), with a laser intensity of 20 mW together with an integration time of 0.5 s and 100 accumulations. A background subtraction was applied to all recorded spectra. The spatial distribution of both P(PMAA-*co*-BPAA) and P(MA-*co*-MMA-*co*-MABP) + PAN within the fibers was analyzed using the "*True Component Analysis*" feature of the *WITec Project SIX* software (version 6.1). For RAMAN imaging, the fibers were electrospun directly onto glass slides.

Scanning Electron Microscopy (SEM)

1D, **2D**, **3D** - SEM characterization was carried out using a *FEI Quanta FEG 250* (*Thermo Fisher Scientific Inc.*) at 3 respectively 10 kV accelerating voltage. In addition to an ETD (SE) detector, a CBS detector (BSE) was employed to visualize the metallic functionalization. Prior to imaging, samples were fixed on conductive carbon tape, mounted on aluminum stubs and coated with a ~ 1.6 nm platinum layer using a *208HR* sputter coater (*Cressington Ltd.*).

1D - To assess the orientation parameters S_{2D} for the fibers within 1D yarns, SEM images were analyzed using the *MountainsLab* software (*Digital Surf*) to extract orientation, diameter, and length of individual fiber segments (see Chapter 7, Figure 61). Equation 7 was used again to determine the S_{2D} parameters for each type of yarn, but here no rotation of the images was done because of the spatial expansion in only one dimension. Since per sample only one image was available, there was also no standard deviation determinable.

Tensile testing

1D - Tensile tests on 1D yarns were performed on a *BT1-FR0.5TN.D14* system (*ZwickRoell GmbH & Co. KG*) equipped with a clamping unit (25 mm distance), a test speed of 5 mm/min at room temperature and a pre-tension of 0.005 N. A 20 N load cell (*ZwickRoell GmbH & Co. KG*) was used for all measurements. The yarns were fixed to paper frames (4.2 x 1.9 cm, 0.5 cm frame width) using adhesive glue, ensuring that they remained straight. This set-up allowed for stress-free mounting in the clamping unit of the testing device; once secured, the lateral sides of the frame were cut to enable mechanical characterization of the free-standing yarns. During the test, an uniaxial tension was applied on the yarns. For each yarn type, five individual measurements were conducted. From these, three representative values were selected for each type to calculate the mean value and standard deviation. These calculations also incorporated the linear density (tex) of the yarns (see Chapter 5.3.1 and 5.3.3).

3D - Compression tests of 3D sponges were conducted on the same testing system equipped with two parallel plates connected to a 20 N load cell (*ZwickRoell GmbH & Co. KG*). The sponge samples were positioned to ensure full contact between the top and bottom plates. Subsequently, a 50 % compression was applied at a testing speed of 30 mm/min. This procedure was repeated over 100 compression cycles. For each sponge type, at least two individual samples were tested by Marius Schmidt (Macromolecular Chemistry II, Prof. Dr. Andreas Greiner) to calculate average values and standard deviations. For determination of the mechanical parameters, the *testXpert* software (*ZwickRoell GmbH & Co. KG*) was used.

Thermogravimetric analysis (TGA)

3D - Thermogravimetric measurements were performed using a *TG 209F1 Libra* thermo-balance (*Netzsch-Gerätebau GmbH*). Approximately 5 mg of sample were placed in aluminum crucibles (*THEPRO GbR*) with a pierced lid and heated from 20 °C to 600 °C at a constant rate of 10 K/min under nitrogen atmosphere. Data analysis was carried out using *Proteus 8.0* software.

Ultraviolet-visible spectroscopy (UV-Vis)

1D - UV-VIS spectra were recorded with a *JASCO V-630* double beam UV-visible spectrophotometer *(JASCO Corp.*) using quartz glass cuvettes. A background subtraction was applied to all recorded absorbance spectra.

X-ray diffraction (XRD)

1D - X-ray diffraction measurements were performed by Patrick Länger (Inorganic Chemistry III, Prof. Dr. Jürgen Senker) with a *PANalytical XPert Pro* (*Malvern Panalytical Ltd.*), set to 40 kV and 40 mA, utilizing Cu-Kα radiation with a wavelength of 0.154 nm. Before analysis, the yarns were wrapped around the glass capillary. The patterns were captured in a reflection geometry across a 2θ angle range of 2 to 60° at room temperature.

5.2 Silver nanowires

AgNWs were used in all three parts of the thesis. While different batches were employed in each chapter, the synthesis protocol remained consistent. The nanowires were synthesized adapting a polyol process that has been previously published.[121]

160.00 mL ethylene glycol were heated to 130 °C overnight under magnetic stirring at 500 rpm. Subsequently, 0.20 mL of a NaCl solution (0.0199 g/mL), 0.10 mL of a $FeCl_3$ solution (0.0054 g/mL), 20.76 mL of a PVP (M_w 1 300 000) solution (0.0420 g/mL), and 20.76 mL of a $AgNO_3$ solution (0.0420 g/mL) all solved in ethylene glycol were sequentially added to the preheated ethylene glycol. The reaction was maintained at 130 °C for 6 h. Afterwards, the mixture was cooled to room temperature, and AgNWs were precipitated by adding approximately 600 mL acetone. The resulting product was separated from excess ligand by centrifugation at 1000 rpm for 10 min (*Megafuge 16R*, *Fisher Scientific GmbH*) followed by decanting the supernatant. Finally, the AgNWs were redispersed in deionized water to obtain suspensions of varying concentrations (see Chapter 7 Figure 64).

The following table gives an overview of the different AgNW batches and the reached concentrations.

Table 7: AgNW batches with their corresponding silver content as well as the reached diameter and length.

Batch	Ag content [wt%][a]	Diameter [nm][b]	Length [µm][b]
$AgNW_{1D}$	0.9	200	3 - 34
$AgNW_{2D}$	2.2	100	5 - 23
$AgNW_{3D}$	1.9	125	11 - 41

[a] determined from ICP-OES, [b] determined from SEM images.

5.3 1D yarns

5.3.1 Yarn preparation

1) Preparation of solution

2.0 g PAN (Orlon, M_n 80 000) were solved in 11.4 mL DMF and stirred at room temperature overnight at 300 rpm.

2) Electrospinning in a custom-made set-up (with funnel device and winding collector)

The solution was filled in two 6 mL syringes which were then further equipped with 0.8 mm blunt-ended cannulas. These syringes were fixed opposite to each other in the set-up, with the fiber-collecting funnel device (8 cm diameter) and the winder collector (2 cm diameter) in between (see Chapter 3.1.1, Figure 16a). During spinning, a temperature of 21 °C and a humidity level of 38 % were measured. The spinning time was fixed at 90 min. The following table gives an overview of the other process parameters. All yarns were wrapped around 20 mL syringes (*B. Braun SE*) and were further named 'as spun'.

Table 8: Overview of the process parameters applied for Yarn Electrospinning using the funnel device together with the winding collector.

Voltage [kV]	Voltage [kV]	Feed rate [mL/h]	Winding motor speed [rpm]	Funnel motor speed [rpm]	Needle-funnel distance [cm]	Ground-winding motor distance [cm]	Ground-funnel edge distance [cm]
+ 12	- 12	0.5	12	1 200	12.5	59	48

3) Heat stretching (with tube oven and two roller motors)

The 1D PAN yarn-loaded syringe (as spun) was mounted on the right winding motor and the yarn was fed through the tube oven (*RE 1.1 RO 4/25 1100°C*, *Heraeus Holding GmbH*) and fixed on the left side of the set-up around a second 20 mL syringe (see Chapter 3.1.1, Figure 16b). The temperature in the middle of the oven was fixed at 150 - 160 °C. The following table gives an overview of the used winding motor speeds, that were controlled with the *LV2016* software, to create different stretch ratios. The latter also specify their further designation in the discussion.

Table 9: Overview of the process parameters applied for yarn Heat Stretching using the stretching device and tube oven in combination with the resulting linear densities.

Stretch ratio	**Winding motor speed [mm/s]**		**Linear density [tex][a]**
As spun	-		1.38
Annealed	Left: 4	Right: 4	1.92
x2	Left: 8	Right: 4	0.38
x3	Left: 12	Right: 4	0.30

[a] determined from weighing each yarn with a constant length of 30 cm.

5.3.2 Nonwoven preparation

1) Preparation of solution

2.0 g PAN (M_n 80 000) were solved in 11.4 mL DMF and stirred at room temperature overnight at 300 rpm.

2) Electrospinning in a custom-made set-up (with high-speed collector)

The solution was filled in a 6 mL syringe and was then further equipped with a 0.8 mm blunt-ended cannula. During spinning, a temperature of 21 °C and a humidity level of 32 % were measured. The spinning time was fixed at 2 h. All fibers were collected on baking paper that was mounted on the rotating drum collector (15 cm diameter) with the syringe fixed above. The following table gives an overview of the other process parameters.

Table 10: Overview of the process parameters applied for 2D nonwoven electrospinning using the high-speed collector.

Feed rate [mL/h]	**Voltage [kV]**	**Voltage [kV]**	**Collector speed [rpm]**	**Needle-collector distance [cm]**
0.5	+ 12	- 1	60	15

5.3.3 Yarn modification

The grafting of *b*-PEI on the 1D PAN yarn surface was adapted from a literature known approach.[113]

65 cm of each yarn type were put in 100 mL of a PEI (M_n 10 000) solution (0.01 g/mL) in ethylene glycol and were refluxed at 140 °C for 4 h. The yarns were wrapped around a 3D printed PEEK frame (1.8 x 3 cm, 0.3 cm frame width). This frame was placed in the flask being held in place by a Teflon ribbon (see Chapter 7, Figure 63). After the reaction, the yarns were filtered, washed several times with deionized water and ethanol and were dried overnight at 60 °C in vacuum.

Table 11: Overview of the linear densities for modified 1D yarns.

Strech ratio	Linear density [tex][a]
As spun	1.59
Annealed	1.96
x2	0.43
x3	0.41

[a] determined from weighing each yarn with a constant length of 30 cm.

5.3.4 Nonwoven modification

The grafting of *b*-PEI on the 2D PAN nonwoven surface was adapted from a literature known approach.[113]

30 mg of nonwoven were put in 100 mL of a PEI (M_n 10 000) solution (0.01 g/mL) in ethylene glycol and were refluxed at 140 °C for 4 h. The nonwoven was wrapped around a 3D printed PEEK frame (1.8 x 3 cm, 0.3 cm frame width). This frame was placed in the flask being held in place by a Teflon ribbon similar to the procedure in Chapter 5.3.3. After the reaction, the nonwoven was filtered, washed several times with deionized water and ethanol and was dried overnight at 60 °C in vacuum.

5.3.5 Yarn functionalization

1) Functionalization with silver nanowires

30 cm of each PEI modified 1D PAN yarn was individually immersed in 2.0 mL of an aqueous 0.9 wt% AgNW suspension ($AgNW_{1D}$). After this, the solutions were degassed twice at 1 mbar until the solutions began to boil. The loaded solutions were shaken for 24 h at 300 rpm in a shaker *(Multi Reax*, *Heidolph Instruments GmbH & Co. KG*). Subsequently, they were washed with deionized water and dried for 5 h at 60 °C in vacuum.

2) Leaching test

2 cm of the as spun AgNW functionalized 1D PAN yarn was placed in 5 mL deionized water and was shaken for 24 h at 500 rpm. This solution is analyzed *via* UV-Vis spectroscopy together with a positive control (0.5 mL of $AgNW_{1D}$ diluted with deionized water to a final dilution of 1:100).

5.4 2D nonwovens

5.4.1 Nonwovens with different degrees of orientation

5.4.1.1 Film preparation

The homogeneous 2D PS film was fabricated by hot pressing using a 100 µm thick mold. PS (M_n 119 000) was evenly spread within the mold and melted for 3 min at 220 °C in a hot press (*2518 Mod. 25-12-2 HC*, *Carver, Inc.*). Subsequently, a pressure of 2 t was applied for 2 min. To finalize the process, the film was transferred to a separate press (*PO Weber GmbH*) and compressed until it cooled to room temperature.

5.4.1.2 Nonwoven preparation

5.4.1.2.1 Random and oriented nonwoven preparation

1) Preparation of solution

1.5 g PS (M_n 119 000) were solved in 3.88 mL DMF and stirred at room temperature overnight at 300 rpm.

2) Electrospinning in a custom-made set-up (with high-speed collector)

The solution was filled in a 6 mL syringe and was then further equipped with a 0.8 mm blunt-ended cannula. During spinning, a temperature of 21 °C and a humidity level of 39 % were measured. The spinning time was fixed at 2 h. All fibers were collected on PET-mesh (100 µm mesh size) that was mounted on the rotating drum collector (5 cm diameter) with the syringe fixed on the right of the collector. Additionally, a back electrode in form of an empty syringe was fixed left to the drum collector (see Chapter 3.2.1, Figure 33a). The following table gives an overview of the other process parameters.

Table 12: Overview of the process parameters applied for random and oriented 2D nonwoven electrospinning using the high-speed collector.

Feed rate [mL/h]	**Voltage [kV]**	**Voltage [kV]**	**Collector speed [rpm]**		**Needle-collector distance [cm]**	
			Random	Oriented	Left	Right
0.6	+ 22	- 3	30	3 000	11	24

Afterwards, the nonwoven mats were divided into two sets: one set was compression molded using a hot press (*2518 Mod. 25-12-2 HC*, *Carver, Inc.*) at 2 t for 1 min, while the other set underwent thermal annealing.

For this purpose, the samples were heated to 115 °C over 11 min in an oven (*Heratherm OGS60*, *Thermo Scientific GmbH*) and held at that temperature for either 3 or 24 h. Cooling was carried out over 55 min until the temperature dropped below 80 °C before the samples were removed from the oven. This thermal treatment was done by Ina Klein (Physical Chemistry I, Prof. Dr. Markus Retsch).

5.4.1.2.2 SJES nonwoven preparation

1) Preparation of solution

1.5 g PS (M_n 119 000) were solved in 3.88 mL DMF and stirred at room temperature overnight at 300 rpm.

2) Electrospinning in a custom-made set-up (with high-speed collector)

The solution was filled in a 6 mL syringe and was then further equipped with a 0.8 mm blunt-ended cannula. During spinning, a temperature of 22 °C and a humidity level of 19 % were measured. The spinning time was fixed at 1 h. All fibers were collected on PET-mesh (100 µm mesh size) that was mounted on the rotating drum collector (5 cm diameter) with the syringe fixed above (see Chapter 3.2.1, Figure 33b). The following table gives an overview of the other process parameters.

Table 13: Overview of the process parameters applied for SJES 2D nonwoven electrospinning using the high-speed collector.

Feed rate [mL/h]	Voltage [kV]	Collector speed [rpm]	Needle-collector distance [cm]
0.9	+ 18	3 000	15

Post-processing treatment was conducted analogous to Chapter 5.4.1.2.1.

5.4.1.3 Nonwoven functionalization

Both types of 2D nonwoven functionalization were applied to the random and oriented nonwoven orientation only.

5.4.1.3.1 AgNW functionalization

The AgNW functionalization of 2D PS nonwoven was adapted from a literature known approach.[133]

1) Preparation of solution

2.0 mL of an aqueous 2.2 wt% AgNW suspension ($AgNW_{2D}$) were freeze-dried (- 109 °C, 0.005 mbar, 24 h, *Alpha 3-4 LSCbasic*, *Martin Christ Gefriertrocknungsanlagen GmbH*), and the resulting solid was redispersed in 3.88 mL DMF.

This mixture was placed in an ultrasonic bath for 5 min to support dispersion. Subsequently, 1.5 g of PS (M_n 119 000) were added, and the mixture was homogenized overnight using a shaker. Prior to further processing, the solution was stirred at room temperature for 1 h at 300 rpm.

2) Electrospinning in a custom-made set-up (with high-speed collector)

The solution was filled in a 6 mL syringe and was then further equipped with a 0.8 mm blunt-ended cannula. During spinning, a temperature of 21 °C and a humidity level of 39 % were measured. The spinning time was fixed at 2 h. All fibers were collected on PET-mesh (100 µm mesh size) that was mounted on the rotating drum collector (5 cm diameter) with the syringe fixed on the right of the collector. Additionally, a back electrode in form of an empty syringe was fixed left to the drum collector (see Chapter 3.2.1, Figure 33a). The following table gives an overview of the other process parameters.

Table 14: Overview of the process parameters applied for AgNW functionalized random and oriented 2D nonwoven electrospinning using the high-speed collector.

Feed rate [mL/h]	**Voltage [kV]**	**Voltage [kV]**	**Collector speed [rpm]**		**Needle-collector distance [cm]**	
			Random	Oriented	Left	Right
0.6	+ 22	- 3	30	3 000	11	24

Afterwards, the functionalized nonwoven mats were compression molded at 2 t for 1 min.

5.4.1.3.2 Cu functionalization

The Cu functionalization of 2D PS nonwoven was adapted from a previously published approach.[56]

Sections of pressed, neat PS nonwoven (3 x 4 cm) were mounted between two PP frame parts, which were sealed together using heat. These framed samples were then immersed in 90 mL of a P4VP solution (6.6 mg/mL) in methanol in a custom-made Teflon reaction container (see Chapter 7, Figure 68b), and stirred for 5 min. After briefly draining off excess liquid, the samples were dried overnight at 80 °C in vacuum.

The dried, P4VP-coated nonwovens were subsequently immersed in 90 mL of a $0.2 \cdot 10^{-3}$ M AgNP suspension. To prepare this suspension, 42 mg (0.247 mmol) of $AgNO_3$ and 65 mg (0.252 mmol) of sodium citrate were dissolved in 1000 mL of deionized water. Then, 0.55 mg (0.015 mmol) of $NaBH_4$ dissolved in 3 mL water was added to the solution. The nonwoven-loaded suspension was degassed twice at 1 mbar until boiling commenced.

The samples remained in the AgNP suspension for 24 h under gentle shaking (60 rpm), followed by rinsing with deionized water.

For copper deposition, the nonwovens were immersed in 90 mL of freshly prepared metallization solution. To prepare this, 1.0 g (4 mmol) of $CuSO_4 \cdot 5\ H_2O$ was dissolved in 40 mL of deionized water, followed by the addition of 2.5 g (8.8 mmol) potassium sodium tartrate tetrahydrate. Then, 1.5 g (24.8 mmol) NaOH, 0.2 g (4.54 mmol) PEG 400, 6.1 µL pyridine, and 3.0 mL formaldehyde were added. The solution was filled up to 100 mL. The reaction container holding the nonwoven samples was placed in a 45 °C water bath and stirred gently for 30 min. Finally, the samples were rinsed with water, pre-dried on filter paper, and dried overnight at 80 °C in vacuum.

5.4.2 Grid nonwovens

1) Preparation of solution

3.0 g PCL (M_n 155 000) were solved in 9.34 mL chloroform and 3.10 mL DMF and stirred at room temperature overnight at 300 rpm.

2) Electrospinning in a custom-made set-up (with high-speed collector)

The solution was filled in a 6 mL syringe and was then further equipped with a 0.8 mm blunt-ended cannula. During spinning, a temperature of 22 °C and a humidity level of 40 - 50 % were measured. The spinning time was fixed at 90 min. All fibers were collected on baking paper that was layered with a stainless-steel metal grid on top (1.2 mm mesh size). Both were mounted on the rotating drum collector (15 cm diameter) with the syringe fixed above. The following table gives an overview of the other process parameters.

Table 15: Overview of the process parameters applied for 2D grid nonwoven electrospinning using the high-speed collector.

Feed rate [mL/h]	Voltage [kV]	Voltage [kV]	Collector speed [rpm]	Needle-collector distance [cm]
0.6	+ 18	- 1	60	17

Afterwards, the grid nonwoven mats were compression molded at 2 t for 1 min.

5.5 3D sponges

The synthesis of monomers, polymers and the processing *via* Side-by-Side Electrospinning, the analysis as well as the fabrication of neat string, bead and bead-on-string fiber sponges was conducted by Marius Schmidt (Macromolecular Chemistry II, Prof. Dr. Andreas Greiner).

All monomer and polymer syntheses were performed under an argon atmosphere.

5.5.1 Monomer synthesis

5.5.1.1 *N*-Succinimidyl acrylate (NAS)

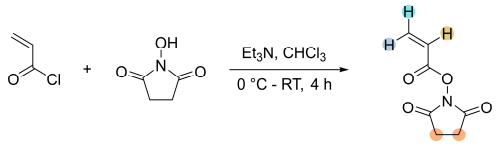

The synthesis of NAS was adapted from a literature known approach.[161]

300.0 mL of chloroform and 26.2 g of *N*-hydroxy succinimide (115.09 g/mol, 228 mmol, 1.00 eq.) were added to a flame-dried Schlenk flask. The reaction mixture was cooled to 0 °C, after which 31.6 mL of triethylamine (101.19 g/mol, 228 mmol, 1.00 eq.) was introduced. Over the course of 30 min, 20.4 mL of acryloyl chloride (90.51 g/mol, 251 mmol, 1.10 eq.), dissolved in 20.0 mL of chloroform, were added dropwise. The mixture was stirred for 4 h while gradually allowing it to reach room temperature. The organic layer was washed with 260 mL of deionized water, followed by three washing steps with 230 mL of saturated sodium hydrogen carbonate solution, and three additional washing steps with 260 mL of deionized water. The organic phase was dried over magnesium sulfate and filtered. The solvent was removed under reduced pressure at 30 °C to a final volume of approximately 50 mL, after which 150 mL of iso-hexane was added. The mixture was placed in a refrigerator at - 26 °C overnight to promote crystallization. The resulting white solid was collected by filtration and washed three times with iso-hexane. The product was dried under reduced pressure at room temperature for 10 h and stored under argon at - 26 °C until further use. The ^{1}H-NMR spectrum is shown in Chapter 7, Figure 70a.

Yield: 30.7 g (80 %).

^{1}H-NMR(300 MHz, $CDCl_3$) δ = 6.75 - 6.70 (1H, ●, dd), 6.39 - 6.30 (1H, ●, dd), 6.21 - 6.17 (1H, ●, dd), 2.88 (4H, ●, s) ppm.

5.5.2 Polymer synthesis

5.5.2.1 Poly(*N*-succinimidyl acrylate-*co*-*N*-(4-benzoylphenyl)acrylamide) P(NAS-*co*-BPAA)

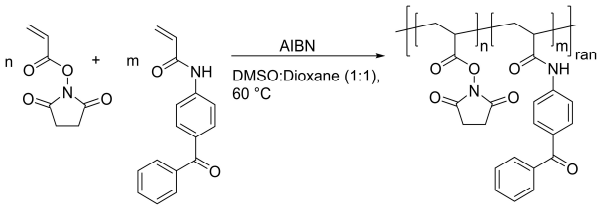

25.3 g of NAS (150 mmol, 0.95 eq.) and 2.0 g of BPAA (8 mmol, 0.05 eq.) were placed in a flame-dried Schlenk flask and dissolved in 52.0 mL of a 1:1 (v/v) mixture of DMSO and dioxane. The solution was purged with argon for 45 min. In a separate Schlenk flask, 0.052 g of AIBN (0.3 mmol, 0.002 eq. relative to the total monomer content) was dissolved in 5.2 mL of the same DMSO:dioxane solvent mixture and degassed under argon. The monomer solution was heated to 60 °C. Once the target temperature was reached, the AIBN solution was added. After 5 h of reaction time, the mixture was slowly cooled in an ice bath and subsequently exposed to air. The resulting product was precipitated in a large excess of acetone, filtered, and dried under reduced pressure at 40 °C, yielding P(NAS-*co*-BPAA), a slightly yellow powder with a monomer ratio of 95:5. The ^{1}H-NMR spectrum is shown in Chapter 7, Figure 70b.

Yield: 26.0 g (95 %)

5.5.2.2 Poly(*N*-(pyridin-4-ylmethyl)acrylamide-*co*-*N*-(4-benzoylphenyl)acrylamide) P(PMAA-*co*-BPAA)

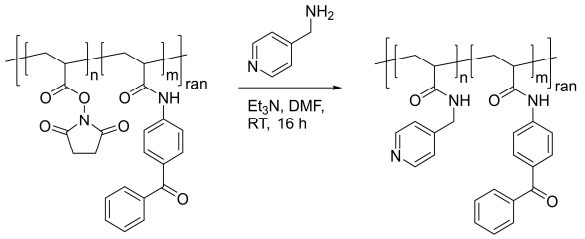

A total of 26.0 g of P(NAS-*co*-BPAA), containing 143.0 mmol of NAS units, were added to a flame-dried Schlenk flask and dissolved in 250.0 mL of DMF. Next, 39.7 mL of triethylamine (285.0 mmol, 2.00 eq. relative to NAS) and 28.8 mL of 4-(aminomethyl) pyridine (285.3 mmol, 2.00 eq. relative to NAS) were added. The reaction mixture was stirred at room temperature for 16 h. Upon completion, the volatile components were removed under reduced pressure at room temperature.

The polymer was then redissolved in ethanol and dialyzed against ethanol for 72 h, with the solvent being replaced twice per day. Finally, the product was precipitated in diethyl ether and dried under reduced pressure at 40 °C, yielding a yellow powder of P(PMAA-*co*-BPAA). The ^{1}H-NMR spectrum is shown in Chapter 3.3.1, Figure 47d.

Yield: 22.1 g (92 %)

5.5.2.3 Poly(methyl acrylate-*co*-methyl methacrylate-*co*-(4-benzoylphenyl) methacrylate) P(MA-*co*-MMA-*co*-MABP)

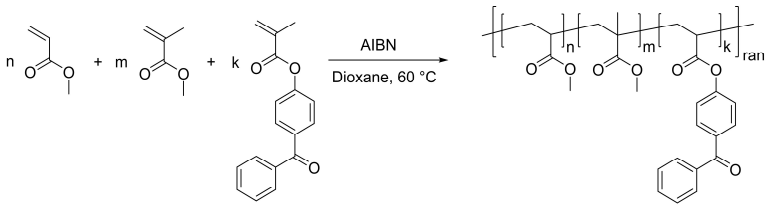

The polymer synthesis was adapted from a literature known procedure.[139]

6.2 g of MABP (24.00 mmol, 0.050 eq.) was dissolved in 170.0 mL of dioxane before adding 25.0 mL of MA (276.00 mmol, 0.570 eq.) and 19.6 mL of MMA (139.00 mmol, 0.380 eq.). The resulting solution was purged with argon for 45 min. In parallel, 0.4 g of AIBN (2.42 mmol, 0.005 eq. relative to the total monomer content) was dissolved in 8.0 mL of dioxane in a separate Schlenk flask and degassed as well. The monomer solution was heated to 60 °C before adding the AIBN solution. After 24 h, the mixture was continuously cooled in an ice bath. The crude polymer was precipitated in an excess of methanol, collected by filtration, and dried under reduced pressure at 40 °C for 16 h. For purification, the polymer was redissolved in dichloromethane and reprecipitated in methanol, followed by filtration and an additional drying step under reduced pressure at 40 °C for 16 h. The final product, P(MA-*co*-MMA-*co*-MABP), was obtained as a white powder. The ^{1}H-NMR spectrum is shown in Chapter 3.3.1, Figure 48c.

Yield: 45.6 g (95 %)

5.5.3 Nonwoven preparation

5.5.3.1 Neat String fibers

1) Preparation of solution

A 25 wt% solution of P(MA-*co*-MMA-*co*-MABP):PAN (8:1 wt/wt) in DMF was prepared and stirred at room temperature overnight at 300 rpm.

2) Electrospinning in a custom-made set-up (with rotating plate collector)

The solution was filled in a 2 mL syringe and was then further equipped with a 0.8 mm blunt-ended cannula. During spinning, a temperature of 23 °C and a humidity level of 30 - 50 % were measured. All fibers were collected on baking paper that was mounted on the rotating plate collector with the syringe fixed above. The following table gives an overview of the other process parameters.

Table 16: Overview of the process parameters applied for neat string nonwoven electrospinning using the rotating plate collector.

Feed rate [mL/h]	Voltage [kV]	Needle-collector distance [cm]
1.0	+ 12.6	20

UV-crosslinking was conducted using a *UVHand 250 GS* lamp (*Dr. Hönle AG*) for 3 h, with a wavelength from 320 - 400 nm and a power of 60 mW/cm^2 in a nitrogen atmosphere. The distance between the sample and the lamp was 15 cm.

5.5.3.2 Neat Bead fibers

1) Preparation of solution

A 31.5 wt% solution of P(NAS-*co*-BPAA) in DMF was prepared and stirred at room temperature overnight at 300 rpm.

2) Electrospinning in a custom-made set-up (with rotating plate collector)

The solution was filled in a 2 mL syringe and was then further equipped with a 0.8 mm blunt-ended cannula. During spinning, a temperature of 23 °C and a humidity level of 30 - 50 % were measured. All fibers were collected on baking paper that was mounted on the rotating plate collector with the syringe fixed above. The following table gives an overview of the other process parameters.

Table 17: Overview of the process parameters applied for neat bead nonwoven electrospinning using the rotating plate collector.

Feed rate [mL/h]	Voltage [kV]	Needle-collector distance [cm]
0.6	+ 11.5	20

UV-crosslinking was conducted analogous to Chapter 5.5.3.1.

5.5.3.3 Bead-on-String fibers

1) Preparation of solution

Two solutions were prepared with DMF serving as solvent for both. Therefore, a 27.5 wt% solution of P(MA-*co*-MMA-*co*-MABP):PAN (8:1 wt/wt) and a 20 wt% solution of P(NAS-*co*-BPAA) were prepared and stirred at room temperature overnight at 300 rpm.

2) Electrospinning in a custom-made set-up (with side-by-side spinning nozzle)

The Side-by-Side Electrospinning was adapted from a previously published procedure.[140]

The solutions were filled in 2 mL syringes and were then further equipped with the side-by-side spinning nozzle. The end of the nozzle consisted of two half circles (350 µm radius) that were separated by a metal plate (350 µm width). During spinning, a temperature of 23 °C and a humidity level of 30 - 50 % were measured. All fibers were collected on baking paper (30 x 40 cm) that was mounted below the side-by-side spinning nozzle (see Chapter 3.3.2, Figure 49). The following table gives an overview of the other process parameters.

Table 18: Overview of the process parameters applied for neat BOS nonwoven prepared by Side-by-Side Electrospinning.

Feed rate [mL/h]	Voltage [kV]	Needle-collector distance [cm]
0.5	+ 13.4	30

UV-crosslinking was conducted analogous to Chapter 5.5.3.1.

5.5.4 Sponge preparation

5.5.4.1 Neat String, Bead and Bead-on-String fiber sponges

1) Preparation of solutions

The respective fiber membranes were cut into ~ 2 x 2 cm pieces by hand and were placed in a mixer (*Gastroback kitchen mixer*) before dioxane was added reaching a fiber concentration c_{SF} of 5.00 respectively 8.76 mg/mL. The fibers were cut into short fibers at a rotation speed of ~ 5000 rpm. The length of the fibers was checked in regular intervals analyzing drops of suspension *via* optical microscope. The duration of cutting was between 30 - 90 s.

2) Preparation of neat sponges

6.0 g of each short fiber suspension was transferred into a cylindrical glass vial (19 mm diameter) and slowly frozen in liquid nitrogen before being freeze dried (- 109 °C, 0.005 mbar, 24 h). At least five replicates were prepared for each sponge type.

5.5.4.2 Sponge functionalization *via* blending approach

1) Preparation of solution

The electrospun BOS fibers were cut into ~ 2 x 2 cm pieces by hand before being dispersed in *tert*-butanol reaching a fiber concentration of 12.00 mg/mL. The fibers got cut for 90 s at ~ 5000 rpm. This short fiber suspension served as a stock solution for the following preparation of functionalized sponges.

2) Preparation of functionalized sponges

For the AgNW functionalized sponges, 4.0 g (respectively 5.0 g in case of the sponges with a final short fiber concentration of 8.76 mg/mL) of the short fiber stock solution were mixed with 0.2, 0.4, or 0.6 mL of an aqueous 1.9 wt% AgNW suspension ($AgNW_{3D}$). Additional *tert*-butanol was added to adjust the short fiber concentration c_{SF} to either 5.00 mg/mL or 8.76 mg/mL. The resulting suspensions were homogenized, and 6.0 g of each suspension was transferred into a cylindrical glass vial (19 mm diameter), slowly frozen in liquid nitrogen, and subsequently freeze-dried (- 109 °C, 0.005 mbar, 24 h). At least five replicates were prepared for each sponge type.

5.5.4.3 Sponge functionalization *via* dip-coating approach

The AgNW functionalization of 3D BOS sponges was adapted from a previously published approach.[83]

Sponges, prepared with a short fiber concentration c_{SF} of either 5.00 or 8.76 mg/mL, were immersed in solutions composed of 14.4 mL deionized water and 0.6 mL of an aqueous 1.9 wt% AgNW suspension ($AgNW_{3D}$) each. The sponges remained in the solution for 36 h under continuous shaking at 250 rpm. Afterwards, they were thoroughly washed, rapidly frozen in liquid nitrogen, and subsequently freeze-dried (- 109 °C, 0.005 mbar, 24 h).

5.5.4.4 Janus sponge

To fabricate janus sponges, two distinct fiber suspensions were first prepared. The non-functionalized suspension consisted of pure bead-on-string fibers at a short fiber concentration c_{SF} of 8.76 mg/mL, following the procedure outlined in Chapter 5.5.4.1.

For the AgNW functionalized suspension, 5.0 g of the short fiber stock solution from Chapter 5.5.4.2 was mixed with 0.2 mL of an aqueous 1.9 wt% AgNW suspension ($AgNW_{3D}$), and *tert*-butanol was added until the same c_{SF} of 8.76 mg/mL was reached.

For the assembly of the janus sponge, 2.5 g of the non-functionalized suspension was weighed into a cylindrical glass vial (19 mm diameter) and slowly frozen over a dry ice/acetone bath. Shortly before the surface of this layer was completely frozen, 2.5 g of the AgNW functionalized suspension, pre-loaded into a syringe, was carefully layered on top and frozen in the same manner. Finally, the structure was capped by adding another 2.5 g layer of the non-functionalized suspension, which was also frozen as before. After the entire layered construct was completely frozen, it was freeze-dried (- 109 °C, 0.005 mbar, 24 h).

6 References

[1] M. A. Meyers, P.-Y. Chen, A. Y.-M. Lin, Y. Seki, *Prog. Mater. Sci.* **2008**, *53*, 1.

[2] N. Pan, *Appl. Phys. Rev.* **2014**, *1*, 21302.

[3] P. Fratzl, R. Weinkamer, *Prog. Mater. Sci.* **2007**, *52*, 1263.

[4] S. Keten, Z. Xu, B. Ihle, M. J. Buehler, *Nat. Mater* **2010**, *9*, 359.

[5] W.-G. Bae, H. N. Kim, D. Kim, S.-H. Park, H. E. Jeong, K.-Y. Suh, *Adv. Mater.* **2014**, *26*, 675.

[6] H. Xu, S. Yagi, S. Ashour, L. Du, M. E. Hoque, L. Tan, *Macro. Materials. & Eng.* **2023**, *308*.

[7] A. Alvarez-Fernandez, J. Maiz, *RSC Appl. Polym.* **2024**, *2*, 1013.

[8] N. Bhardwaj, S. C. Kundu, *Biotechnol. Adv.* **2010**, *28*, 325.

[9] D. Ji, Y. Lin, X. Guo, B. Ramasubramanian, R. Wang, N. Radacsi, R. Jose, X. Qin, S. Ramakrishna, *Nat Rev Methods Primers* **2024**, *4*.

[10] J. Xue, T. Wu, Y. Dai, Y. Xia, *Chem. Rev.* **2019**, *119*, 5298.

[11] S. Agarwal, M. Burgard, A. Greiner, J. Wendorff, *Electrospinning*. *A practical guide to nanofibers*, **2016**.

[12] I. Alghoraibi, S. Alomari in *Handbook of Nanofibers*, pp. 1–46.

[13] Y.-Z. Long, X. Yan, X.-X. Wang, J. Zhang, M. Yu in *Electrospinning: Nanofabrication and Applications*, **2019**, pp. 21–52.

[14] G. Taylor, *Proc. R. Soc. Lond. A* **1969**, *313*, 453.

[15] Q. Gao, S. Agarwal, A. Greiner, T. Zhang, *Prog. Mater. Sci.* **2023**, *137*, 101139.

[16] F. E. Ahmed, B. S. Lalia, R. Hashaikeh, *Desalination* **2015**, *356*, 15.

[17] A. Celebioglu, T. Uyar, *Nanoscale* **2012**, *4*, 621.

[18] G. Zheng, W. Li, X. Wang, D. Wu, D. Sun, L. Lin, *J. Phys. D: Appl. Phys.* **2010**, *43*, 415501.

[19] M. M. Nazemi, A. Khodabandeh, A. Hadjizadeh, *ACS Appl. Bio Mater.* **2022**, *5*, 394.

[20] T. D. Brown, P. D. Dalton, D. W. Hutmacher, *Prog. Mater. Sci.* **2016**, *56*, 116.

[21] S. Zainuddin, T. Scheibel, *Textiles* **2022**, *2*, 124.

[22] N. Zander, *Polymers* **2013**, *5*, 19.

[23] S. Park, K. Park, H. Yoon, J. Son, T. Min, G. Kim, *Polym. Int.* **2007**, *56*, 1361.

[24] M. Langner, A. Greiner, *Macromol. Rapid Commun.* **2016**, *37*, 351.

[25] D. Zong, X. Zhang, X. Yin, F. Wang, J. Yu, S. Zhang, B. Ding, *Adv. Fiber Mater.* **2022**, *4*, 1434.

[26] M. Gong, L. Zhang, P. Wan, *Prog. Mater. Sci.* **2020**, *107*, 101279.

[27] Y. Wang, T. Yokota, T. Someya, *NPG Asia Mater* **2021**, *13*.

[28] A. Greiner, J. H. Wendorff, *Angew. Chem. Int. Ed.* **2007**, *46*, 5670.

[29] A. Townsend-Nicholson, S. N. Jayasinghe, *Biomacromolecules* **2006**, *7*, 3364.

[30] Y. J. Son, W. J. Kim, H. S. Yoo, *Arch. Pharmacal Res.* **2014**, *37*, 69.

[31] L. Liu, W. Xu, Y. Ding, S. Agarwal, A. Greiner, G. Duan, *Compos. Commun.* **2020**, *22*, 100506.

[32] B. Subeshan, A. Atayo, E. Asmatulu, *J Mater Sci* **2024**, *59*, 14095.

[33] T. Valente, J. L. Ferreira, C. Henriques, J. P. Borges, J. C. Silva, *J. Appl. Polym. Sci.* **2019**, *136*.

[34] S. Nagam Hanumantharao, S. Rao, *Fibers* **2019**, *7*, 66.

[35] K. Jankowska, Z. Su, T. Jesionowski, J. Zdarta, M. Pinelo, *Environ. Technol. Innov.* **2023**, *32*, 103408.

[36] S. S. Zargarian, V. Haddadi-Asl, Z. Kafrashian, M. Azarnia, M. M. Mirhosseini, E. Seyedjafari, *J. Biomed. Mater. Res. A* **2019**, *107*, 597.

[37] H. Che, J. Yuan, *J. Mater. Chem. B* **2021**, *10*, 8.

[38] P. Sagitha, C. R. Reshmi, S. P. Sundaran, A. Sujith, *Eur. Polym. J.* **2018**, *105*, 227.

[39] B. Niemczyk-Soczynska, A. Gradys, P. Sajkiewicz, *Polymers* **2020**, *12*.

[40] K. Müller, J. F. Quinn, A. P. R. Johnston, M. Becker, A. Greiner, F. Caruso, *Chem. Mater.* **2006**, *18*, 2397.

[41] W. Cui, X. Li, C. Xie, H. Zhuang, S. Zhou, J. Weng, *Biomater.* **2010**, *31*, 4620.

[42] J. K. Y. Lee, N. Chen, S. Peng, L. Li, L. Tian, N. Thakor, S. Ramakrishna, *Prog. Polym. Sci.* **2018**, *86*, 40.

[43] J. Singh, S. Thakur, R. Sehgal, A. S. Dhaliwal, V. Kumar in *Electrospun Nanofibers*, pp. 251–283.

[44] G. Wang, D. Yu, A. D. Kelkar, L. Zhang, *Prog. Polym. Sci.* **2017**, *75*, 73.

[45] Y. Liao, C.-H. Loh, M. Tian, R. Wang, A. G. Fane, *Prog. Polym. Sci.* **2018**, *77*, 69.

[46] T. Kowalczyk, *Polymers* **2020**, *12*.

[47] A. Barhoum, M. Bechelany, A. Makhlouf (Eds.) *Handbook of Nanofibers*, **2019**.

[48] N. M. Abbasi, H. Yu, Li Wang, Zain-ul-Abdin, W. A. Amer, M. Akram, H. Khalid, Y. Chen, M. Saleem, R. Sun et al., *Mater. Chem. Phys.* **2015**, *166*, 1.

[49] D. Fu, R. Yang, Y. Wang, R. Wang, F. Hua, *Adv. Mater. Technol.* **2022**, *7*.

[50] S. Nagarajan, S. Balme, S. Narayana Kalkura, P. Miele, C. P. Bohatier, M. Bechelany in *Handbook of Nanofibers*, pp. 347–372.

[51] F. Huang, Q. Wei, Y. Cai in *Functional Nanofibers and their Applications*, **2012**, pp. 92–118.

[52] B. M. Thamer, A. Aldalbahi, M. Moydeen A, M. Rahaman, M. H. El-Newehy, *Polymers* **2020**, *13*.

[53] J. Liu, P. Zhou, L. Zhang, Z. Ma, J. Liang, H. Fong, *Carbon* **2009**, *47*, 1087.

[54] R. Gopal, M. Zuwei, S. Kaur, S. Ramakrishna in *Topics in Applied Physics*, *Vol. 109*, **2007**, pp. 72–91.

[55] C. Brandl, A. Greiner, S. Agarwal, *Macro Materials & Eng* **2011**, *296*, 858.

[56] M. Langner, S. Agarwal, A. Baudler, U. Schröder, A. Greiner, *Adv. Funct. Mater.* **2015**, *25*, 6182.

[57] Y. I. Kim, S. An, M.-W. Kim, H.-S. Jo, T.-G. Kim, M. T. Swihart, A. L. Yarin, S. S. Yoon, *J. Alloys Compd.* **2019**, *790*, 1127.

[58] S. Soltanian, R. Rahmanian, B. Gholamkhass, N. M. Kiasari, F. Ko, P. Servati, *Adv. Energy Mater.* **2013**, *3*, 1332.

[59] D. Kulkarni, S. Musale, P. Panzade, A. C. Paiva-Santos, P. Sonwane, M. Madibone, P. Choundhe, P. Giram, S. Cavalu, *Nanomater.* **2022**, *12*.

[60] L. Duque Sánchez, N. Brack, A. Postma, P. J. Pigram, L. Meagher, *Biomater.* **2016**, *106*, 24.

[61] L. Zhang, A. Aboagye, A. Kelkar, C. Lai, H. Fong, *J Mater Sci* **2014**, *49*, 463.

[62] W.-H. Han, Q.-Y. Wang, Y.-Y. Kang, L.-R. Shi, Y. Long, X. Zhou, C.-C. Hao, *Nanoscale* **2023**, *15*, 15513.

[63] A. M. Yessuf, M. Bahri, T. S. Kassa, B. P. Sharma, A. M. Salama, C. Xing, Q. Zhang, Y. Liu, *ACS Appl. Bio Mater.* **2024**, *7*, 4231.

[64] S. K. Nemani, R. K. Annavarapu, B. Mohammadian, A. Raiyan, J. Heil, M. A. Haque, A. Abdelaal, H. Sojoudi, *Adv Materials Inter* **2018**, *5*.

[65] Y. Dai, K. Qi, K. Ou, Y. Song, Y. Zhou, M. Zhou, H. Song, J. He, H. Wang, R. Wang, *ACS Appl. Mater. Interfaces.* **2023**, *15*, 11244.

[66] G. Heness in *Advances in Polymer Nanocomposites*, **2012**, pp. 164–177.

[67] A. Kausar, *J. Plast. Film Sheeting* **2019**, *35*, 65.

[68] P. Zhang, I. Wyman, J. Hu, S. Lin, Z. Zhong, Y. Tu, Z. Huang, Y. Wei, *Mater. Sci. Eng. B* **2017**, *223*, 1.

[69] L. Yang, X. Huang, H. Wu, Y. Liang, M. Ye, W. Lu, F. Li, T. Xu, H. Wang, *Eng. Sci.* **2023**.

[70] X. Jiang, X. Qiu, G. Fu, J. Sun, Z. Huang, D. Sun, L. Xu, J. Zhou, Y. Tang, *J. Mater. Chem. A* **2018**, *6*, 17682.

[71] S. Ye, A. R. Rathmell, Z. Chen, I. E. Stewart, B. J. Wiley, *Adv. Mater.* **2014**, *26*, 6670.

[72] Y. Song, R. M. Garcia, R. M. Dorin, H. Wang, Y. Qiu, E. N. Coker, W. A. Steen, J. E. Miller, J. A. Shelnutt, *Nano Lett.* **2007**, *7*, 3650.

[73] Z. Xia, W. Wen, *Nanomater.* **2016**, *6*.

[74] F. Cheng, Z. Tao, J. Liang, J. Chen, *Chem. Mater.* **2008**, *20*, 667.

[75] M. P. Proenca, C. T. Sousa, J. Escrig, J. Ventura, M. Vazquez, J. P. Araujo, *J. Appl. Phys.* **2013**, *113*.

[76] L. Bardet, D. T. Papanastasiou, C. Crivello, M. Akbari, J. Resende, A. Sekkat, C. Sanchez-Velasquez, L. Rapenne, C. Jiménez, D. Muñoz-Rojas et al., *Nanomater.* **2021**, *11*.

[77] G. Kawamura, H. Muto, A. Matsuda, *Front. Chem.* **2014**, *2*, 104.

[78] A. Zhang, G. Zheng, C. M. Lieber, *Nanowires*, **2016**.

[79] N. A. C. Lah, S. Trigueros, *Sci. Technol. Adv. Mater.* **2019**, *20*, 225.

[80] B. Silva, W. Da Silva, S. Saraiva, L. Otubo, *J. Braz. Chem. Soc.* **2024**.

[81] L. Bai, Z.-M. Zhang, J.-H. Pu, C.-P. Feng, X. Zhao, R.-Y. Bao, Z.-Y. Liu, M.-B. Yang, W. Yang, *Polymer* **2020**, *194*, 122390.

[82] D. Doganay, S. Coskun, C. Kaynak, H. E. Unalan, *Compos. B Eng.* **2016**, *99*, 288.

[83] D. Fang, Y.-T. Liu, B. Ding, A. Greiner, *Macro. Materials. & Eng.* **2024**, *309*.

[84] K. Park, S. Kang, J.-W. Park, J. Hwang, *J. Hazard. Mater.* **2021**, *411*, 125043.

[85] C.-L. Zhang, K.-P. Lv, N.-Y. Hu, Le Yu, X.-F. Ren, S.-L. Liu, S.-H. Yu, *Small* **2012**, *8*, 2936.

[86] H. S. Jo, H.-J. Kwon, T.-G. Kim, C.-W. Park, S. An, A. L. Yarin, S. S. Yoon, *Nanoscale* **2018**, *10*, 19825.

[87] Y. Lu, J. Jiang, S. Yoon, K.-S. Kim, J.-H. Kim, S. Park, S.-H. Kim, L. Piao, *ACS Appl. Mater. Interfaces.* **2018**, *10*, 2093.

[88] K. Yadav, R. Nain, M. Jassal, A. K. Agrawal, *Compos. Sci. Technol.* **2019**, *182*, 107766.

[89] C. Sun, S. Liu, X. Shi, C. Lai, J. Liang, Y. Chen, *J. Chem. Eng.* **2020**, *381*, 122641.

[90] J. Jung, H. Cho, R. Yuksel, D. Kim, H. Lee, J. Kwon, P. Lee, J. Yeo, S. Hong, H. E. Unalan et al., *Nanoscale* **2019**, *11*, 20356.

[91] C. Li, M. Chen, B. Xie, *J. Phys. D: Appl. Phys.* **2024**.

[92] A. T. Bellew, H. G. Manning, C. Da Gomes Rocha, M. S. Ferreira, J. J. Boland, *ACS nano* **2015**, *9*, 11422.

[93] H. Wu, J. Fan, N. Du, *J. Appl. Polym. Sci.* **2007**, *106*, 576.

[94] J. Yun, *Soft. Sci.* **2023**, *3*, 12.

[95] R. Hu, Y. Liu, S. Shin, S. Huang, X. Ren, W. Shu, J. Cheng, G. Tao, W. Xu, R. Chen et al., *Adv. Energy Mater.* **2020**, *10*.

[96] F. Lebeda, M. Demleitner, A. Pongratz, H. Ruckdäschel, M. Retsch, *ACS omega* **2024**, *9*, 39232.

[97] X. Lian, L. Tian, Z. Li, X. Zhao, *Int. J. Heat Mass Transf.* **2024**, *220*, 124941.

[98] N. Burger, A. Laachachi, M. Ferriol, M. Lutz, V. Toniazzo, D. Ruch, *Prog. Polym. Sci.* **2016**, *61*, 1.

[99] N. Mehra, L. Mu, T. Ji, X. Yang, J. Kong, J. Gu, J. Zhu, *Appl. Mater. Today* **2018**, *12*, 92.

[100] N. Yüksel in *Insulation Materials in Context of Sustainability* (Eds.: A. Almusaed, A. Almssad), **2016**.

[101] "Thermal Insulation Materials. Material Characterization, Phase Changes, Thermal Conductivity", can be found under https://analyzing-testing.netzsch.com/_Resources/Persistent/c/1/3/b/c13b995631cc9637b854c5ed9a103aead7a15832/Thermal_Insulation_Materials_E_0214.pdf.

[102] T. Ishizaki, H. Nagano, *Int. J. Therm. Sci.* **2023**, *193*, 108475.

[103] T. Tran, C. Kodisch, M. Schöttle, N. W. Pech-May, M. Retsch, *J. Phys. Chem. C* **2022**, *126*, 14003.

[104] K. Razeeb, E. Dalton in *Advances in Nanocomposites - Synthesis, Characterization and Industrial Applications*, InTech, **2011**.

[105] M. Das, J. Knapczyk-Korczak, A. Moradi, W. Pichór, U. Stachewicz, *Mater. Adv.* **2025**, *6*, 1859.

[106] J. Tan, Y. Zhang, *Molecules* **2024**, *29*.

[107] Q. Sun, G. Zhi, S. Zhou, X. Dong, Q. Shen, R. Tao, J. Qi, *Adv. Mater. Technol.* **2024**, *9*.

[108] Y. Peng, Y. Cui, *Natl. Sci. Rev.* **2024**, *11*, nwae295.

[109] D. Langley, G. Giusti, C. Mayousse, C. Celle, D. Bellet, J.-P. Simonato, *Nanotechnol.* **2013**, *24*, 452001.

[110] M. Ataei, M. Yousefzadeh, M. Montazer, S. Ramakrishna, *Macro. Materials. & Eng.* **2025**.

[111] Q. Shao, B. Xing, X. Liu, Z. Du, W. Yu, A. Greiner, *Text. Res. J.* **2025**.

[112] M. Hu, Q. Ma, Y. Yuan, Y. Pan, M. Chen, Y. Zhang, D. Long, *Chem. Eng. J.* **2020**, *388*, 124258.

[113] R. Zhao, X. Li, B. Sun, Y. Li, Y. Li, R. Yang, C. Wang, *J. Mater. Chem. A* **2017**, *5*, 1133.

[114] Q. Shao, B. Xing, Z. Du, W. Yu, *Polymers* **2024**, *16*.

[115] F. T. Peirce, *J. Text. Inst.* **1926**, *17*, T355-T368.

[116] D. A. Brennan, K. Shirvani, C. D. Rhoads, S. E. Lofland, V. Z. Beachley, *MRS Commun.* **2019**, *9*, 764.

[117] X. Hou, X. Yang, L. Zhang, E. Waclawik, S. Wu, *Mater. Des.* **2010**, *31*, 1726.

[118] A. R. Bagheri, M. Abdouss, A. M. Shoushtari, M. Javanbakht, M. Zargaran, *CTAIJ* **2007**, *2*, 100.

[119] C. Zhao, B. Zhou, *J. Funct. Biomater.* **2022**, *14*.

[120] C. Zhang, Z. Ren, Z. Yin, L. Jiang, S. Fang, *Spectrochim Acta A Mol Biomol Spectrosc* **2011**, *81*, 598.

[121] S. Reich, M. Burgard, M. Langner, S. Jiang, X. Wang, S. Agarwal, B. Ding, J. Yu, A. Greiner, *npj Flex Electron* **2018**, *2*.

[122] Y. Zhao, M. L. Fitzgerald, Y. Tao, Z. Pan, G. Sauti, D. Xu, Y.-Q. Xu, D. Li, *Nano Lett.* **2020**, *20*, 7389.

[123] Z. Cheng, L. Liu, S. Xu, M. Lu, X. Wang, *Sci. Rep.* **2015**, *5*, 10718.

[124] J. Hou, X. Wang, L. Zhang, *APL* **2006**, *89*.

[125] M. Alaghemandi, M. Alamandi, *Heat Transfer in Composite Materials: Mechanisms and Applications*, **2025**.

[126] M. L. Fitzgerald, Z. Pan, G. Sauti, D. Li, *ACS Appl. Polym. Mater.* **2025**, *7*, 1394.

[127] C. Tang, K. Zhang, S. Yu, H. Guan, M. Cao, K. Zhang, Y. Pan, S. Zhang, X. Sun, H. Peng, *Small* **2024**, *20*, e2405000.

[128] I. Klein, S. E. Fritze, A. Berger, H. Schmalz, M. Retsch, A. Greiner, *ACS Appl. Polym. Mater.* **2026**, *8*, 1954.

[129] X. Wan, Y. Zhao, Z. Li, L. Li, *Exploration* **2022**, *2*, 20210029.

[130] H. Yuan, S. Zhao, H. Tu, B. Li, Q. Li, B. Feng, H. Peng, Y. Zhang, *J. Mater. Chem.* **2012**, *22*, 19634.

[131] P. Kiselev, J. Rosell-Llompart, *J. Appl. Polym. Sci.* **2012**, *125*, 2433.

[132] J. Xu, Y. Zhang, *Fibers Polym* **2017**, *18*, 2146.

[133] S. Chen, C. Ding, Y. Lin, X. Wu, W. Yuan, X. Meng, W. Su, K.-Q. Zhang, *RSC Adv.* **2020**, *10*, 21845.

[134] W. M. Haynes (Ed.) *CRC handbook of chemistry and physics*, **2017**.

[135] K. Ruan, Y. Guo, C. Lu, X. Shi, T. Ma, Y. Zhang, J. Kong, J. Gu, *Research* **2021**, *2021*, 8438614.

[136] K.-I. Jang, K. Li, H. U. Chung, S. Xu, H. N. Jung, Y. Yang, J. W. Kwak, H. H. Jung, J. Song, C. Yang et al., *Nat. Commun* **2017**, *8*, 15894.

[137] W. Chen, Y. Xu, Y. Liu, Z. Wang, Y. Li, G. Jiang, X. Mo, G. Zhou, *Mater. Des.* **2019**, *179*, 107886.

[138] G. Ye, Z. Song, T. Yu, Q. Tan, Y. Zhang, T. Chen, C. He, L. Jin, N. Liu, *ACS Appl. Mater. Interfaces.* **2020**, *12*, 1486.

[139] G. Duan, S. Jiang, V. Jérôme, J. H. Wendorff, A. Fathi, J. Uhm, V. Altstädt, M. Herling, J. Breu, R. Freitag et al., *Adv. Funct. Mater.* **2015**, *25*, 2850.

[140] M. Schmidt, C. Riecken, E. Zussman, S. Agarwal, H. Schmalz, A. Greiner, *Adv Materials Inter* **2025**, *12*.

[141] M. Gernhardt, L. Peng, M. Burgard, S. Jiang, B. Förster, H. Schmalz, S. Agarwal, *Macro Materials & Eng* **2018**, *303*.

[142] D. Puchowicz, M. Cieslak in *Recent Developments in Atomic Force Microscopy and Raman Spectroscopy for Materials Characterization* (Eds.: C. Shakher Pathak, S. Kumar), **2022**.

[143] X. Lu, P. Lin, Y. Huang, X. He, C. Yi, J. Sun, M. U. Farid, A. K. An, J. Guo, *Adv. Fiber Mater.* **2025**.

[144] M. Hojatjalali, S. Bahraminia, M. Anbia, *Sci. Rep.* **2025**, *15*, 7378.

[145] R. Kurpanik, E. Stodolak-Zych, *Eng. Biomater.* **2021**, 31.

[146] S. Jiang, S. Reich, B. Uch, P. Hu, S. Agarwal, A. Greiner, *ACS Appl. Mater. Interfaces.* **2017**, *9*, 34286.

[147] Y. Xu, Z. Ye, G. Zhao, Q. Fei, Z. Chen, J. Li, M. Yang, Y. Ren, B. Berigan, Y. Ling et al., *Nat. Nanotechnol* **2024**, *19*, 1158.

[148] C. Xu, J. Y. Cheong, X. Mo, V. Jérôme, R. Freitag, S. Agarwal, R. Gharibi, A. Greiner, *Macromol. Biosci.* **2023**, *23*, e2300143.

[149] T. Gries, D. Veit, B. Wulfhorst (Eds.) *Textile Fertigungsverfahren*, **2018**.

[150] L. Zhang, H. Deng, Q. Fu, *Compos. Commun.* **2018**, *8*, 74.

[151] D. Le Hung Anh, Z. Pásztory, *J. Build. Eng* **2021**, *44*, 102604.

[152] Q. Gao, T. Tran, X. Liao, S. Rosenfeldt, C. Gao, H. Hou, M. Retsch, S. Agarwal, A. Greiner, *ACS Appl. Mater. Interfaces.* **2022**, *14*, 19918.

[153] M. Lagrange, D. P. Langley, G. Giusti, C. Jiménez, Y. Bréchet, D. Bellet, *Nanoscale* **2015**, *7*, 17410.

[154] Y. Huang, X. Bai, M. Zhou, S. Liao, Z. Yu, Y. Wang, H. Wu, *Nano Lett.* **2016**, *16*, 5846.

[155] J. S. Park, T. Kim, W. S. Kim, *Sci. Rep.* **2017**, *7*, 3246.

[156] D. Kojda, R. Mitdank, M. Handwerg, A. Mogilatenko, M. Albrecht, Z. Wang, J. Ruhhammer, M. Kroener, P. Woias, S. F. Fischer, *Phys. Rev. B* **2015**, *91*.

[157] M. O. Pretscher, G. Sitaru, M. Dietel, H. Schmalz, S. Gekle, S. Agarwal, *ACS Appl. Polym. Mater.* **2021**, *3*, 1349.

[158] F.-S. Du, P. Zhang, F.-M. Li, *J. Appl. Polym. Sci.* **1994**, *51*, 2139.

[159] H. Topsøe, *Geometric factors in four point resistivity measurement*. *Bulletin No. 472-13*, **1966**.

[160] N. N. Greenwood, *Chemie der Elemente*, **1988**.

[161] S. Sharma, K. C. Basavaraju, A. K. Singh, D.-P. Kim, *Org. Lett.* **2014**, *16*, 3974.

7 Appendix

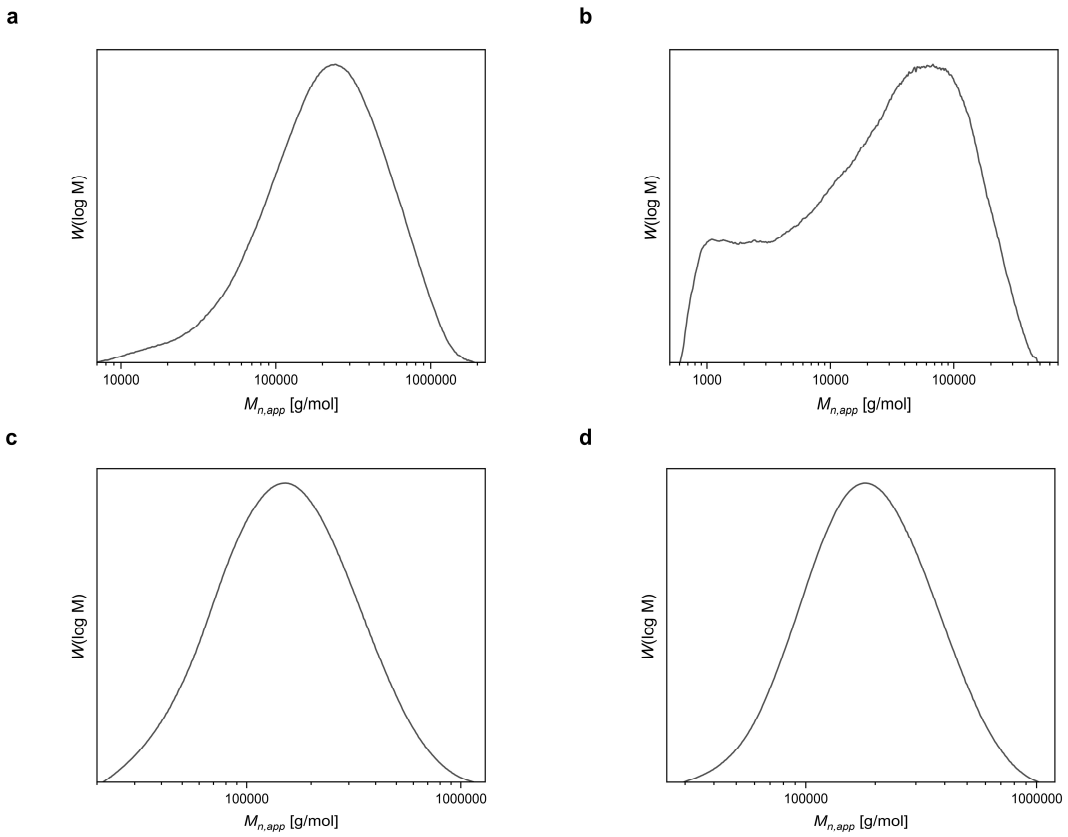

Figure 60: GPC chromatograms of the used commercial base polymers PAN ($M_{n,app}$: 126 000, $M_{w,app}$: 230 000, $Đ$: 2.3) (**a**), PEI ($M_{n,app}$: 6 400, $M_{w,app}$: 55 000, $Đ$: 8.7) both measured in DMF (**b**), PS ($M_{n,app}$: 119 000, $M_{w,app}$: 193 000, $Đ$: 1.6) (**c**) and PCL ($M_{n,app}$: 155 000, $M_{w,app}$: 223 000, $Đ$: 1.44) both measured in chloroform (**d**). All $M_{n,app}$ and $M_{w,app}$ values are given in g/mol.

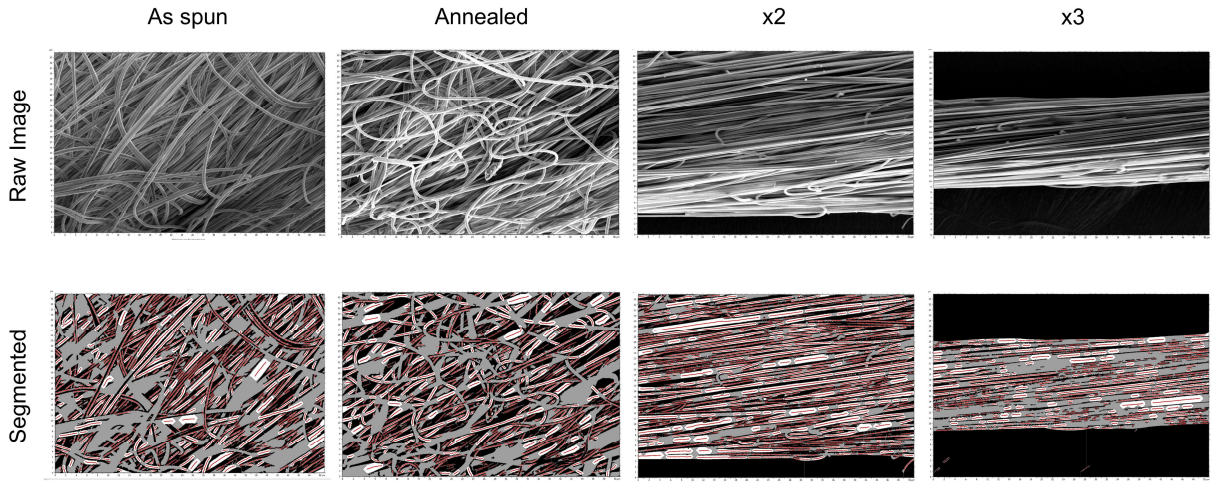

Figure 61: SEM images used to determine the orientation parameters S_{2D} for 1D PAN yarns. Detection and segmentation of the fibers was performed with the *MountainsLab* software. Detected fiber segments are presented in white, each with a red line in its center showing the orientation.

Table 19: Yarn and fiber diameters of the different (modified) 1D PAN yarns and the respective orientation parameters S_{2D}.

Sample	Yarn diameter [µm][a]	Fiber diameter [µm][a]	S_{2D}[a]
PAN_As spun	86.74 ± 3.75	0.69 ± 0.08	0.71
PAN_Annealed	85.78 ± 5.73	0.68 ± 0.08	0.75
PAN_x2	35.41 ± 0.97	0.68 ± 0.10	0.99
PAN_x3	16.33 ± 0.45	0.36 ± 0.05	0.99
PAN_PEI_As spun	-	-	0.41
PAN_PEI_Annealed	-	-	0.72
PAN_PEI_x2	-	-	0.93
PAN_PEI_x3	-	-	0.97

[a] determined from SEM images.

Table 20: Maximum force before failure F_{max} and elongation at break ε_b and YOUNG's modulus E_{mod} of the different (functionalized) 1D PAN yarns as well as the thermal diffusivity values α.

Sample	F_{max} [MPa][a]	ε_b [%][a]	E_{mod} [GPa][a]	α [mm²/s][b]	
PAN_As spun	54.9 ± 5.0	57.5 ± 5.7	1.1 ± 0.2	0.209 ± 0.016	0.177 ± 0.011
PAN_Annealed	108.0 ± 10.9	28.7 ± 3.1	3.4 ± 0.4	0.282 ± 0.020	0.231 ± 0.013
PAN_x2	342.0 ± 32.6	9.7 ± 1.1	13.2 ± 1.5	0.501 ± 0.025	0.373 ± 0.015
PAN_x3	322.0 ± 16.5	7.4 ± 0.6	8.3 ± 0.4	0.516 ± 0.043	0.372 ± 0.358
PAN_PEI_As spun	67.3 ± 3.5	28.6 ± 1.2	1.0 ± 0.1	-	
PAN_PEI_Annealed	116.0 ± 8.7	31.9 ± 0.5	2.8 ± 0.3	-	
PAN_PEI_x2	242.0 ± 18.7	13.1 ± 2.7	6.1 ± 4.4	-	
PAN_PEI_x3	195.0 ± 15.7	12.5 ± 0.5	5.5 ± 0.7	-	
PAN_PEI_AgNW_As spun	-	-	-	0.331 ± 0.015	-
PAN_PEI_AgNW_Annealed	-	-	-	0.410 ± 0.100	-
PAN_PEI_AgNW_x2	-	-	-	0.473 ± 0.045	-
PAN_PEI_AgNW_x3	-	-	-	0.511 ± 0.075	-

[a] determined from tensile testing, [b] determined *via* LIT. The left column provides the α values derived from the evaluation of the phase only, while the right column shows the values resulting from both the phase and amplitude evaluation.

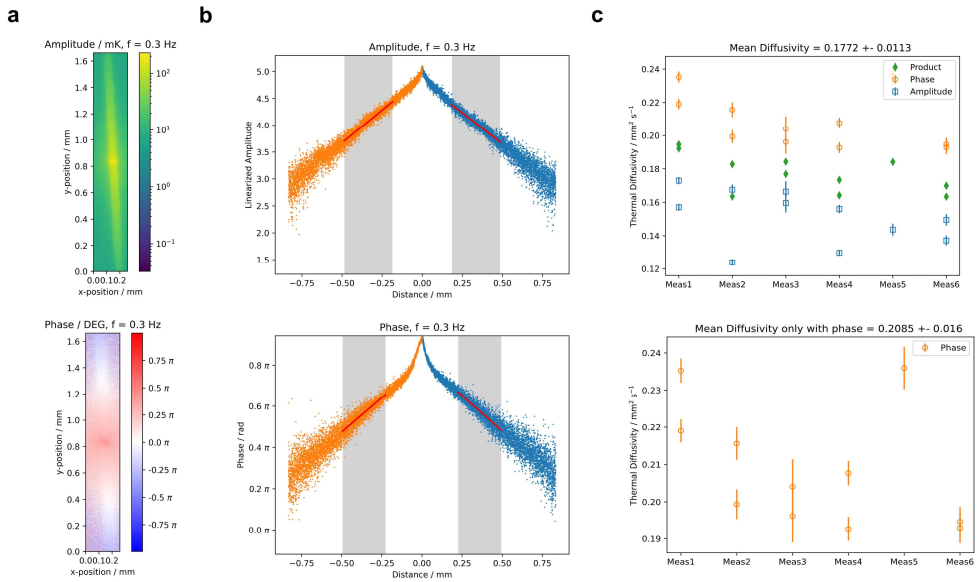

Figure 62: Exemplary Lock-In Thermography data of the as spun 1D PAN yarn: 2D amplitude and phase data of the yarn (**a**), respective linearized 1D plots of the yarn (**b**) and mean diffusivity plots for the different measurements - showcasing the results from both the phase and amplitude evaluation (**c**, **top**) as well as the results from the phase only evaluation (**c**, **bottom**).

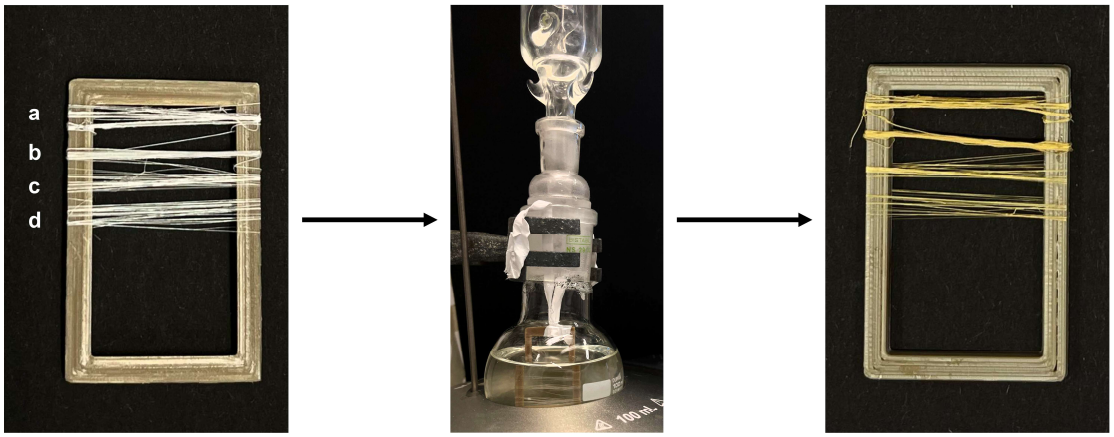

Figure 63: Optical images of neat white 1D PAN yarns mounted on a PEEK frame (1.8 x 3 cm, 0.3 cm frame width) (**left**), the frame being placed in the reaction solution (**middle**) and the yellow PEI modified 1D PAN yarns mounted on the frame after the reaction (**right**). To ensure simultaneous modification, the yarns were fixed on one frame in the following order: as spun (**a**), annealed (**b**), x2 (**c**) and x3 stretching state (**d**).

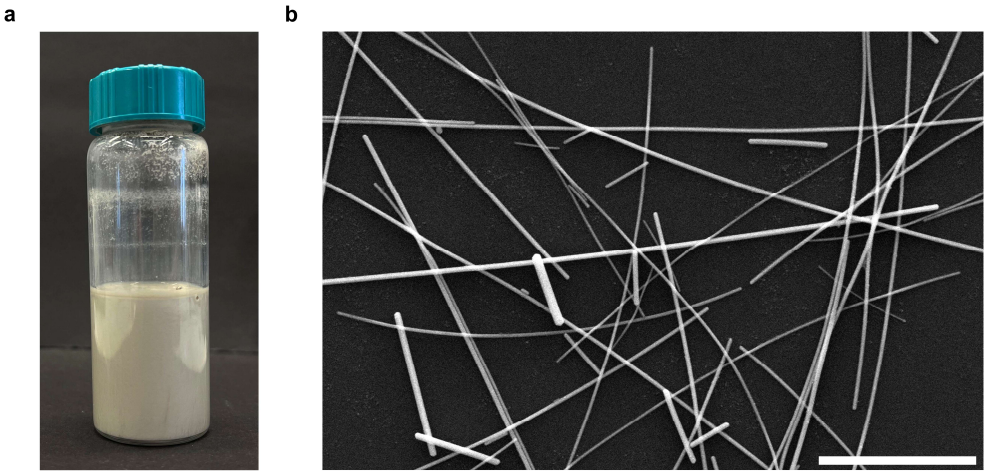

Figure 64: Optical image of the aqueous silver nanowire suspension (**a**) and SEM image of silver nanowires used for 2D PS nonwoven functionalization (3 µm scale bar) (**b**). Reprinted with permission from KLEIN et al.[128] Copyright © 2026, American Chemical Society.

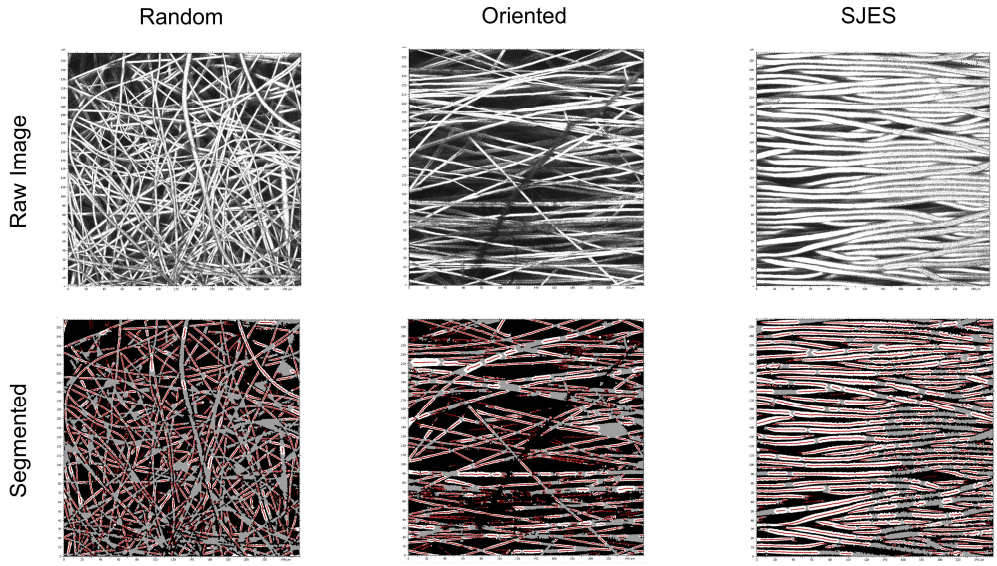

Figure 65: Optical microscopy images used to determine the orientation parameters S_{2D} for 2D PS nonwovens. Detection and segmentation of the fibers was performed with the *MountainsLab* software. Detected fiber segments are presented in white, each with a red line in its center showing the orientation. Reprinted in parts with permission from KLEIN et al.[128] Copyright © 2026, American Chemical Society.

Table 21: Fiber diameters of the different (functionalized) 2D PS nonwovens, the respective orientation parameters S_{2D} as well as the thermal diffusivity values α (adapted from KLEIN et al.).[128]

Sample	Fiber diameter [µm][a]	S_{2D}[b]	α [mm²/s][c]	
PS_random_pressed	2.70 ± 0.45	0.19 ± 0.09	0.048 ± 0.001	
PS_random_3h annealed	3.27 ± 0.64	0.21 ± 0.09	0.074 ± 0.003	
PS_random_24h annealed	3.52 ± 0.92	0.27 ± 0.07	0.083 ± 0.001	
PS_oriented_pressed	2.78 ± 0.35	0.86 ± 0.04	0.011 ± 0.002	0.095 ± 0.007
PS_oriented_3h annealed	4.87 ± 1.18	0.67 ± 0.10	0.041 ± 0.002	0.114 ± 0.004
PS_oriented_24h annealed	4.70 ± 1.38	0.81 ± 0.04	0.052 ± 0.002	0.112 ± 0.005
PS_SJES_pressed	3.98 ± 0.49	0.95 ± 0.3	0.039 ± 0.006	0.109 ± 0.004
PS_SJES_3h annealed	4.39 ± 0.43	0.87 ± 0.09	0.027 ± 0.002	0.139 ± 0.008
PS_SJES_24h annealed	5.09 ± 0.57	0.89 ± 0.03	0.038 ± 0.002	0.137 ± 0.006
PS_AgNW_random	2.06 ± 0.27	0.25 ± 0.16	0.090 ± 0.002	
PS_AgNW_oriented	1.04 ± 0.18	0.58 ± 0.40	0.042 ± 0.002	0.152 ± 0.005
PS_Cu_random	2.72 ± 0.32	0.10 ± 0.12	5.075 ± 0.528	
PS_Cu_oriented	2.77 ± 0.31	0.77 ± 0.05	2.988 ± 0.324	8.451 ± 1.477

[a] determined from SEM images, [b] determined from LEXT images, [c] determined *via* LIT. In the case of splitting columns, the left column represents the α value perpendicular to the preferential fiber direction and the right column represents the value parallel to the preferential direction.

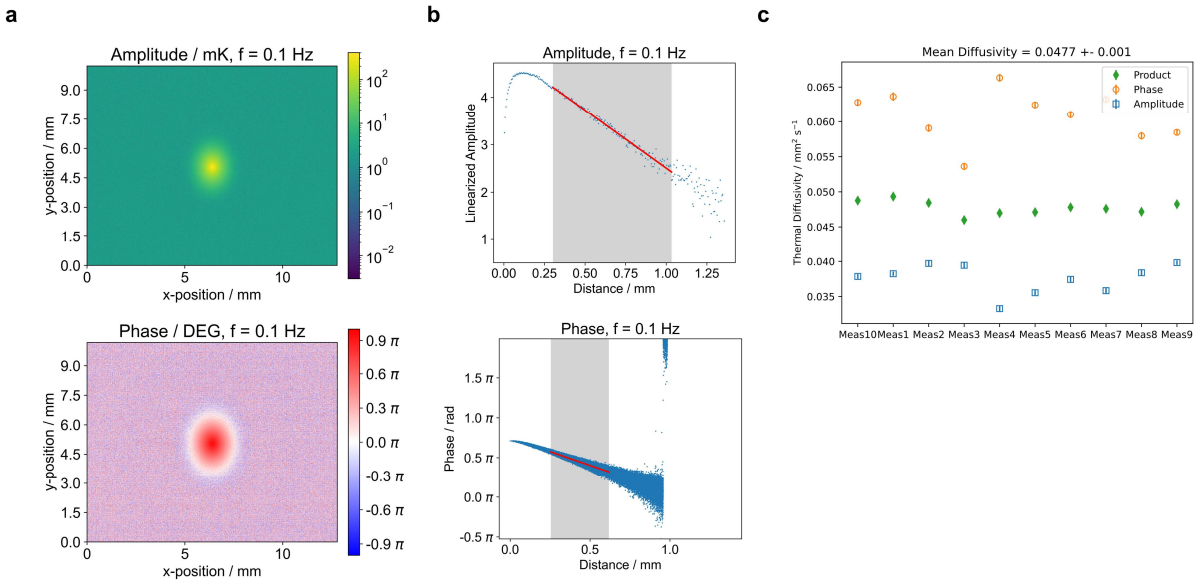

Figure 66: Exemplary Lock-In Thermography data of the random pressed 2D PS nonwoven: 2D amplitude and phase data of the nonwoven (**a**), respective linearized 1D plots of the nonwoven (**b**) and mean diffusivity plot for the different measurements showcasing the results from both the phase and amplitude evaluation (**c**).

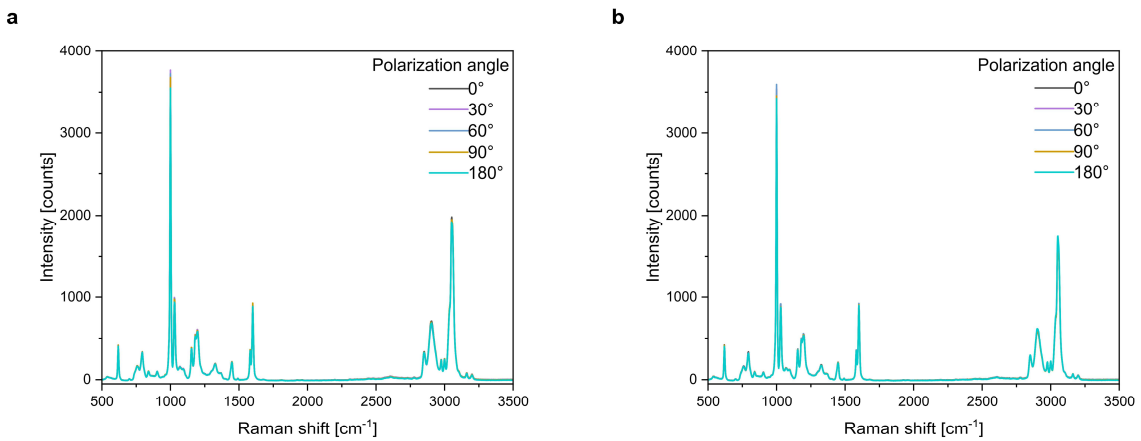

Figure 67: RAMAN spectra utilizing polarized incident radiation (angles ranging from 0° to 180°) of pressed SJES 2D PS nonwoven (**a**) and SJES 2D PS nonwoven annealed at 115 °C for 3 h (**b**) (adapted from KLEIN et al.).[128]

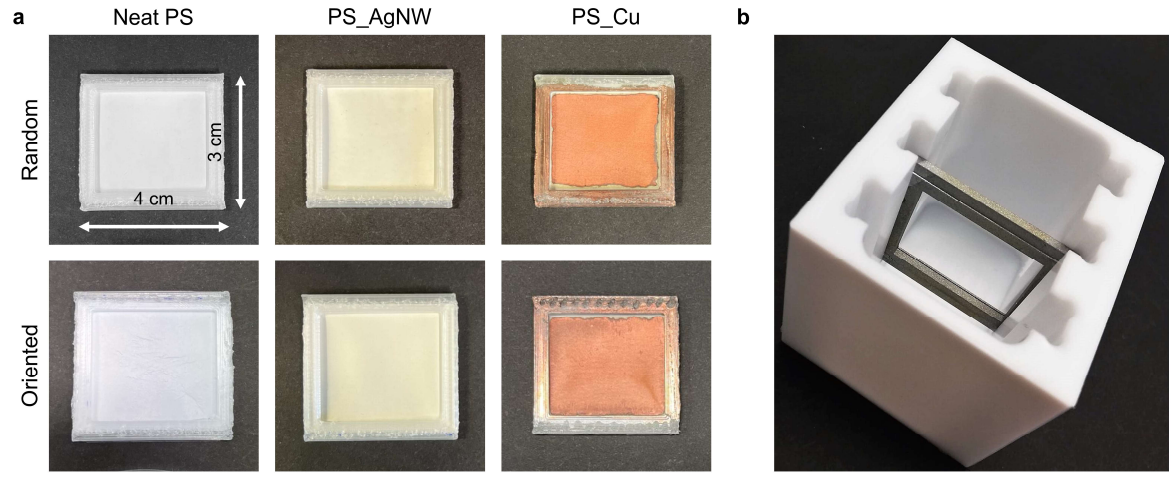

Figure 68: Optical images of the pressed 2D PS nonwovens with different degrees of functionalization mounted in PP frames (3 x 4 cm) (**a**) as well as of the custom-made Teflon reaction container (**b**). Reprinted with permission from KLEIN et al.[128] Copyright © 2026, American Chemical Society.

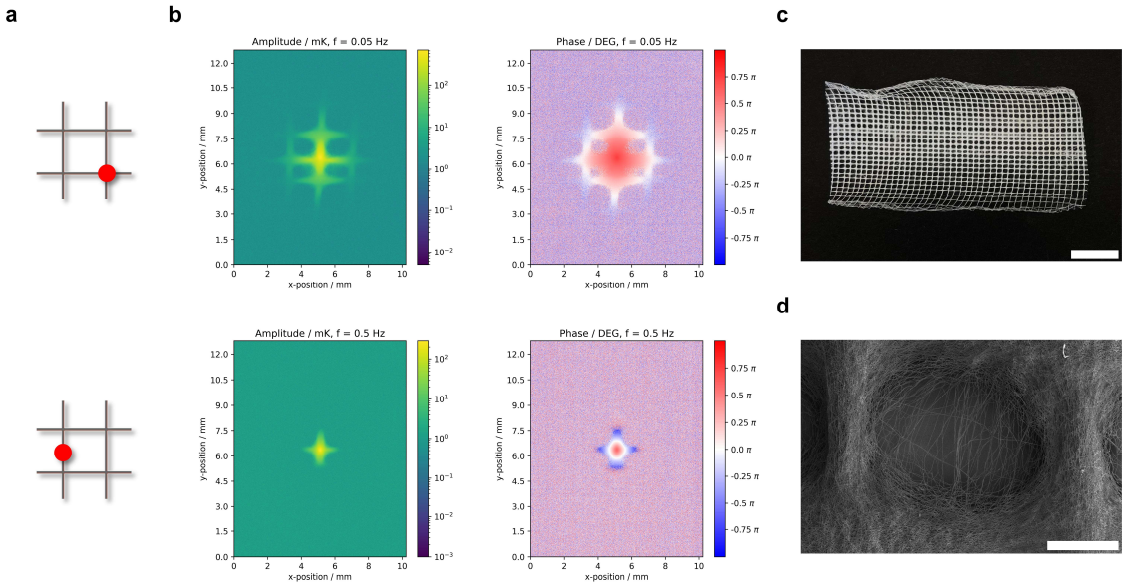

Figure 69: Illustration of the point of laser focusing on the fiber grid (**a**), respective Lock-In Thermography data (comprising amplitude and phase) (**b**), optical image of the 2D PCL grid nonwoven (1 cm scale bar) (**c**) and SEM image of a single grid rectangle (500 µm scale bar) (**d**).

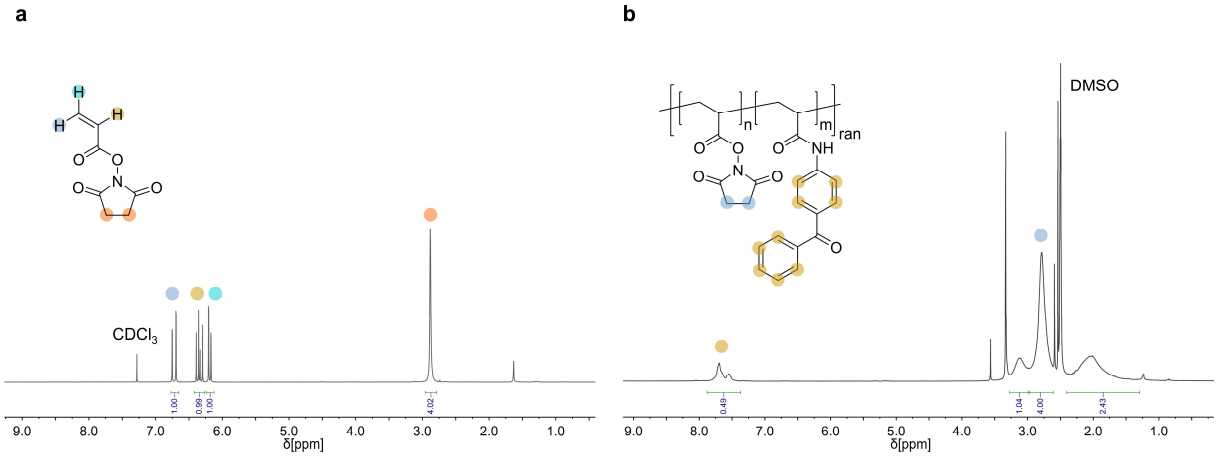

Figure 70: ^{1}H-NMR spectrum of *N*-Succinimidyl acrylate (NAS) in $CDCl_3$ (**a**) next to the spectrum of P(NAS-*co*-BPAA) in DMSO-d_6 (**b**).

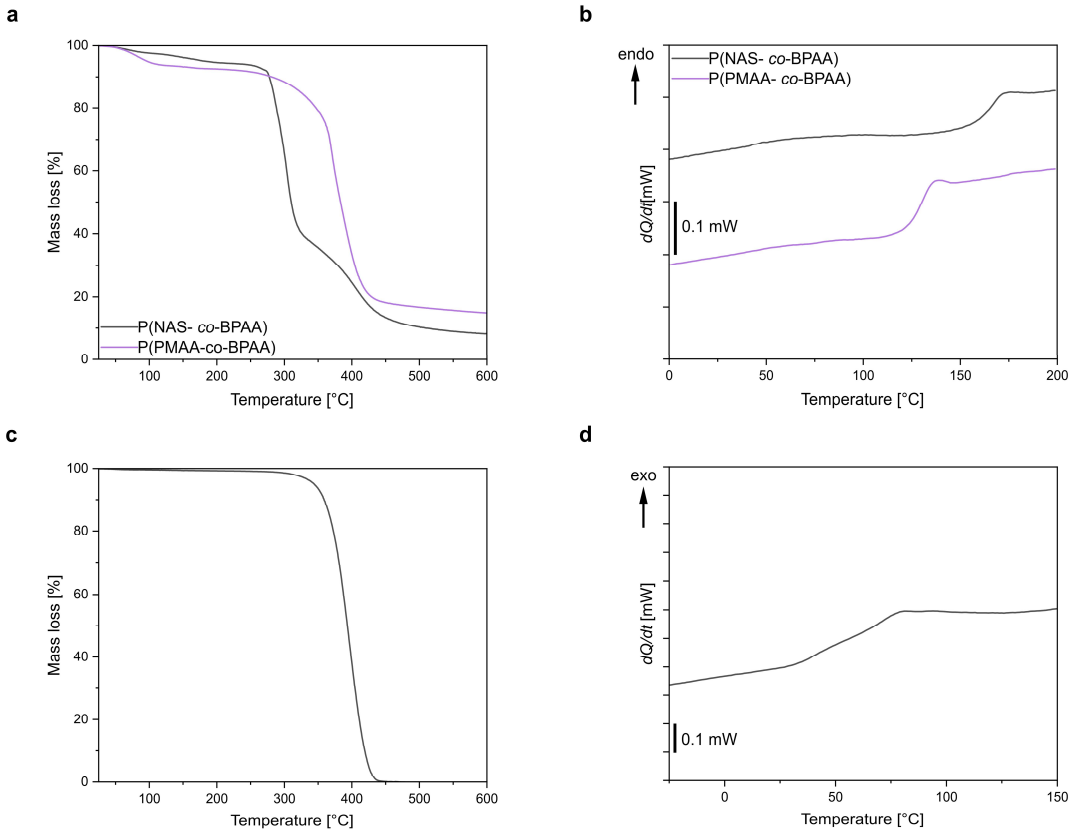

Figure 71: TGA curves of P(NAS-*co*-BPAA) and P(PMAA-*co*-BPAA) (**a**) as well as the corresponding DSC curves (T_g^{NAS}: 164 °C, T_g^{PMAA}: 128 °C) (**b**) and TGA curve of P(MA-*co*-MMA-*co*-MABP) (**c**) as well as the corresponding DSC curve (T_g: 63 °C) (**d**).

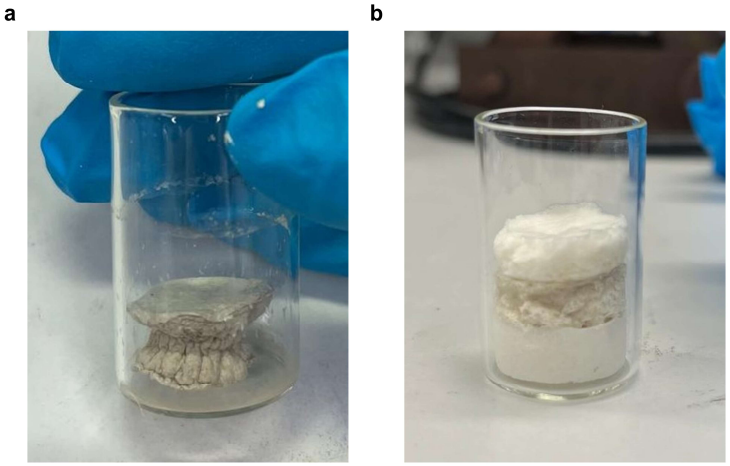

Figure 72: Optical images of a collapsed 3D BOS sponge with a short fiber concentration c_{SF} of 8.76 mg/mL and AgNW volume V_{AgNW} of 1.0 mL (**a**) as well as of a 3D BOS janus sponge of the same c_{SF} consisting of unfunctionalized bottom and top layers that enclose the AgNW functionalized layer with a V_{AgNW} of 0.2 mL (**b**).

8 Danksagung

First and foremost, I would like to express my profound gratitude to my academic guide and mentor, Prof. Dr. Andreas Greiner, whose belief in my potential gave me the opportunity to start my scientific journey. From my initial steps during the Bachelor's and Master's theses to the completion of my PhD, he provided not only personal encouragement and thematic guidance but also the necessary resources and opportunities that shaped my path. His trust allowed me to broaden my scientific horizons and to develop both professionally and personally.

I am equally indebted to dedicated members of the MC II chair, especially to my second mentor, Prof. Dr. Seema Agarwal as well as Dr. Holger Schmalz, both of whom offered invaluable thematic insights and constructive suggestions throughout my research. I also want to thank Dr. Schmalz for the RAMAN spectroscopy analysis.

A special word of thanks goes to my third mentor and collaboration partner, Prof. Dr. Markus Retsch (Physical Chemistry I), who provided a space for fruitful cooperation. I am particularly grateful to the colleagues in his laboratory, notably Ina Klein, for her close, enjoyable, and highly productive collaboration, as well as for sharing her expertise in complex thermal and electrical fiber analyses. I would also like to acknowledge Marius Schmidt from MC II, whose preparative and analytical contributions and collaboration became especially important towards the end of my PhD.

The CRC *MultiTrans* played an important role in my doctoral journey, serving as a major scientific platform. Beyond offering essential financial support for conferences and research stays, the CRC fostered interdisciplinary exchange and enriched my experience with a wide range of perspectives.

In this context, I am deeply thankful to my partners at the ICPEES in Strasbourg, particularly Prof. Guy Schlatter and Dr. Anne Hébraud, who welcomed me warmly and made my research stay unique. Special mention goes to Alessandra Pistillo, Rodolphe Migneret, Bryan Gross, and all my colleagues in Strasbourg for their support.

I also wish to acknowledge the University of Bayreuth Graduate School for broadening my knowledge beyond my core research area and facilitating valuable exchanges with fellow PhD students.

My sincere appreciation goes to all my colleagues at the MC II chair - Emilia Fulajtar, Lisa-Cathrin Leitner, Dr. Felix Bretschneider, Roman Schaller, Thomas Schmitt, Marius Schmidt, Yannick Eich, Tasmai Paul, Dr. Chengzhang Xu, Lars Schwarzer, Hendrik Volz, Dr. Chao Deng, Jinke Yang, Dan Fang, Dr. Elmar Sehl, Benedict Petran, Dr. Maximilian Rist, and all the other members from NW II and PNS - who made every day work not only easier but also more enjoyable. Their suggestions, support, and good company were indispensable.

I am grateful to Christina Lindörfer and Ramona Lechner from the secretary's office for their continuous organizational assistance, and to Annette Krökel for her vital role in laboratory management. Lothar Benker deserves special mention for his countless instances of technical support and for introducing me to both old and new processing devices. Thanks also to Simon Knorr for the efficient joint maintenance of the ICP-OES, and to Rika Schneider for conducting GPC measurements.

Beyond my immediate working environment, I would like to thank Dr. Ulrich Mansfeld and Martina Heider from the *KeyLab Electron and Optical Microscopy* for their expert guidance electron microscopy and for measuring EDX. My gratitude also extends to Alexander Berger (Physical Chemistry I) for 4PP measurements, Patrick Länger (Inorganic Chemistry III) for XRD measurements, and to Dr. Felix Bretschneider, Ina Klein, Philipp Dennstedt (Physical Chemistry II), and Alexander Kern (Macromolecular Chemistry I) for their essential contributions regarding 3D printed components.

I am especially appreciative to Dr. Felix Bretschneider, Emilia Fulajtar, Ina Klein, Marius Schmidt and Max Leinert for their help in proofreading and finalizing my thesis.

Last but by no means least, my deepest thanks go to my family and friends, who have accompanied me throughout this journey. My parents always nurtured my scientific curiosity and always believed in me. My little sister, grandparents, aunts, uncles, and further relatives provided constant support and encouragement. My friends from school and university not only motivated me through every phase but carried me forward with their support - sometimes even quite literally. Finally, I want to express my heartfelt gratitude to my partner Johannes, who has been by my side since the beginning of my time at university. Together, we have faced every challenge and enriched each other's lives with new perspectives and positivity.

This journey began with little knowledge, and although it concludes with much learned, I realize there is still so much more to discover - and I look forward to continuing that quest.

9 Eidesstattliche Erklärungen und Versicherungen

(§ 9 Satz 2 Nr. 3 PromO BayNAT)

Hiermit versichere ich eidesstattlich, dass ich die Arbeit selbstständig verfasst und keine anderen als die von mir angegebenen Quellen und Hilfsmittel benutzt habe (vgl. Art. 97 Abs. 1 Satz 8 BayHIG).

(§ 9 Satz 2 Nr. 3 PromO BayNAT)

Hiermit erkläre ich, dass ich die Dissertation nicht bereits zur Erlangung eines akademischen Grades eingereicht habe und dass ich nicht bereits diese oder eine gleichartige Doktorprüfung endgültig nicht bestanden habe.

(§ 9 Satz 2 Nr. 4 PromO BayNAT)

Hiermit erkläre ich, dass ich Hilfe von gewerblichen Promotionsberatern bzw. -vermittlern oder ähnlichen Dienstleistern weder bisher in Anspruch genommen habe noch künftig in Anspruch nehmen werde.

(§ 9 Satz 2 Nr. 7 PromO BayNAT)

Hiermit erkläre ich mein Einverständnis, dass die elektronische Fassung meiner Dissertation unter Wahrung meiner Urheberrechte und des Datenschutzes einer gesonderten Überprüfung unterzogen werden kann.

(§ 9 Satz 2 Nr. 8 PromO BayNAT)

Hiermit erkläre ich mein Einverständnis, dass bei Verdacht wissenschaftlichen Fehlverhaltens Ermittlungen durch universitätsinterne Organe der wissenschaftlichen Selbstkontrolle stattfinden können.

…….

Ort, Datum, Unterschrift